

2011-01-01

Electrochemical Behavior of Zinc

Carlos E. Castillo

University of Texas at El Paso, cecastillo2@miners.utep.edu

Follow this and additional works at: https://digitalcommons.utep.edu/open_etd



Part of the [Engineering Commons](#)

Recommended Citation

Castillo, Carlos E., "Electrochemical Behavior of Zinc" (2011). *Open Access Theses & Dissertations*. 2450.
https://digitalcommons.utep.edu/open_etd/2450

This is brought to you for free and open access by DigitalCommons@UTEP. It has been accepted for inclusion in Open Access Theses & Dissertations by an authorized administrator of DigitalCommons@UTEP. For more information, please contact lweber@utep.edu.

THE ELECTROCHEMICAL BEHAVIOR OF
ZINC

CARLOS CASTILLO

Department of Mechanical Engineering

APPROVED:

Arturo Bronson, Ph.D.

Soheil Nazarian, Ph.D.

Chintalapalle V. Ramana, Ph.D.

Patricia D. Witherspoon, Ph.D.
Dean of the Graduate School

Copyright
by
Carlos E. Castillo
2011

THE ELECTROCHEMICAL BEHAVIOR OF
ZINC

by

CARLOS E. CASTILLO

THESIS

Presented to the Faculty of the Graduate School of
The University of Texas at El Paso
in Partial Fulfillment
of the Requirements
for the Degree of

MASTER OF SCIENCE

Department of Mechanical Engineering
THE UNIVERSITY OF TEXAS AT EL PASO
May 2011

Acknowledgement

I would like to extend my deepest gratitude to Dr. Arturo Bronson for guiding me throughout my graduate career and for his advice and support. I would also like to thank Dr. Nazarian for all the advice and support that has made the completion of my degree less arduous and Dr. Ramana for his support that has made the completion of my degree possible.

Lastly, I would like to thank my friends and family for their unwavering support during my education. I would especially like to thank my fiancée Brenda Mota who supported me above anyone else during the process of finishing my degree.

Abstract

The investigation focused on the corrosion of galvanized steel exposed to soil. The primary objective of the study was to develop a technique for monitoring the corrosion behavior of samples in the field by measuring the potential and current with respect to time (or electrochemical noise). Electrochemical electrodes were designed to simulate the galvanized steel in contact with thin electrolytes which are usually generated in soils as they collect and drain rain water depending on soil porosity.

The corrosion behavior of the galvanized steel was also studied by using electrochemical impedance spectroscopy (EIS) coupled with potentiokinetic scans to predict the corrosion rate the galvanized steel immersed in solutions ranging from 0.0001 M to 0.1 NaCl. The corrosion rate for the galvanized steel reached 37.5 mils/yr (or 952.09 $\mu\text{m}/\text{year}$) at the high chloride content (i.e., 0.1 M NaCl) and 0.314 mils/year (7.97 $\mu\text{m}/\text{year}$) for the low chloride content (i.e., 0.0001 M NaCl). In comparing the corrosion rates available from field bilogarithmic trends and the acquired laboratory studies, the laboratory corrosion rates of 0.314 and 37.484 $\mu\text{m}/\text{yr}$ at 0.0001 and 0.001 M NaCl, respectively, corresponded to the field corrosion rate of 20 $\mu\text{m}/\text{yr}$ at 200 ppm Cl (approximating 0.0002 M Cl).

Table of Contents

Acknowledgement	iv
Abstract	v
List of Figures	ix
Chapter 1: Introduction	1
1.1 Overview	1
1.2 Objective	3
Chapter 2: Literature Review	4
2.1 Corrosion of Zinc and Carbon Steel.....	4
2.1.1 Corrosion of Zinc.....	4
2.1.1.1 Effect of Anions on Zn.....	8
2.1.2 Corrosion of Underlying Steel.....	11
2.1.2.1 Effect of Zinc Products on the Formation of β -FeOOH	12
2.1.2.2 Effect of anions in the formation of β -FeOOH	15
2.2 Electrochemical Methods for Studying Corrosion.....	17
2.2.1 Polarization Scans of Galvanized Steel	17
2.2.2 Electrochemical Impedance Spectroscopy	19
2.2.3 Electrochemical Noise	24
2.2.3.1 Electrochemical Noise Analysis Methods	27
2.2.3.2 PSD Acquisition Methods.....	27

2.3	Microstructure of Galvanized Steel.....	31
2.3.1	Fe-Zn Phase Diagram	31
Chapter 3: Methodology		35
3.1	Galvanized steel electrode preparation	35
3.2	Delrin coupon preparation.....	36
3.3	Electrode coupon assembly	37
3.4	Electrode positioning structure.....	38
3.5	Polarization scan experiments setup	39
3.6	Electrochemical impedance experiments setup.....	40
3.7	Electrochemical noise experiments setup	42
Chapter 4: Results and Discussion.....		45
4.1	Electrochemical Impedance Spectroscopy	45
4.2	Voltage/Current Response at Low Chloride Contents.....	53
4.3	Electrochemical Noise.....	55
4.4	Microstructure and corrosion products	63
Chapter 5: Conclusion.....		Error! Bookmark not defined.
Chapter 6: Future Work.....		73
References		74
Appendix.....		79
Polarization curves		79

Electrochemical impedance spectroscopy graphs.....	83
Electrochemical noise graphs	95
Curriculum Vitae.....	100

List of Figures

Figure 1.- Illustration of corrosion mechanism of galvanized steel (Yadav, Nishikata and Tsuru 2004).	7
Figure 2.- SEM image of Zn electrode after 5 min. immersion on 0.01 NaSO ₄ at room temperature (Aal and Wanees 2009).	10
Figure 3.- Experimental bode diagram and fit to the TML model for Type 304 stainless steels covered with a 0.1 NaCl solution layer (Nishikata, Ichihara and Tsuru 1995).	22
Figure 4.- The influence of MEM order on the characteristics of PSD. The MEM spectra are displaced upwards to allow them to be seen clearly (Cottis 2001).	29
Figure 5.- The effect of low order MEM on low frequency PSD (Cottis 2001).	30
Figure 6.- Fe-Zn equilibrium phase diagram (Kubachewski and Massalski 1986).	32
Figure 7.- Zn rich part of the Fe-Zn phase diagram (Kubachewski and Massalski 1986).	33
Figure 8.- Microstructure of Zn coating after immersion in a 450 C 0% Al bath on a ultra low carbon steel substrate. 1 gamma (Γ) phase, 2 delta (δ) phase, 3 zeta (ζ) phase (Marder 2000). ..	34
Figure 9.- Galvanized steel plate after CNC machining.	35
Figure 10.- Above, above view of a finished electrode coupon. Below, side view of a finished electrode coupon with cable holes.	37
Figure 11.- Electrode positioning structure.....	39
Figure 12.- Ideal polarization curve and tafel slopes (Jones 1992)	40
Figure 13.- Equivalent circuit	41
Figure 14.- Potentiostat and frequency response detector connection setup.	42
Figure 15.- Circuits used to acquire current and voltage electrochemical noise simultaneously.	44

Figure 16.- Bode and Nyquist plot of galvanized steel at 0.0001 M NaCl. Acquired with PowerSINE	46
Figure 17.- Solution resistance at different NaCl molarities. Acquired with PowerSINE.....	47
Figure 18.- Inverse of polarization resistance with respect to the solution molarity. Acquired with PowerSINE	47
Figure 19.- Equivalent circuit describing the one time-constant system of galvanized steel corroding in 0.0001 M NaCl solution.	48
Figure 20.- Polarization curve of galvanized steel in 0.0001 M NaCl. Acquired with PowerCV. 50	
Figure 21.- Change in current density as the NaCl molarity increases.....	51
Figure 22.-Change in MPY as the NaCl molarity increases.	52
Figure 23.- Change in $\mu\text{m}/\text{yr}$ as the NaCl molarity increases.....	52
Figure 24.- Elias' diagram showing the corrosion rates for zinc at 0.0001 and 0.001 M NaCl and 200 ppm Cl (0.0002 Cl).	53
Figure 25.- Change in potential from 0.00001 to 0.0001 M NaCl.....	54
Figure 26.- Change in current from 0.00001 to 0.0001 M NaCl	54
Figure 27.- Potential electrochemical noise data corresponding to Odessa. (1024 points sample).	56
Figure 28.- Current electrochemical noise data corresponding to Odessa. (1024 points sample).56	
Figure 29.- Potential PSD acquired from the FFT for a 1024 sample from Odessa's data. Acquired with Dadisp.	57
Figure 30.- Potential PSD acquired from MEM for a 1024 sample from Odessa's data. Acquired with Dadisp	58
Figure 31.- MEM acquired potential PSD overlapped with FFT acquired potential PSD. Acquired	

with Dadisp.	58
Figure 32.- Current PSD acquired from the FFT for a 1024 sample from Odessa's data. Acquired with Dadisp.	59
Figure 33.- Current PSD acquired from the MEM for a 1024 sample from Odessa's data. Acquired with Dadisp.	60
Figure 34.- MEM acquired current PSD overlapped with FFT acquired current PSD. Acquired with Dadisp.	60
Figure 35.- Noise impedance calculated with the PSD from the FFT of the potential and current. Acquired with Dadisp	62
Figure 36.- Noise impedance calculated with the PSD from the MEM of the potential and current. Acquired with Dadisp	62
Figure 37.- SEM image of the galvanized steel microstructure.....	64
Figure 38.- SEM image of galvanized steel electrode in 0.1 M NaCl solution.	64
Figure 39.- Line scan analysis of the microstructure of galvanized steel at the Fe-Zn interface.	65
Figure 40.- Area analysis of zinc coating. Analysis performed with EDAX.....	66
Figure 41.- Area analyzed for elements on zinc coating. (SEM image)	67
Figure 42.- Area analysis on the microstructure of a galvanized steel corroded on 0.1 M NaCl for 12 hrs. Analysis performed with EDAX.	67
Figure 43.- Area analyzed for elements on the microstructure of corroded galvanized steel on 0.1 M NaCl. (SEM image).....	68
Figure 44.- Microstructure of galvanized steel under real time corrosion for 280 days. Microstructure shows passive corrosion. (SEM image).	69
Figure 45.- Area analysis of microstructure of galvanized steel under real time corrosion for 280	

days. Acquired with EDAX.	70
Figure 46.- Chloride concentration analysis on the solution extracted from every wet cycle in the electrochemical noise experiments. Analysis performed by Dr. Borrok and Anita Thapalia.	71
Figure 47.- Polarization curve for galvanized steel in 0.0001 M NaCl solution.	79
Figure 48.- Polarization curve for galvanized in 0.001 M NaCl solution.....	80
Figure 49.- Polarization curve for galvanized in 0.01 M NaCl solution.....	81
Figure 50.- Polarization curve for galvanized in 0.1 M NaCl solution.....	82
Figure 51.- Bode and Nyquist plots for galvanized steel at 0.0001 M NaCl solution.	83
Figure 52.- Bode and Nyquist plots for galvanized steel at 0.0001 M NaCl solution.	84
Figure 53.- Bode and Nyquist plots for galvanized steel at 0.0001 M NaCl solution.	85
Figure 54.- Bode and Nyquist plots for galvanized steel at 0.001 M NaCl solution.	86
Figure 55.- Bode and Nyquist plots for galvanized steel at 0.001 M NaCl solution.	87
Figure 56.- Bode and Nyquist plots for galvanized steel at 0.001 M NaCl solution.	88
Figure 57.- Bode and Nyquist plots for galvanized steel at 0.01 M NaCl solution.	89
Figure 58.- Bode and Nyquist plots for galvanized steel at 0.01 M NaCl solution.	90
Figure 59.- Bode and Nyquist plots for galvanized steel at 0.01 M NaCl solution.	91
Figure 60.- Bode and Nyquist plots for galvanized steel at 0.1 M NaCl solution.	92
Figure 61.- Bode and Nyquist plots for galvanized steel at 0.1 M NaCl solution.	93
Figure 62.- Bode and Nyquist plots for galvanized steel at 0.1 M NaCl solution.	94
Figure 63.- Electrochemical noise potential for Odessa (sample 2). Acquired with Dadisp.	95
Figure 64.- Electrochemical noise current for Odessa (sample 2). Acquired with Dadisp.....	95
Figure 65.- Potential PSD acquired from FFT method for Odessa (sample 2). Acquired with Dadisp.	96

Figure 66.- Potential PSD acquired from MEM method for Odessa (sample 2). Acquired with Dadisp.	96
Figure 67.- Potential PSD acquired from FFT and MEM methods for Odessa (sample 2). Acquired with Dadisp.	97
Figure 68.- Current PSD acquired from FFT method for Odessa (sample 2). Acquired with Dadisp.	97
Figure 69.- Current PSD acquired from MEM method for Odessa (sample 2). Acquired with Dadisp.	98
Figure 70.- Current PSD acquired from FFT and MEM methods for Odessa (sample 2). Acquired with Dadisp.	98
Figure 71.- Noise impedance calculated with the PSD from the FFT of the potential and current. Acquired with Dadisp	99

Chapter 1: Introduction

1.1 Overview

Zinc is a common protective coating used for steels which tend to form a porous β -FeOOH layer and/or a duplex layer of Fe_3O_4 and Fe_2O_3 during aqueous corrosion. Galvanized steels in atmospheric environments are subjected to corrosion in wet and dry cycles, which differ slightly in some aspects with submerged steels in bulk solutions. For example, during the drying process of the wet/dry cycles of a thin layer of solution, the metal surface may be exposed to a more concentrated solution of chloride and/or sulfate salts developing a corrosive solution. Experiments have shown that the reactions are accelerated at first for the initial wet/dry cycles, then the corrosion rate decreases and finally becomes constant for galvanized steel (Yadav, Nishikata and Tsuru 2004).

Zinc coatings protect steel in two phases, first as a barrier separating the corrosive solution from the steel and second as a sacrificial anode. The zinc layer dissolves into the aqueous solution usually with the formation of ZnO considered the passive layer. The corrosion of the passive layer is described in the background section depending on acid/alkaline solution and chloride/sulfate anions. The anodic mode of zinc protecting the underlying layer of carbon steel depends on the coupled electrochemical reactions occurring on the Zn and Fe. Yadav, Katayama and Noda (2004) reported that the Zn sacrificial phase of the corrosion also occurs by the dissolution of the Fe-Zn intermetallic underlying the Zn coating followed by the corrosion of the steel (Yadav, et al. 2007).

Electrochemical kinetics involved in aqueous corrosion is usually investigated

within controlled potential (or potentiostatic) mode and sinusoidal potential perturbation of the anodic electrode. In both methods, after perturbing the surface with a potential signal the current developed on the electrode is measured. The continuous potential scan, usually at 0.1 mV/s, with its current response is called a potentiokinetic or polarization scan. The sinusoidal potential perturbation followed by measuring the current response of the electrode is termed an electrochemical impedance spectroscopy (EIS). Jones (1992) gives an overview of the techniques, though Kaesche (Kaesche 2003) and Fontana (Fontana 1986) give an in-depth discussion of the polarization scan. For the explanations of EIS, Macdonald acquires an impedance spectrum using Nyquist plots (e.g., Guan and Macdonald, 2009) while Mansfeld uses the Bode plot for characterizing the electrochemical kinetics (e.g., Mansfeld, 1981) (Guan and Macdonald 2009) (Mansfeld 1981).

In either technique, the interpretation of the electrochemical impedance spectroscopy (EIS) requires an understanding of the kinetics coupled with equivalent circuits to explain the corrosion behavior. The foregoing techniques perturb the electrode, but an inactive, or passive technique used more for monitoring corrosion acquires the potential and/or the current developed when the electrode is unperturbed and reacts simply to exposure to the aqueous solution. The monitoring of corrosion potential or current generated from the unperturbed electrode is termed electrochemical noise, (EN) as described by Mansfeld (Mansfeld, Sun and Hsu 2000) and Cottis (Cottis and Turgoose 1995).

In the case under study, the three techniques were used to investigate the corrosion of galvanized steel under a thin layer of electrolyte during the wet and dry

cycles. For this reason, it is difficult to apply standard electrochemical techniques. The studies made in the galvanized protection of zinc on steel under a thin layer of electrolyte are still scarce at this present day. Zhang and Valeriotte (1993) have been some of the few that have had investigated the subject; they conducted experiments measuring the potential and current on a zinc/steel couple covered with a thin layer of electrolyte (150 micrometers) using a Lugging probe (Yadav, et al. 2007) (Zhang and Valeriotte 1993).

1.2 Objective

The objective of this research is to apply passive electrochemical technique (or EN) to monitor the corrosion of galvanized steel and confirm the results with the use of electrochemical impedance spectroscopy primarily in near neutral solutions. The study is directly applicable to the corrosion of galvanized steel bars and rods used for mechanically stabilized earth (MSE) walls that have been constructed throughout the state of Texas.

Chapter 2: Literature Review

2.1 Corrosion of Zinc and Carbon Steel

2.1.1 Corrosion of Zinc

Zinc coating steels with wet/dry cycles corrode at an accelerated rate during the initial cycles, followed by a gradual decrease in the rate and finally reaching a steady state. During the first stage of exposure to the solution, the surface of galvanized steel was covered with a ZnO layer, the accelerated corrosion rate was attributed to the decomposition of ZnO in air and then dissolution of zinc as a result of chloride ions concentrated during the drying period (Yadav, Nishikata and Tsuru 2004). Furthermore, the appearance of red rust (mainly β -FeOOH), which implies the beginning of corrosion of the underlying steel layer, always appears during the stage of gradual decrease of corrosion rate (Yadav, Nishikata and Tsuru 2004). From an electrochemical impedance spectroscopy of galvanized steel, Yadav et al. (2004) showed that the exposure of the samples to larger periods of drying cycles caused a faster decrease in the inverse of the polarization resistance (R_p^{-1}), which is proportional to the corrosion rate. The appearance of red rust occurs right after R_p^{-1} showed a maximum. The time of appearance of red rust was decreased by increasing the drying period. This is an indication that with a more extended drying period, the capability of the zinc to protect through galvanic protection is reduced. The investigation revealed as well, that the thickness loss of the galvanized coating was also related to the length of the drying period. Yadav's experiments demonstrated that the samples with the shortest drying period presented the highest thickness loss of the coating, while the sample with the

longest drying period presented the least thickness loss. It is interesting to note that the sample with the shortest drying period showed the most thickness loss of coating, but it did not show red rust during the entire exposure time. In contrast, the sample with the longest drying period was the first one to show red rust to the naked eye. This indicates that the corrosion of the coating progresses uniformly throughout the first several cycles and then becomes more localized as the wet and dry cycles continues with longer drying periods. Yadav et al. (2004) reported that the extended drying periods exposed the zinc surface to more concentrated chloride solutions, thus initiating pitting corrosion that reaches the zinc/steel boundary (Yadav, Nishikata and Tsuru 2004).

Yadav et al. identified the corrosion products for zinc in wet and dry cycles in a 0.05 M NaCl solution with a layer of about 500 μm thickness. The products in order of concentration were $\text{Zn}(\text{OH})_2 < \text{ZnCl}_2 \cdot 6\text{Zn}(\text{OH})_2 < \text{ZnCl}_2 \cdot 4\text{Zn}(\text{OH})_2$ as the concentration of chloride and hydrogen ions increased. The corrosion products were formed during the drying cycle when the evaporation of the water leads to the concentration of chloride ions and reaches a solubility approximating $\approx 5 \text{ M NaCl}$. With increasing chloride ion content, thermodynamic calculations show that the most stable Zn precipitate would be $\text{ZnCl}_2 \cdot 4\text{Zn}(\text{OH})_2$. However as the corrosion proceeds, ZnO , $\text{Zn}(\text{OH})_2$ and ZnCO_3 increase faster than the rest, but in an amorphous state (Yadav, Nishikata and Tsuru 2004). This prediction would be assuming that a pH of 5.6 is maintained constant by CO_2 gas dissolution from the air in the NaCl solution (Yadav, Nishikata and Tsuru 2004). In a similar study, at 0.5 M NaCl the corrosion products were analyzed by XRD and although many peaks were obtained, only ZnO and $\text{ZnCl}_2 \cdot 4\text{Zn}(\text{OH})_2$ were the Zn compounds identified (Yadav, Nishikata and Tsuru 2004). The corrosion products on

both studies were very similar, suggesting that during the drying cycle, when the chloride ions concentrate, it leads to a similar solubility for NaCl (≈ 5 M NaCl) and therefore to a similar reaction that forms the same corrosion products for zinc on wet and dry cycles.

In the first stage of corrosion, zinc acting as a sacrificial anode dissolves into solution as Zn^{2+} . As corrosion products start to form on the surface of the zinc, Zn^{2+} diffuses through the pores of the corrosion products. The thicker layers of products (mainly $\text{ZnCl}_2 \cdot 4\text{Zn}(\text{OH})_2$) were found to develop on the zinc surface working as an anode, but the corrosion products do not impede the mass transfer of O_2 and Zn^{2+} . The reduction of oxygen occurs at the same rate throughout the whole surface, but the dissolution of zinc has a higher rate at active anodic sites than inactive sites (cathode). This difference in rates creates an increase in pH that leads to the stability of $\text{Zn}(\text{OH})_2$ and $\text{ZnCl}_2 \cdot 4\text{Zn}(\text{OH})_2$ thus increasing the difference in dissolution rates between O_2 and Zn^{2+} at cathodic and anodic sites. Once the corrosion reaches the Zn-Fe interface, the corrosion changes from anodic to cathodic and the dissolution of zinc stops due to the more positive potential of Zn-Fe interface with respect to the zinc (active sites are reduced). In the last stage, red rust was observed with the naked eye, at this stage, the zinc can still act as a sacrificial anode if it is covered with sufficient electrolyte. Figure 1 shows an illustration on the mechanics of the corrosion of galvanized steel (Yadav, Nishikata and Tsuru 2004).

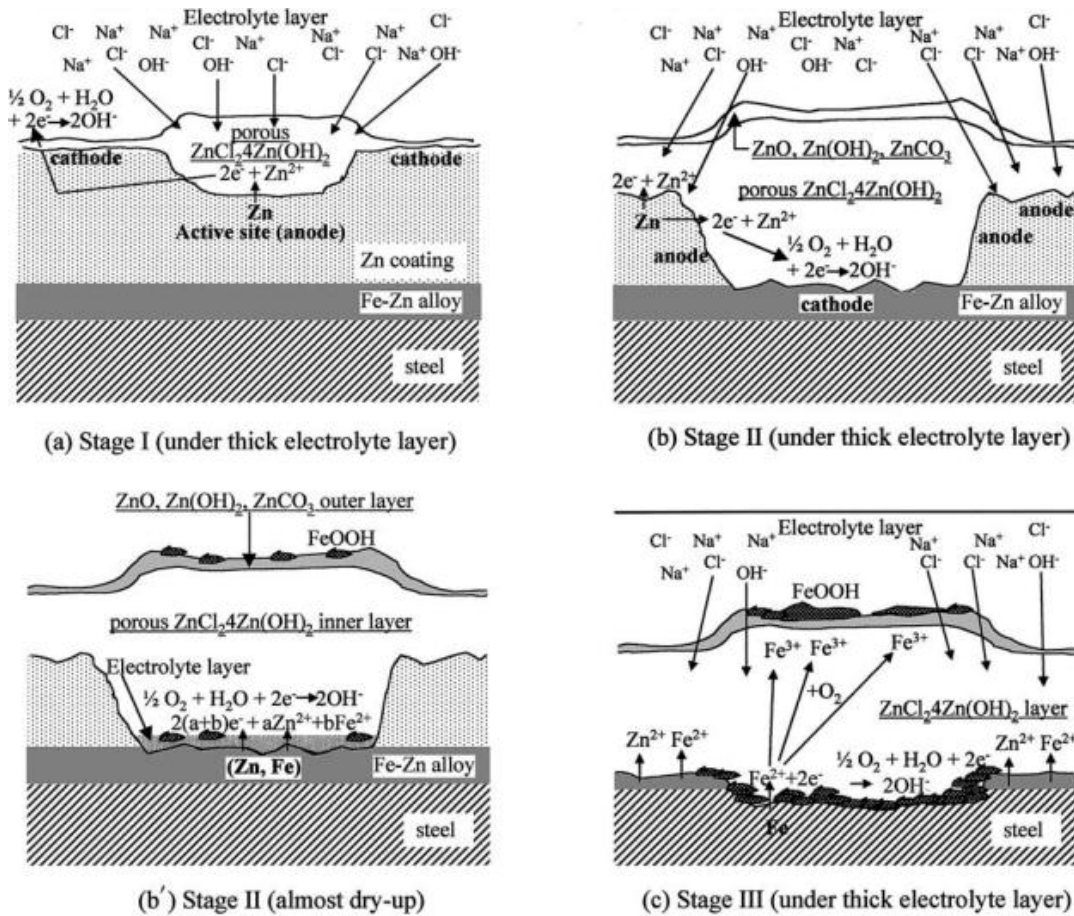
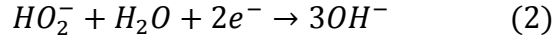
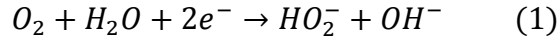


Figure 1.- Illustration of corrosion mechanism of galvanized steel (Yadav, Nishikata and Tsuru 2004).

In a different study, Yadav et al. stated that in general, the corrosion product deposition advances on the surface of the electrode, the limiting current decrease which limits the supply of O_2 to the surface of the inactive area. Nevertheless, experiments show an increase in the limiting current. This phenomenon was attributed to the change in mode of oxygen reduction due to the formation of corrosion products (e.g. oxygen may be reduced in a 2 electron transfer reaction into hydrogen peroxide or it may be reduced into hydroxide in a 4 electron transfer reaction, which indicates a fast charge transfer reaction). Equation 1 and 2 describe the reduction of oxygen into hydrogen

peroxide and hydroxide. (Yadav, Nishikata and Tsuru 2005).



2.1.1.1 Effect of Anions on Zn

El-Mahdy et al. (2000) in a study of galvanized steel conducted experiments to measure the corrosion mass loss in a solution of 0.05 M NaCl and 0.05 M Na₂SO₄ with cycles of 1 hour of immersion and 7 hours of drying for 15 cycles. The corrosion mass loss with respect to each cycle was described by equation 3.

$$\Delta M = (M_{Zn}/2F) \int_0^{t_N} i_{corr} dt \quad (3)$$

The calculations for the mass loss of zinc in 0.05 M NaCl resulted in two different regions. The first region is slightly accelerated rate of mass loss until the appearance of red rust to the naked eye, indicating the corrosion of the underlying steel. After the appearance of red rust, the mass loss rate is drastically decreased.

The results for the corrosion of Zn in 0.05 M Na₂SO₄ differ from the corrosion by a chloride solution. During the exposure to the sulfate solution, the mass loss rate remained constant throughout the whole 15 cycles. The XRD analysis of the corrosion products of the samples exposed to both solutions revealed that the corrosion products were composed of ZnO, ZnCl₂·4Zn(OH)₂, Zn₅(CO₃)₂(OH)₆, α-FeOOH, β-FeOOH and δ-FeOOH in the 0.05 M NaCl solution and only hydrated ZnSO₄ in the 0.05 M Na₂SO₄ solution. El-Mahdy et al. attributed the difference in the corrosion behavior between solutions with Cl⁻ and SO₄²⁻ anions to the difference in Zn precipitates formed on the surface (El-Mahdy, Nishikata and Tsuru 2000).

Aal and Wanees (2009) conducted experiments by galvanostatic potential techniques to generate polarization curves of Zn in near neutral solutions of Na_2SO_4 (in the range of 0.0005-0.1 M). The polarization curve defined the point in which ZnO was formed. After the formation of ZnO, the potential rose linearly until it reached a potential in which the potential moved in a negative direction, indicating the breakdown of the passive film and the initiation of pitting corrosion on the zinc surface. The authors suggested that the breakdown of the zinc passivity film can be attributed to the ability of sulfate anions to create an electrostatic field across the film electrolyte interface. When the film reaches a certain value, the adsorbed sulfate anions penetrate the zinc oxide film causing its dissolution. However, a more plausible mechanism is that SO_4^{2-} attracts H^+ ions causing an acidic solution dissolving the Zn surface. This process leads to the initiation of localized corrosion of the passive film. As shown in Figure 2, scanning electron microscope image of a polarized zinc sample of 5 minutes in 0.01 M Na_2SO_4 at 25°C and 1.8 mA/cm^2 was analyzed. This micrograph showed that in the presence of SO_4^{2-} anions, well defined pits were developed throughout the surface of the ZnO film. It was found that for the time elapsed for reaching the breakdown potential and the rate of potential increase depends directly on the sulfate anion concentration, temperature, and magnitude of the current density (Aal and Wanees 2009).

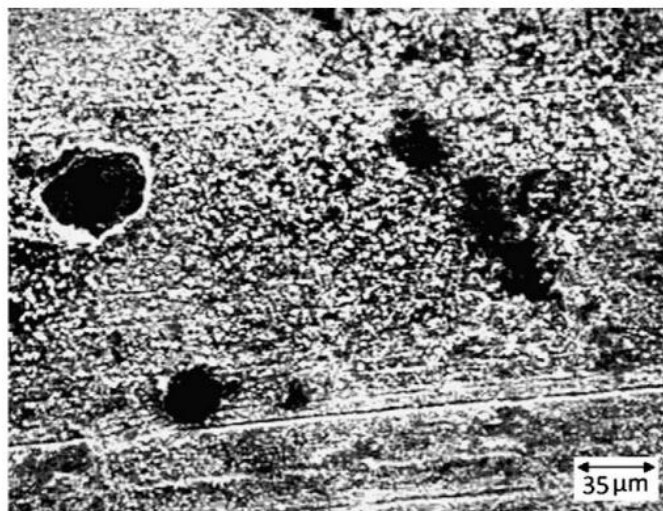


Figure 2.- SEM image of Zn electrode after 5 min. immersion on 0.01 NaSO₄ at room temperature (Aal and Wanees 2009).

Gouda et al. (1967) performed experiments by measuring the potential of pure zinc as a function of both time and anion concentration. The reason for the investigation was to categorize anions or inhibiting ions. The potential of the zinc electrode was measured at varying concentrations between 10^{-6} and 5 M. The anions were classified in two different groups depending on the variation of the steady state potentials with the concentration of the anion. The first group compiled SO_4^{2-} , Cl^- , Br^- , I^- , ClO_4^- and NO_3^- , the potential of the zinc electrode decreases with increasing concentration of these anions. The steady state potential decreased linearly and the maximum potential occurred in the beginning at the lowest concentration. This behavior denotes the destruction of the passive layer (ZnO) found on the surface of the electrode prior to the immersion in the solution. This decrease of the electrode potential with the increase of anion concentration is attributed to an unbalance between the anodic and cathodic reactions. As the anion concentration destroys the oxide film layer, the same oxide film

is being repaired by oxygen reduction. To compensate for the accelerated corrosion, the rate of oxygen reduction increases (Gouda, Khedr and Shams El Din 1967).

In the second group, CrO_4^{2-} , H_2PO_4^- , HPO_4^{2-} and NO_2^- demonstrated that at low concentrations the zinc electrode developed a potential dependent on the type of anion, but not on the concentration. As the concentration of the anions was increased, at a certain concentration (depending on the salt) the potential changes drastically towards more noble values. The switch of the potential to positive values indicates the inhibition of corrosion (Gouda, Khedr and Shams El Din 1967).

2.1.2 Corrosion of Underlying Steel

Yadav et al. (2004) reported in his investigation on the corrosion of zinc on wet/dry cycles in 0.5 M NaCl solution that red rust appears on the cycle when R_p^{-1} reaches a maximum. The calculated coating-thickness loss of 1.3 μm for a drying period of 11 hrs is significantly smaller than the initial thickness of the coating (18-20 μm). Results suggest that the corrosion of the underlying steel begins while there is still zinc present on the sample. This means that when the R_p^{-1} reaches its maximum point, steel is partially exposed to the chloride solution. As the drying periods increase, the corrosion will reach the zinc/steel boundary faster, but the thickness loss will be less than with short drying periods; a clear indication that by increasing the drying periods, it will lead to localized corrosion. However, the sample with the shortest drying period (3 h) did present a decrease in R_p^{-1} , but red rust did not appear. This means that the inhibition of zinc is necessary, but a longer drying period is needed for the corrosion of the underlying steel and the formation of red rust. This can be explained by considering the galvanic protection of the zinc. If the sample is covered with thick electrolyte solution

during the drying period, a large area around the exposed steel can work as a sacrificial anode (Yadav, Nishikata and Tsuru 2004).

Yadav (2004) also noted that red rust appeared when E_{corr} was near -0.950 V. At this potential, zinc coating serves as cathodic protection, the usual potential used for the zinc to act as a sacrificial anode for ordinary steels is ~ -0.77 V. These changes may be explained by the fact that inhibition of anodic dissolution of zinc and acceleration of the cathodic process simultaneously take place. The dual processes are attributed to the coating covered with small quantity of concentrated electrolyte imperceptible to the naked eye throughout the surface. Enough current for cathodic protection would not be supplied due to the fact that the area covered by the solution is very small. Steel starts to corrode as localized corrosion of the zinc starts to progress (Yadav, Nishikata and Tsuru 2004).

R. P. Vera Cruz et al. (1996) explained in a study of the corrosion of stainless steel on wet and dry cycles. The commencement of pitting and its growth mainly occurs just before the sample is completely dry this is when the sample is covered with a very thin layer of electrolyte. The process of repassivation takes place when the sample completely dries during the following immersion in the solution (Vera Cruz, Nishikata and Tsuru 1996).

2.1.2.1 Effect of Zinc Products on the Formation of β -FeOOH

Steel rust can be considered as the assemblage of ferric oxyhydroxides, magnetite, and amorphous ferric oxides and hydroxides. Ishikawa et al. indicates that the oxyhydroxides α -FeOOH (goethite), β -FeOOH (akaganeite) and γ -FeOOH (lepidocrocite) react with $\text{Fe}(\text{OH})_2$ to produce Fe_3O_4 (magnetite), also known as

$\text{FeO} \cdot \text{Fe}_2\text{O}_3$, which is the most common corrosion product in anaerobic conditions. The ferric oxyhydroxides will react with $\text{Fe}(\text{OH})_2$ to form eventually magnetite in the order of $\beta\text{-FeOOH} > \gamma\text{-FeOOH} \gg \alpha\text{-FeOOH}$. The crystallization and particle growth of $\alpha\text{-FeOOH}$ and $\gamma\text{-FeOOH}$ can be minimized by metal ions such as $\text{Cu}(\text{II})$, but the formation of $\beta\text{-FeOOH}$ can only be interrupted by $\text{Ti}(\text{IV})$. This indicates that akaganeite is the most stable of the ferric oxyhydroxides formed during the corrosion process (Ishikawa, Kumagai, et al. 2002).

Akaganeite ($\beta\text{-FeOOH}$) is a corrosion product often observed in steel in chloride environments. It is observed commonly in corroded archeological iron artifacts and has been known to form continuously even in the controlled atmosphere of museums. The hydroxide always contains chlorides. In a freshly prepared sample it can reach $\text{Cl}:\text{Fe}$ ratios of 1:5. It is possible to remove the chloride ions from the compound by alkaline treatment, but this results in a structural rearrangement leading to the formation of goethite ($\alpha\text{-FeOOH}$) (Refait and Genin 1997). Special interest is taken on this phase of ferric oxyhydroxide because it has been found that the corrosion of steel in chloride environments is influenced by the formation of $\beta\text{-FeOOH}$. Nakayama et al. (1998) demonstrates that the corrosion rate of weathering steels which include minor copper content can be reduced by decreasing the formation of $\beta\text{-FeOOH}$ in the surface (Ishikawa, Miyamoto, et al. 2005).

The use of galvanized coatings is not only due to the sacrificial corrosion of the zinc that protects the steel substrate. The corrosion products from the zinc also protect the underlying steel with a combination of oxides, hydroxides and basic zinc salts. These basic zinc salts provide the means for a formation of a disordered layer structure

producing adherent films to the zinc products. Metal salt films have shown to be related to the transition of pits from metastability to stability. The two regimes of pit growth found in investigation by Laycock and Newman (1997) indicate the growth of pits by mixed activation/ohmic control at lower potentials and the growth under diffusion control with a metal salt film present on the surface of the pit. The investigation predicted that the growth of pits would occur in active or salt filmed surfaces depending on the magnitude of the current density. The authors also mentioned that at low potentials, crystallographic etch pits could grow in the presence of a salt layer, given that the salt layer is thin enough. But at high potentials, hemispherical and electropolished pits would form on thicker salt filmed surfaces (Laycock and Newman 1997).

The corrosion of galvanized steel in chloride environment in an early stage leads to the formation of zinc precipitates such as ZnO and zinc hydroxychloride (ZHC) ($\text{Zn}_5(\text{OH})_8\text{Cl}_2 \cdot \text{H}_2\text{O}$), followed by the formation of $\beta\text{-FeOOH}$ which is influenced by the of Zn(II) and zinc rusts (Tanaka, et al. 2010). Tanaka et al. (2010) explains the influence of zinc corrosion products on the formation of $\beta\text{-FeOOH}$ by synthesizing particles of $\beta\text{-FeOOH}$ in the presence of ZnCl_2 , ZnO, and ZHC ($\text{Zn}_5(\text{OH})_8\text{Cl}_2 \cdot \text{H}_2\text{O}$). The XRD patterns of the synthesized products in the presence of Zn(II) do not recognize the peaks related to the existence of ZnO and ZHC ($\text{Zn}_5(\text{OH})_8\text{Cl}_2 \cdot \text{H}_2\text{O}$), suggesting that these compounds were dissolved during the formation of $\beta\text{-FeOOH}$. Also, it was confirmed that using Scherrer equation in the presence of Zn(II), the crystallite sizes of $\beta\text{-FeOOH}$ are reduced from ~60 nm to ~40 nm, and a similar tendency happens in the presence of ZnO and $\text{Zn}_5(\text{OH})_8\text{Cl}_2 \cdot \text{H}_2\text{O}$ but the reduction is more significant (from ~60 nm to ~20 nm). This phenomenon is an indication that the crystallization of $\beta\text{-FeOOH}$ can be

inhibited by the inclusion of Zn(II), ZnO and $\text{Zn}_5(\text{OH})_8\text{Cl}_2 \cdot \text{H}_2\text{O}$, with an inhibition order of $\text{ZHC} \approx \text{ZnO} > \text{Zn(II)}$ (Tanaka, et al. 2010).

Previous investigations have reported that Fe(III) is hydrolyzed at $\text{pH} \geq 2$ to form iron hydroxides of the form $\text{Fe}(\text{OH})_x^{(3-x)}$. The pH of the chloride solution with Zn(II) decreases gradually as the solution ages but when ZnO and $\text{Zn}_5(\text{OH})_8\text{Cl}_2 \cdot \text{H}_2\text{O}$ are added to the solution it has a sudden increase to a pH of 2.3 in about 15 minutes of aging and then it decreases rapidly for an hour. The sudden increase in the pH is attributed to the dissolution of the ZnO and $\text{Zn}_5(\text{OH})_8\text{Cl}_2 \cdot \text{H}_2\text{O}$ compounds, which then causes an acceleration in the formation of $\text{Fe}(\text{OH})_x^{(3-x)}$ resulting in the rapid reduction of the pH for an hour. The $\text{Fe}(\text{OH})_x^{(3-x)}$ hydroxides are condensed to form amorphous iron oxides and hydroxides that originate the formation of $\beta\text{-FeOOH}$ particle. After the decrease in pH, the hydrolysis of Fe(III) is inhibited and the crystallization and particle growth of $\beta\text{-FeOOH}$ is suppressed. Also, the ZnO and ZHC in the solution interfere in the crystallization and particle growth of $\beta\text{-FeOOH}$ as it was mentioned above (Tanaka, et al. 2010).

2.1.2.2 Effect of anions in the formation of $\beta\text{-FeOOH}$

It is well known that the phase and crystallization of the various iron oxides formed in corroding solutions depend on the conditions of the electrolyte, such as anions coexisting, concentrations, pH and temperature. The formation of akaganeite requires the presence of halide ions like Cl^- , but the formation of its structure can be influenced by the existence of different anions such as SO_4^{2-} , NO_3^- , HPO_4^{2-} , and SiO_3^{2-} . The latter two are supposed to be present in soils and treating agents of steels (Ishikawa, Miyamoto, et al. 2005).

It has been reported that β -FeOOH was found mainly in areas of thick corrosion layers, and scarcely in areas where the corrosion layers are thin. Asami et al. (2003) mentioned that in these areas where the corrosion layer is thin, β -FeOOH may be working as a reservoir of chloride ions (Asami and Kikuchi 2003). In the presence of sulfate anions, α -FeOOH is the most stable phase of ferric oxyhydroxide. According to Yamashita et al. (2005), the formation of β -FeOOH occurs in the presence of concentrated chloride ions in thin electrolyte films created during the drying of the solution on the surface of the steel. This phenomenon is also encountered during the drying process of the wet-dry cycle experiments (Yamashita, et al. 2005).

Ishikawa et al. (2005) performed XRD analysis of a sample of β -FeOOH obtained through the oxidation of Fe(II). The peaks only indicated the formation of β -FeOOH in the sample. The analysis indicated that the addition of SO_4^{2-} lowers the intensity of the peaks and reduce the crystallinity of the particles. The addition of HPO_4^{2-} also reduces the crystallinity of the particles, on the contrary to the presence of NO_3^- and SO_4^{2-} which showed no influence on the crystallinity. The XRD results of a similar β -FeOOH sample obtained through the hydrolysis of Fe(III) demonstrated similar results to the Fe(II)-oxidation, except for the products in the presence of SO_4^{2-} , which showed an improved crystallinity at low $\text{SO}_4^{2-}/\text{Fe(III)}$ ratios (Ishikawa, Miyamoto, et al. 2005).

The structure of β -FeOOH rust formed by Fe(II)-oxidation and Fe(III)-hydrolysis is affected by the presence of different anions. To confirm these results, Ishikawa et al. (2005) performed an Infrared spectroscopy to corroborate the inclusion of the anions to the particle structure of β -FeOOH. The results indicated that SO_4^{2-} and HPO_4^{2-} are incorporated in the structure of the particle and causes the particle to grow and

improves the crystallization. Also, the NO_3^- ions barely affect the formation of $\beta\text{-FeOOH}$ due to the low Fe(III)-complex logarithmic stability constant of 1.0 at 25°C , in contrast to the magnitudes of 9.1 and 4.0 of HPO_4^{2-} and SO_4^{2-} respectively (Ishikawa, Miyamoto, et al. 2005). In a similar study, Kamimura et al. (2005), described from an XRD spectrum that when cations are added as nitrates, there is no significant change in XRD peaks and are not incorporated to the structure of $\beta\text{-FeOOH}$. It is mentioned that the incorporation of such cations is dependent on the coexistence of anions (Kamimura, et al. 2005).

2.2 Electrochemical Methods for Studying Corrosion

The evolution of the use of electrochemical impedance spectroscopy (EIS) as a tool for studying the corrosion has been reviewed by Epelboin et al. (1970). The use of EIS techniques has proven to be very useful to obtain data that could not be obtained through traditional DC techniques, for example, the measurement of corrosion rates in a low conductivity solution (F. Mansfeld 1990). However, some electrochemical techniques were not suited for the present study due to the nature of the present experiments, such as the corrosion monitoring under a thin layer of electrolyte solution or the study of polarization curves in near neutral solutions.

2.2.1 Polarization Scans of Galvanized Steel

The corrosion rate, i_k , can be calculated through back extrapolation of the linear section of the anodic and cathodic region (Tafel slopes) to the corrosion potential E_k from polarization curves. Though, this technique cannot be carelessly used with non-stirred near neutral solutions, the reason for this is that the mass transport of reactants (H^+ or O_2), or products (M^+) towards and away from the surface of the metal surface

progresses in a very slow manner. The slow mass transfer of reactants and products affects the charge-transfer reaction, by causing a shift in the Tafel slopes due to an alteration in the measurement of the corrosion potential (E_k) and current density (i_k). The partial cathodic reaction (hydrogen evolution) would be altered by the slow diffusion of hydrogen ions toward the surface of the electrode, and then causes a decrease in the corrosion potential and the current density. The partial anodic reaction (metal dissolution) would be affected by the concentration of metal ions in the vicinity of the electrode surface, which causes an increase in the corrosion potential and a decrease in the current density. Due to the previously stated reasons, back extrapolation can lead to erroneous results (Walter 1975). A more appropriate procedure would be the measurement of the polarization resistance, R_p , (which is directly related to the corrosion rate), by small polarizations that allows to proceed to the steady state situation. The main disadvantage of this method is that the experiments may take a significant amount of time (~1 hour) if the measurements of polarization resistance are to be accurate (Walter 1975).

Walter (1976) identifies several possible sources of error in calculating corrosion rates from data acquired in low polarization data experiments. These errors are: the incorrect inclusion of the diffusion portion of the potential response, the neglect of the curvature in the polarization curve in the vicinity of the corrosion potential, the neglect of the metal ion deposition when the corrosion potential nears the equilibrium potential, and the values for the anodic Tafel slope for a zinc coating containing impurities may vary during the experiment and may also differ from the literature values of pure zinc. The shape of the potential response curve to a current step changes over the time of

immersion of the sample in the solution. At low immersion times, the diffusion portion of the potential is not observed and it is negligible, as the immersion time increases the potential response obtained contains a small portion of the diffusion polarization, which inevitably results in corrosion rates smaller than they should be. The polarization curves for zinc and zinc coatings show a curvature in polarization curves near the corrosion potential. The slope at the corrosion potential is acquired in order to build the polarization resistance curve. The range of the linearity, based on a 5% deviation of the polarization curve from linear behavior at the corrosion potential is of about 1.5 mV for zinc and zinc coatings. In the case of such a small linear range, results obtained outside of this range may result in inaccurate corrosion rates. The increase of metal ions in the solution may increase the metal equilibrium potential, defined as the difference between the corrosion and equilibrium potentials; this is important especially at long immersion times due to the accumulation of metal ions in the solution resultant from soluble corrosion products. The consideration of the accumulation of metal ions in the calculation of the mass loss results in more accurate results. The values of anodic Tafel slopes for zinc have been shown to change over the period of sample immersion, because of the direct relationship between the anodic Tafel slope and the calculation of the corrosion rate. Such changes may result in considerable errors in calculating corrosion rates if ignored (Walter 1976).

2.2.2 Electrochemical Impedance Spectroscopy

Atmospheric corrosion occurs due to the presence of dissolved salts and gases in thin electrolyte solutions deposited on the metal surface. The thickness of this thin electrolyte layer has an influence on the atmospheric corrosion rate of the metal. The

thickness of the solution affects the oxygen diffusion through the electrolyte controlling the rate of the cathodic reaction of the metal corrosion and the solubility of the corrosion products, which controls the concentration of anions. Also, during the drying period of the thin electrolyte layer, an increase in concentration of the anions occurs and often a change in the solution pH. Therefore, the corrosion mechanism of metals under a thin electrolyte solution is more complicated than in bulk solutions. Nishikata et al. (1995) mention that the largest problem on applying electrochemical impedance spectroscopy (EIS) methods in corrosion of thin electrolyte layers is that the solution resistance is extremely high as the thickness of the electrolyte becomes very thin. When this occurs, the high resistance and the non-uniform current density lead to serious inaccurate electrochemical data measurements causing erroneous results in the calculation of atmospheric corrosion rates (Nishikata, Ichihara and Tsuru 1995). For the impedance from sinusoidal potential perturbation, at high frequencies the solution resistance is measured; at low frequencies the impedance represents the sum of the polarization and the solution resistance. The polarization resistance is inversely proportional to the corrosion rate in aqueous solutions. Also, since the solution resistance is comparatively large in atmospheric corrosion systems, the current distribution over the working electrode can be monitored by monitoring the frequency response of the electrode. As a result, the EIS technique is very useful to monitor the atmospheric corrosion rates after determining furthermore equivalent circuits to simulate the dissolution at the metal-thin electrolyte layer interface (Nishikata, Ichihara and Tsuru 1995).

Nishikata et al. also reported that some previous investigations using polarization curves and impedances of metals in thin electrolyte layer have neglected the

contribution of the current distribution over the surface of the working electrode. To take into account for the current distribution, Nishikata et al. (1995) used a transmission line model (TLM), in which the current distribution over the working electrode is considered. With a transmission line, the EIS analysis model provides the effects of current distribution over the surface of the electrode can be established. On a plot of the phase shift angle (θ), the phase angle must pass further than -45° so the current distribution becomes uniform especially at low frequencies, as shown in Figure 3. Accordingly, the polarization resistance obtained can be used to acquire an accurate corrosion rate (Nishikata, Ichihara and Tsuru 1995), as exemplified in the EIS data obtained for stainless steel with two different electrolyte thicknesses (10 and 1100 μm) of 0.1 M NaCl. The impedance for 0.1 M NaCl with a thickness of 10 μm shows the effect TLM type frequency dependency in the frequency range of 1Hz-10kHz. Corresponding to the region used to acquire the solution resistance.

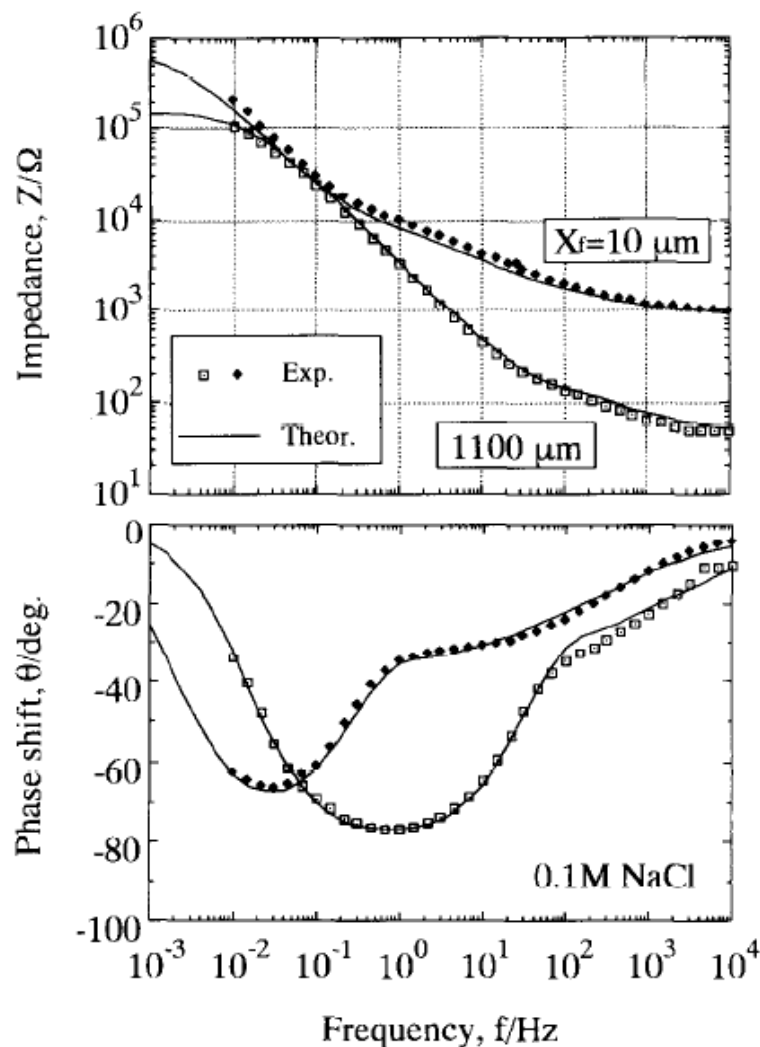


Figure 3.- Experimental bode diagram and fit to the TML model for Type 304 stainless steels covered with a 0.1 NaCl solution layer (Nishikata, Ichihara and Tsuru 1995).

Yadav et al. (2004) performed studies on the atmospheric corrosion of galvanized steel in cycles of wet and dry in a solution of 0.5 NaCl with electrochemical impedance spectroscopy. The experiments were conducted for a period of 336 h by exposure of alternate conditions of 1 h immersed in the solution and drying periods (11, 7 and 3 h). For the analyses of the data, the inverse of the polarization resistance (R_p^{-1}) was directly related to the corrosion behavior of the zinc coating. In contrast to previous studied

where the corrosion rate was calculated over the whole exposure time, Yadav et al. (2004) performed the corrosion rate calculations over the time when the electrode is still wet, at least with a thin layer of electrolyte. This gives a better understanding of the corrosion behavior under wet-dry cycles because the corrosion rate becomes negligible when the electrode is completely dry. The time of wetness of the sample was acquired from the impedance at the high frequency, which determines the solution resistance, R_s . The solution conductance, R_s^{-1} , was monitored throughout the experiment and it was determined that the sample would be considered to be wet when the solution conductance was greater than $1 \times 10^{-3} \Omega^{-1}$ (Yadav, Nishikata and Tsuru 2004).

For localized corrosion, Annergren et al. (1998) approached the investigation on the growth of pits by electrochemical impedance spectroscopy. Annergren et al. (1998) found that during the pit growth, the electrochemical impedance consists of the active pit and the passive area surrounding the pit. Therefore, localized electrochemical impedance spectroscopy (LEIS) can provide information on the impedance changes occurring on a small area, which helps obtain information on the impedance behavior that only originates from the pit. The study of pit growth through (LIES) provides similar results as the investigations through artificial pit techniques; the advantage of LIES is that the measurements are acquired from microscopic pits surrounded by passive area while the artificial pit techniques are done through macroscopic pits. Also, it was determined that with LEIS technique, the presence of salt films could be detected during pit growth (Annergren, Zou and Thierry 1999).

In summary, EIS has matured as a technique to measure uniform corrosion and pitting with the ability to consider the effects of transmission line on the metal surface,

capacitance within the passive film and solution, and salt films.

2.2.3 Electrochemical Noise

The noise resistance (R_n) acquired from the experimental potential and current noise data has attracted the attention of many corrosion scientists and engineers since it was suggested that R_n was related to the polarization resistance R_p . Electrochemical noise (EN) techniques have become an attractive alternative to electrochemical impedance spectroscopy, the relative ease of the data acquisition (Mansfeld and Lee 1997), and because of the low cost of electrochemical noise analysis.

Gabrielli et al. (1990) described electrochemical noise as the fluctuations of free potential or the fluctuations of current when a constant potential is applied. He also describes that the noise can be analyzed in the time domain by counting the events or in the frequency domain by acquiring its power spectral density (PSD), which estimates the power of the signal. The most common approach to build a power spectrum density is to calculate it through a fast Fourier transform (FFT) algorithm (Gabrielli, Huet and Oltra 1990).

Macdonald et al. (1996) mentioned that all localized and general corrosion processes, such as general corrosion, pitting attack, stress corrosion cracking and crevice corrosion, result in fluctuations of the cathodic and anodic partial currents as well as in the free corrosion potential. Macdonald also commented that electrochemical noise measurement has been used for monitoring corrosion activity in different investigations, even though the sources of electrochemical noise are still unclear. Some authors believe that it is due to the formation of hydrogen bubbles or the absorption of hydrogen by the first layers of metal after the dissolution of the passive film, at least in

the case of general corrosion. In the case of localized corrosion such as crevice corrosion, pitting attack or stress corrosion cracking, the electrochemical noise is more associated to the development of damage of the passive film (Macdonald, Liu and Manahan 1996).

Mansfeld and Xiao (1994) mentioned that previous studies were performed with only the use of electrochemical potential to analyze localized corrosion. Later it was recognized that simultaneous monitoring of both potential and current noise would provide information on more conventional electrochemical processes for systems undergoing uniform corrosion such as linear polarization resistance and electrochemical impedance. This observation was demonstrated by calculating the transfer function (R_n) between the current and potential noise signals. R_n corresponds to the coating resistance for coating undergoing general corrosion at rates greater than 0.1 mpy. For systems undergoing a slower rate of corrosion (passive materials), it is ideally better to replace R_n with a complex impedance Z_n . In the general case for the study of potential and current noise signals, $R_{ct} = R_n = R_p$, where R_{ct} is the charge transfer resistance, and R_p is the polarization resistance and assuming solution resistance is negligible (Mansfeld and Xiao 1994).

Mansfeld and Lee (1997) mention that the determination of spectral noise plots in which $\log R_{sn}$ (spectral noise resistance) is plotted vs. $\log f$ similar to bode plots, can only be done if the potential and current noise data are obtained simultaneously. The spectral noise resistance is defined as the dc-limit of the spectral noise plot. The authors also mention that the main problem in the analysis of electrochemical noise data is the frequency dependence of R_n . In order for R_n to be equal to R_p as it was

assumed by Skerry et al. (1991), R_n cannot depend on the frequency, since R_p is defined as

$$R_p = \lim_{f \rightarrow 0} (|Z(f)|) - R_s$$

For R_n and R_p to be equal, the potential and current PSD plots must have equal slopes. If the slopes are different, R_n can provide information on the degradation of the coating, but cannot be related as a specific coating property (Mansfeld and Lee 1997).

Cottis (2001) indicated that the standard method used for measuring electrochemical noise consists of monitoring the current noise between two nominally identical working electrodes. Then the potential noise of the two working electrodes can be measured with respect to a reference electrode or a third working electrode. This method has the advantage of measuring both the potential and current noise simultaneously and also both measurements are related to the same working electrodes. The area of the working electrodes plays an important role in the monitoring of the potential noise since the potential noise of the third working electrode may be larger if it is used as a reference electrode (Cottis 2001).

The effect of the electrode area on electrochemical noise measurements is yet to be fully established; however it is considered that the current noise amplitude is proportional to the electrode's surface area, and assuming that the potential noise is produced by the effect of current noise on R_p , therefore the potential noise also has a dependence on the area of the electrode. This theory is based on the assumption that the current noise is caused by a large number of uncorrelated sources. Therefore, the most common approach to report the electrochemical noise measurements is by

specifying the area of the electrode used for the measurements (Cottis 2001).

2.2.3.1 Electrochemical Noise Analysis Methods

The analysis methods of electrochemical noise can be divided into two groups. One group treats the collection of current and potential noise independent of the order in which they were recorded, these sequence-independent methods are called statistical and consist of the mean, root mean square, variance, standard deviation, moments, skew, kurtosis, and other higher order statistics (Cottis 2001). The second group takes into account the sequence within time in which the measurements were recorded. These methods include the autocorrelation function (ACF), which is defined as the expected value of the product of the time series at one time and at certain later times. This method is the simplest among the sequence-dependent analysis methods although it has generally been superseded by power spectra. The power spectra method estimates the power present at various frequencies including the signal; the power spectrum plots the power per unit of frequency, as a function of frequency (PSD). There is no correct way to estimate a power spectrum, but two methods are commonly used to obtain the PSD, the fast Fourier transform method (FFT) and the maximum entropy method (MEM).

2.2.3.2 PSD Acquisition Methods

The most direct method for the estimation of power spectrum is the fast Fourier transform, the method consists of computing a set of sine waves that combined can obtain the measured signal. Due to the obvious relationship between the measured signal and the obtained power spectrum, the FFT is believed to have a fundamental connectivity to the transient or steady-state signal. However, by sampling at a different

time, the values would change and the resulting PSD would also be different. In any case the acquired power spectrum density is valid and neither of the approaches is more correct than the other when describing the behavior of a single spectrum. This was proven by the usual averaging of multiple spectra to reduce the scattering.

An alternative to the averaging of spectra in the PSD, the spectrum can be smoothed by fitting functions to the power spectrum. This method is the maximum entropy method; this approach has been little used and needs further investigation. The MEM is a method that is still broadly misunderstood in the corrosion literature; some authors have even considered the MEM as a method unsuited to calculate power spectra. However this is based on the comparison of the scattered FFT and the MEM with a relatively low order. If the FFT is smoothed through averaging or the order of the MEM is increased, the resulting PSD is rather similar. Figure 4 demonstrates the similarity between the PSD obtained at high order of MEM and the FFT. In past studies, the FFT has been used to validate the results acquired by the MEM method, because the FFT is not prone to misleading results and is better understood.

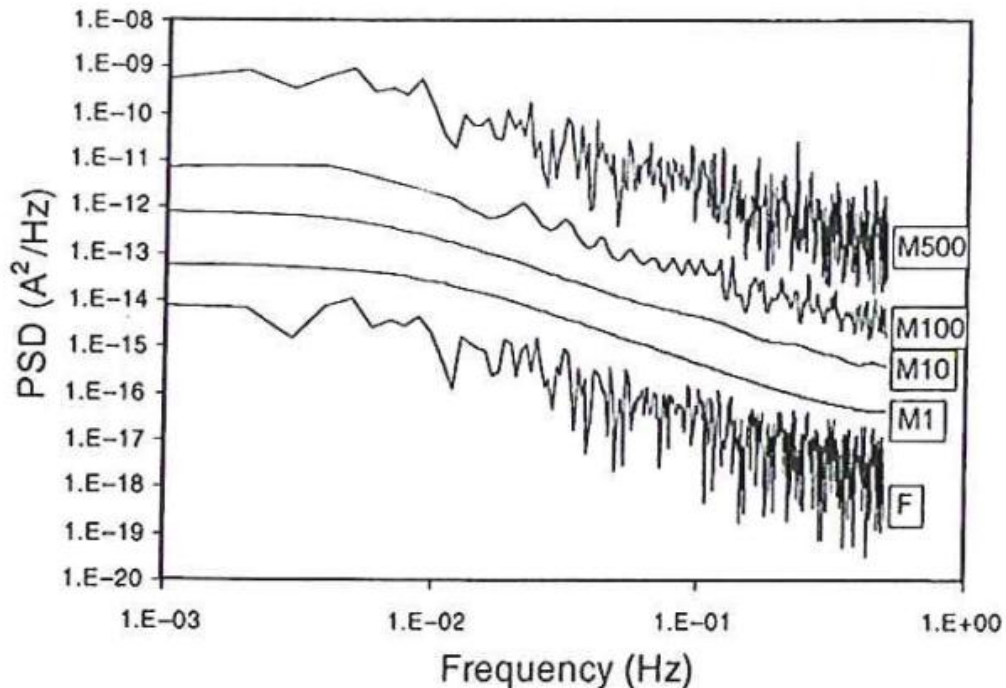


Figure 4.- The influence of MEM order on the characteristics of PSD. The MEM spectra are displaced upwards to allow them to be seen clearly (Cottis 2001).

The MEM method claims an advantage over the FFT method that indicates the ability to extrapolate to lower frequencies than the minimum frequency, but this is recognized by Cottis (2001) as a misunderstanding of the MEM features. The MEM method makes the minimum possible assumptions about the values of the PSD at frequencies outside the range that can possibly be analyzed, but this is hardly a valid extrapolation (Cottis 2001). According to Bertocci et al. (1998), the values estimated by the MEM method outside the frequency range generate a low frequency plateau whether it exists or not (Bertocci, et al. 1998). Cottis (2001) mentions as well that a low order of the MEM method can give false indication of a plateau at low frequencies. Cottis also mentions that the FFT is often used as a guide for the optimization of the high order MEM. Figure 5 demonstrates the low frequency plateau phenomenon

acquired by MEM.

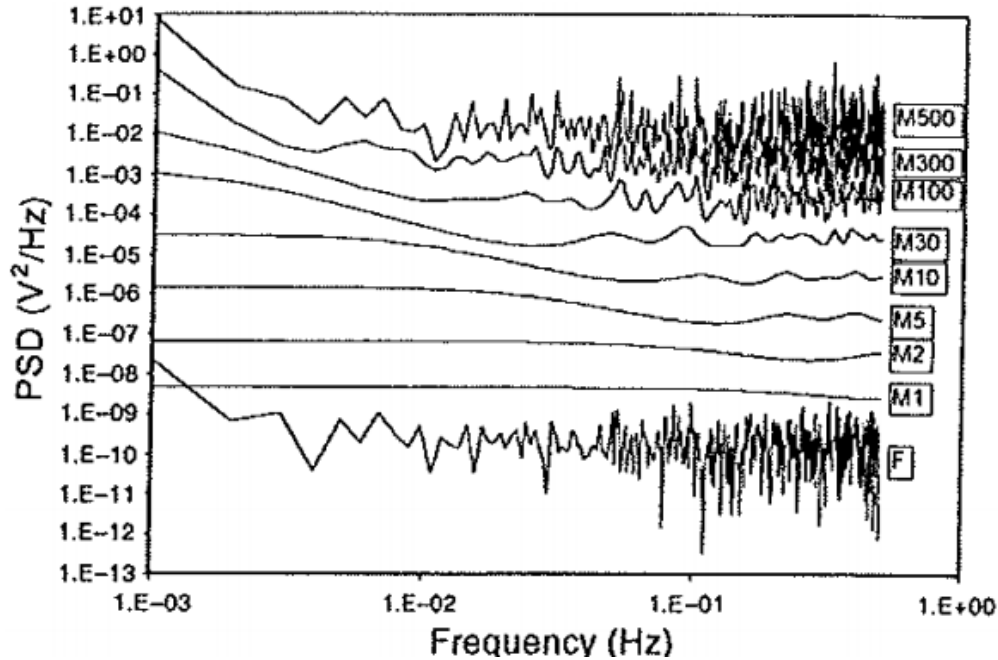


Figure 5.- The effect of low order MEM on low frequency PSD (Cottis 2001).

For the PSD to be defined the stochastic signal must be stationary and have a constant time average, which would result in a PSD with a constant time average and no drifts. Bertocchi et al. (1998) mentioned that both the FFT and MEM methods are inaccurate in calculating the PSD for non-stationary systems. Analyses of the electrochemical noise data of these systems, show that the erroneous spectra can be identified easier in the FFT than with the MEM method. During analyses of non-stationary systems, windowing becomes very necessary since other methods such as moving average, polynomial fitting and linear regression cancel part of the fluctuations and therefore alter the PSD. Windowing implies the multiplication of the time record by a function that shrinks to zero at the beginning and end of the time window and is equal to one in the middle. This reduces the confusion of low frequencies as high frequencies

and eliminates the drifting without the altering the PSD (Bertocci, et al. 1998).

2.3 Microstructure of Galvanized Steel

The typical processes for the production of galvanized steel include hot-dipping galvanizing, electrodeposition and thermal spraying. One of the preferred methods on industry and the one under study in the present investigation is the hot-dipping galvanizing method. Galvanization by hot-dipping method consists of dipping the steel article on a bath of liquid zinc or zinc alloy. The bath temperature depends upon the composition of the coating alloy, the melting point of the alloy and the temperature of the steel article prior to the dipping. A galvanized Zn (<.3% Al) bath is maintained between 445 and 450°C and the immersion time is from 3 to 6 minutes depending on the thickness of the steel article. For a Zn-5%Al since it is an eutectic, a lower temperature of 425°C is used and for a Zn-55%Al the temperature of the bath is kept at 600°C (Marder 2000).

2.3.1 Fe-Zn Phase Diagram

The structure of the zinc coated steel consists of the coating alloy, the interfacial reactions between the overlay and the substrate steel to produce inter-metallic compounds and finally the substrate steel. The possible reactions that occur between iron and zinc are explained by the phase diagram. The Fe-Zn system has been modified several times since it was first presented in 1938, especially the zinc rich part. The most widely accepted Fe-Zn system equilibrium phase diagram is that of Kubachewski (1986) presented in Figure 6.

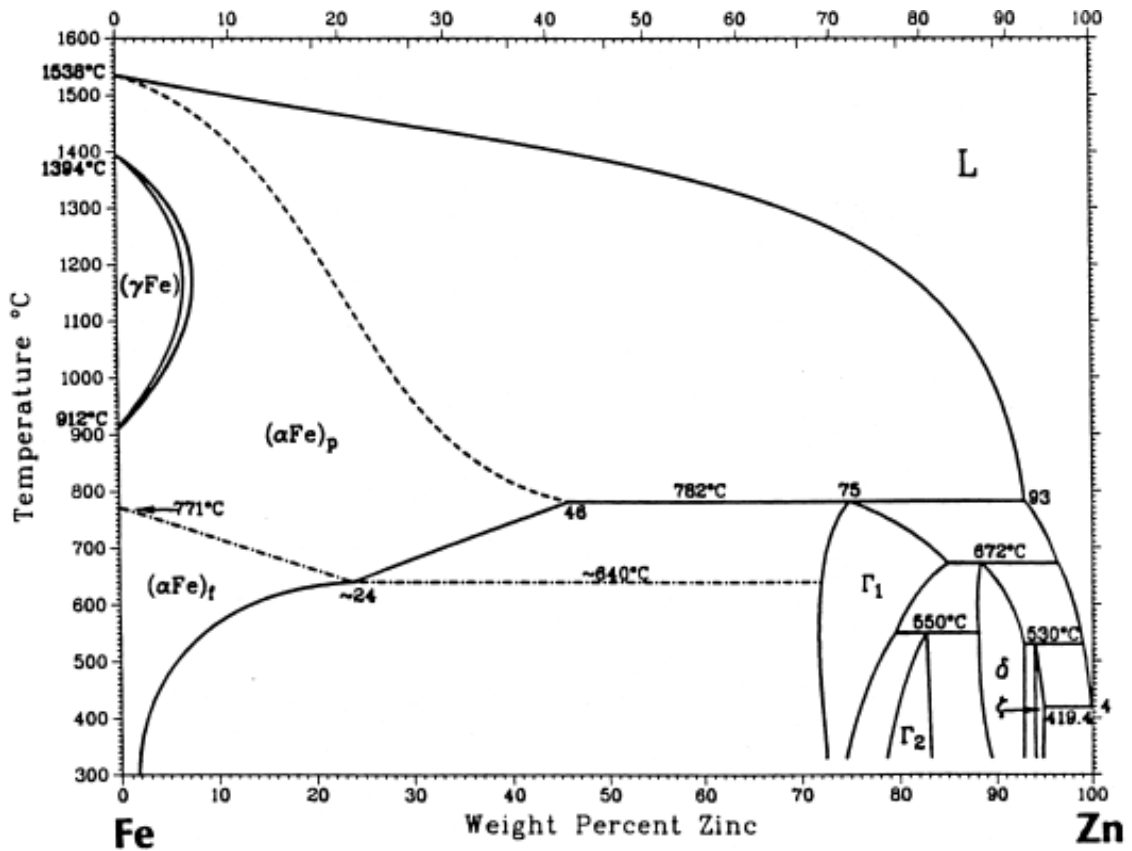


Figure 6.- Fe-Zn equilibrium phase diagram (Kubachewski and Massalski 1986).

When iron is immersed in molten zinc at the typical galvanizing temperatures (450-490°C), according to the phase diagram, Horstmann (1978) proposed that the following phases should be formed, zinc saturated α -iron, gamma (Γ) phase layer, gamma₁ (Γ_1) phase layer, delta (δ) phase layer and an eta (η) phase layer (Horstmann 1978). Figure 7 shows the Zinc rich part of the Fe-Zn equilibrium phase diagram by Kubachewski.

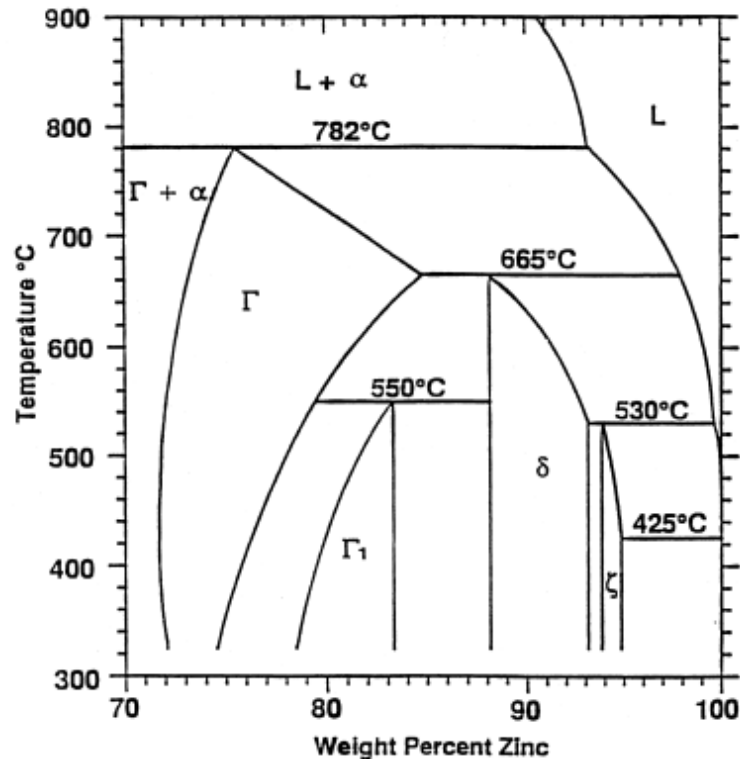


Figure 7.- Zn rich part of the Fe-Zn phase diagram (Kubachewski and Massalski 1986).

The sequential formation of the Fe-Zn phases originate at the zinc-steel interface beginning with the zeta (ζ) phase layer, followed by the delta (δ) phase layer and after some incubation the formation of the gamma (Γ) phase layer. Figure 8 shows in an optical micrograph how the gamma layer is so small that the layer is assumed to contain both Γ and Γ_1 phase layers. The phase layer development of the Fe-Zn system starts with the zeta (ζ) phase formation, immediately followed by the formation of the delta (δ) phase at the α -iron/ zeta (ζ) phase interface. The zeta (ζ) and delta (δ) phases form a continuous layer after a 5 seconds immersion, however the gamma (Γ) phase was found to form after 30 seconds incubation. The zeta (ζ) phase layer has two layers (ζ_1 and ζ_2) depending on the saturation of Fe in the alloy melt. The zeta phase grows in a columnar morphology that is saturated with Fe, the continued growth of these crystal

form a new kind of zeta phase (ζ_2). If the zinc melt is supersaturated with iron, the sufficient formation of these zeta phase crystals saturated with iron can lead to the formation of these crystals in the melt, the ζ_2 will be separated by the solid zinc η phase, as it can be seen in Figure 8 (Marder 2000).

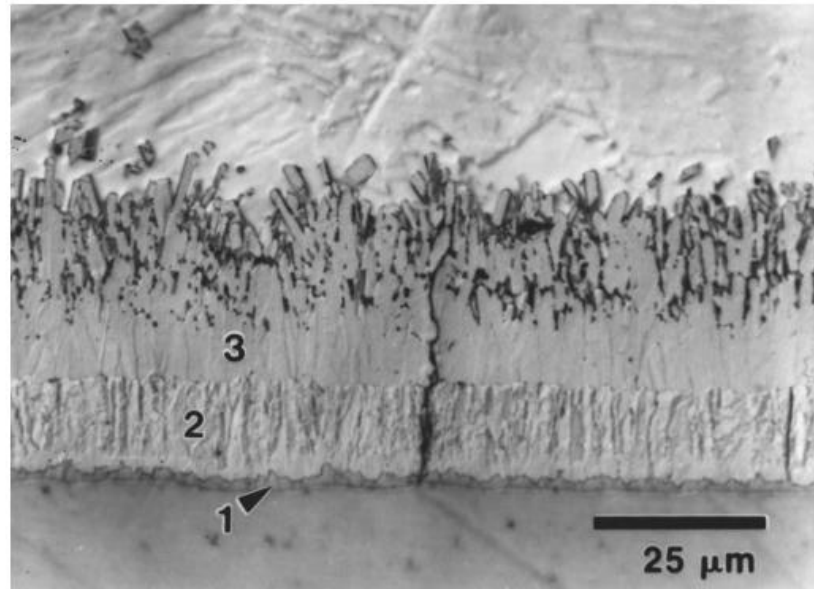


Figure 8.- Microstructure of Zn coating after immersion in a 450 C 0% Al bath on a ultra low carbon steel substrate. 1 gamma (Γ) phase, 2 delta (δ) phase, 3 zeta (ζ) phase (Marder 2000).

Chapter 3: Methodology

3.1 Galvanized steel electrode preparation

The galvanized steel strands were cut in sections avoiding ribs or scratches and sections that are straight enough to machine into electrodes. The sides of the section of galvanized steel segments were chosen, and then the sections were machined in a Hass super mini-mill CNC. The CNC was programmed to create an area of $1 \times \frac{1}{2}$ cm. The CNC used a $\frac{1}{4}$ in. four flute end-mill made of tungsten carbide in a cobalt matrix. Coolant was used during the whole machining process with the CNC to avoid the heating of the material, which would change the microstructure of the metal such as grain size and consequently the corrosion characteristics. The spin and feed rates of the CNC were also fixed to ensure the zinc coating does not suffer damage during the machining process. Figure 9 shows how the plate looked after the CNC process was completed.

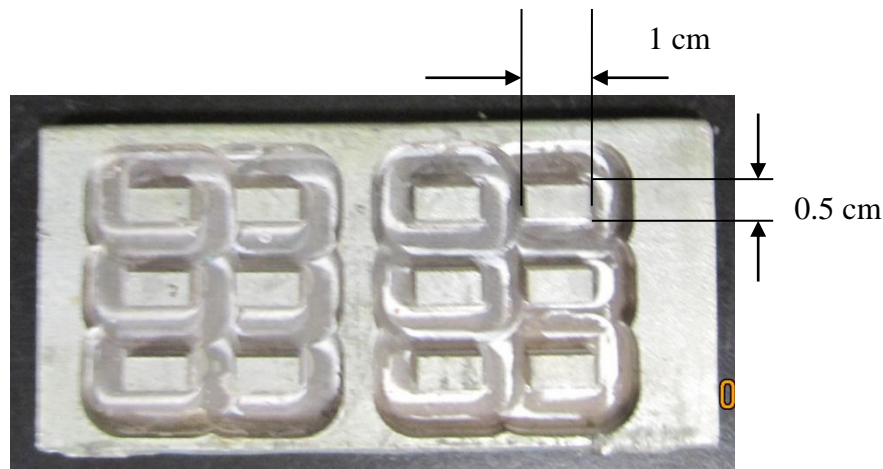


Figure 9.- Galvanized steel plate after CNC machining.

After the CNC finished machining the galvanized steel plates, the electrodes were cut with an abrasive wheel. Water was used to keep the plate cool during the cutting of the electrodes. In this step of the process, the electrodes were cut as close as

possible to the electrodes. The edges of the electrodes were then detailed with a grinder.

The final step in the processing of the galvanized steel electrodes consisted in machining the height of the electrode to a height of 0.170 in. This step is used to ensure the electrode will be flushed after the press fitting into the Delrin pocket with a depth of 0.20 in. along with the copper cable used for data acquisition. The machining of the height of the electrode also allows the copper wire to have contact with steel instead of zinc, which improves the conductivity between the electrode and the wire.

3.2 Delrin coupon preparation

A 1 1/4 in. diameter delrin rod was cut into segments of 2 in. of length and the sections are then machined with a CNC programmed to create a ridge of 0.02 in. and 3 pockets of 1 x 1/2 cm. and 0.2 in. in depth. The delrin rod was phased with a 1 in. two flute end-mill, and the pockets were machined with 1/4 in. 4 flute end-mill. And then detailed with a 1/8 in. 4 flute end-mill. During the machining of the Delrin coupon, coolant was used to prevent the Delrin from burning. The 2 in Delrin sections are machined on both sides.

After the segments have been machined on both sides, they were cut in half with a vertical saw to create two separate Delrin coupons. The final height of the Delrin coupons was machined with a milling machine. The reason for reducing the height in the laid machine before using the milling machine is due to the elasticity of the material. If the feeding of the material is too much in the milling machine, it would rip the coupon out of the bice. Finally, the holes to insert the copper cables into the Delrin coupon were machined with a milling machine and a 1/16 in. bit, as shown in Figure 10.



Figure 10.- Above, above view of a finished electrode coupon. Below, side view of a finished electrode coupon with cable holes.

3.3 Electrode coupon assembly

Before the working electrode was press fitted into the Delrin coupon, the edges of the working electrode were slightly ground to enhance the guiding of the electrode through the Delrin during the press fitting process. The electrodes were cleaned in an ultrasonic cleaner with acetone for 30 minutes to remove any contaminants that remained from the machining process. The Delrin coupons were also cleaned with acetone. The copper wire was inserted into the coupon and spread inside the pocket to ensure good contact with the electrode. Prior to press fitting of the electrode, two drops

of epoxy were poured into the coupon's pocket to seal the electrode sides and prevent crevice corrosion. The electrode was press fitted carefully so the galvanized steel was not damaged in the process. After the electrodes were press fitted, pressure was applied with a hydraulic press to ensure the electrodes are driven to the bottom of the Delrin pocket. Finally the electrodes were cleaned with a cotton cloth saturated with acetone to remove any epoxy that may have made it to the electrode's surface. After some time has been allowed for the epoxy to dry (2 to 3 hours), the cables were sealed so that they do not corrode during the experiments.

3.4 Electrode positioning structure

A plexiglass structure was built to allow for the accommodation of the electrodes inside a 1 liter beaker glass, as shown in Figure 11. This structure ensured that the electrodes were always in the same position during the electrochemical experiments. The plexiglass structure also aids to position the counter electrode in a mesh position with the reference electrode in the middle of the counter electrode.

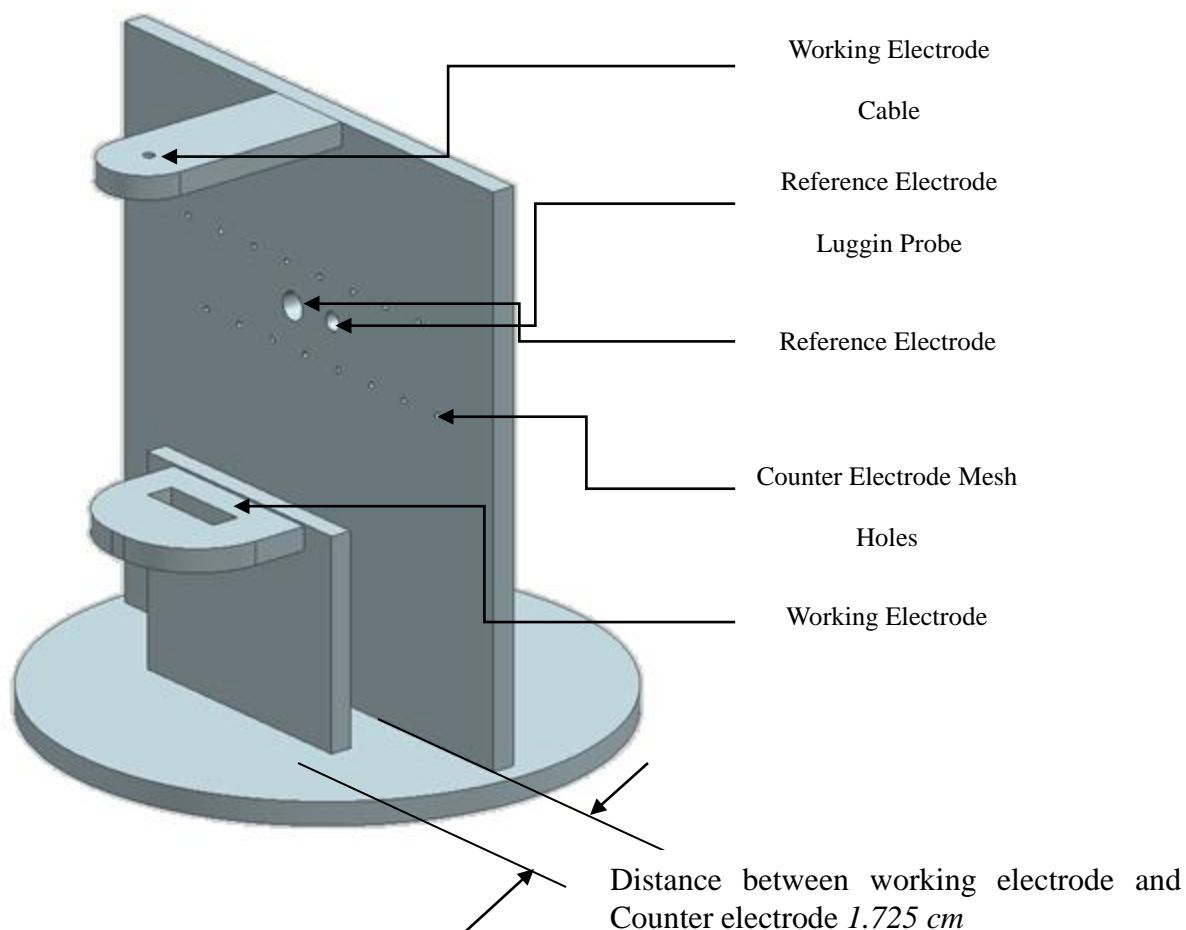


Figure 11.- Electrode positioning structure

3.5 Polarization scan experiments setup

Polarization scans were acquired at different NaCl molarities to acquire electrochemical data that would allow for the calculation of corrosion current rates, mass loss and MPY. The electrode potential was measured between the working electrode and the reference electrode. The polarizing current was measured between the working electrode and counter electrode which is very commonly an inert noble metal. The polarization scans provided showed the Tafel behavior of the system consisting of the anodic and cathodic polarization curves which ideally are symmetric

about E_{corr} when $|\beta_a| = |\beta_c|$, as shown in Figure 12. However for corroding metals, the Tafel slopes are almost never equal because of the different anodic and cathodic half cell reactions which compose the mixed potential E_{corr} . The polarization scans were performed with galvanized steel as the working electrode, Ag/AgCl saturated with KCl as the reference electrode and a Pt wire as the counter-electrode.

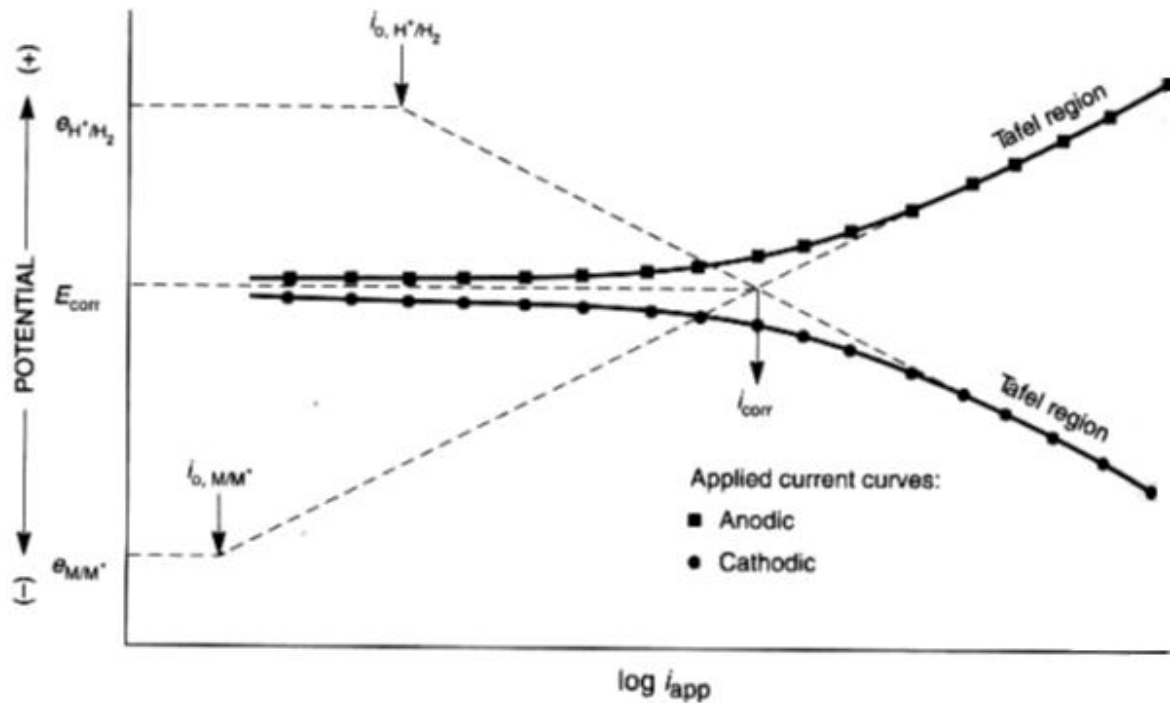


Figure 12.- Ideal polarization curve and tafel slopes (Jones 1992)

3.6 Electrochemical impedance experiments setup

The electrochemical impedance measurements were acquired to obtain the solution resistance at the respective molar concentration, as well as the polarization resistance. The electrochemical impedance experiments characterize the electrochemical behavior of the electrode to create an electric equivalent circuit representing the metal/solution interface and interphase. The equivalent circuit consists

of a C, that is a frequency independent property and depends only on the electrode potential, an electrolytic resistance, R_s , between the reference electrode and the working electrode, and a complex faradic impedance, polarization resistance (R_p), caused by a transfer electrode reaction, as shown in Figure 13.

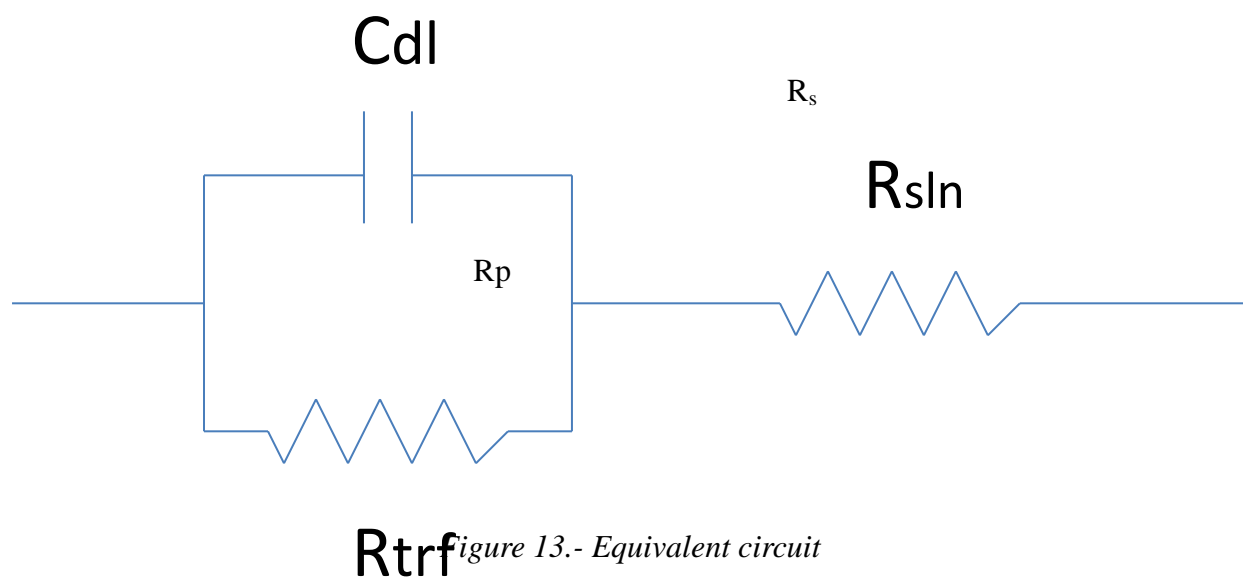


figure 13.- Equivalent circuit

The setup for the electrochemical impedance experiments used the same electrode structure (Figure 11) as the polarization scan experiments. For the reference electrode, a Pt electrode contained in a Luggin-probe was connected in parallel to an Ag/AgCl reference with a 100 μ F capacitor. This modification to the reference electrode allows the stabilization of the electrochemical impedance measurements at high frequencies. The necessity for this modification was brought upon by problems such as the phase shift introduced by the potentiostat and problems at high frequencies due to the resistance and capacitance of the fiber tip of the reference electrodes (Mansfeld, Lin, et al. 1988). Figure 14 shows the connection setup of the potentiostat and frequency response detector in the electrochemical impedance experiments.

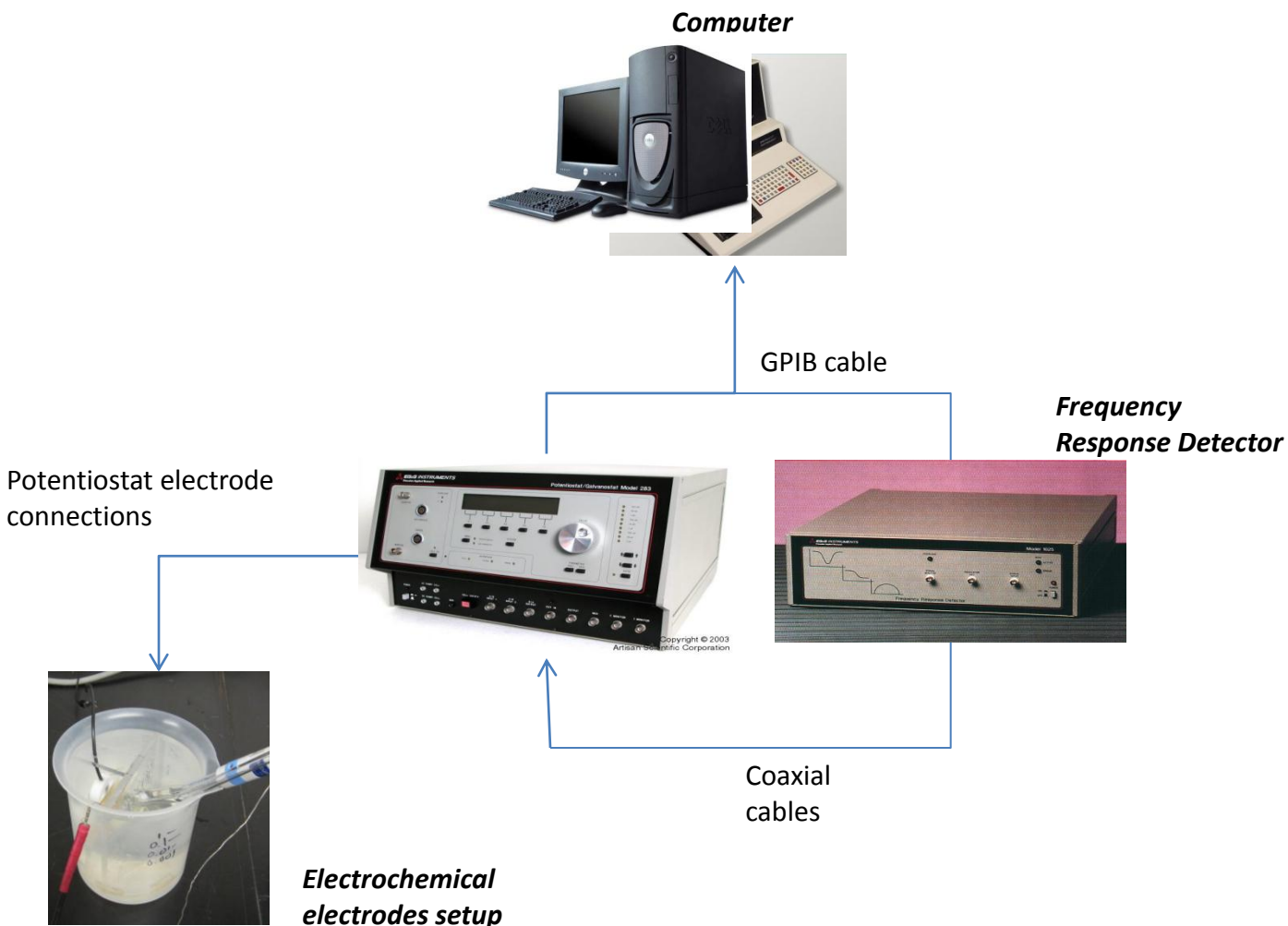


Figure 14.- Potentiostat and frequency response detector connection setup.

3.7 Electrochemical noise experiments setup

The setup for the electrochemical noise experiments consisted on measuring current and voltage during wet and dry cycles in soil. The electrode coupon was composed of three galvanized steel electrodes working as the reference electrode, the counter electrode and the working electrode. Current was measured between the working electrode and the counter electrode; the potential was measured between the working electrode and the reference electrode, the third electrode.

The electrochemical noise setup is composed of two separate circuits, as shown in Figure 15. The circuit to acquire the voltage noise signals included a 10 M Ω connected to the working electrode to dissipate probable parasitic capacitance. The voltage signal obtained between the working and reference electrodes is then connected to a buffer amplifier to simplify data acquisition. The circuit to acquire the current noise signals used the counter-electrode being grounded. The current signal then passed through an operational amplifier with a 10 k Ω resistance. The resultant signal finally passed through a buffer amplifier to improve the data acquisition.

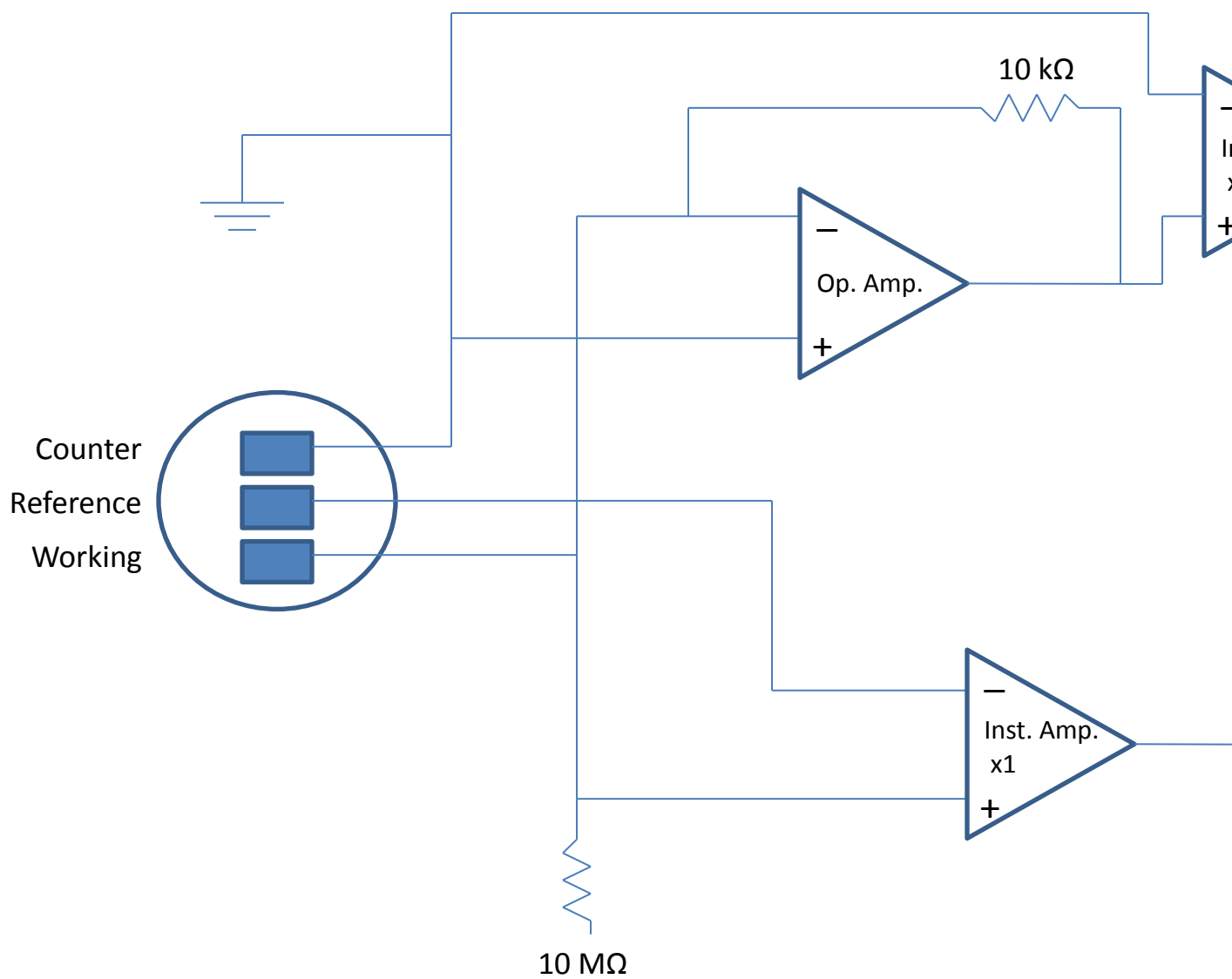


Figure 15.- Circuits used to acquire current and voltage electrochemical noise simultaneously.

Chapter 4: Results and Discussion

4.1 Electrochemical Impedance Spectroscopy

Electrochemical impedance spectroscopy was performed for galvanized steel immersed in aqueous solutions containing 0.0001, 0.001, 0.01 and 0.1 M NaCl. To emulate the real time corrosion behavior of the galvanized steel in the soil, special attention was given to the results at the lowest molarity possible (0.0001 M NaCl), since it is the closest to the chloride content of the soil.

The polarization resistance and solution resistance obtained from the Bode plots shows the difference in solution conductivity as well as the changes in corrosion rates as the chloride content increases. Bode and Nyquist plots were obtained for the NaCl contents ranging from 0.1 to 0.0001 M NaCl and the plots have been averaged. A typical plot is shown in Figure 16. The Bode plots were obtained three times to verify the reproducibility of the results and averaged at each molarity to provide a more accurate result. The solution resistance at different molarities is shown in Figure 17. The linearity of the results in the solution resistance in the logarithmic graph demonstrates the consistency in the results. The inverse of the polarization resistance as measured with respect to the molarity is shown in Figure 18. The polarization resistance plateaus at chloride content less than 0.001 M NaCl.

The resistivities with respect to the solution molarity were calculated by dividing the solution resistance acquired from EIS measurements with the spacing between the working electrode and the reference electrode. The resistivity obtained from the solution extracted from the real time corrosion experiments in soil from Odessa after running the wet/dry cycles for 15 months are shown in Table 1. The value of the resistivity from the

solution obtained from the real time corrosion experiments falls between the resistivity for 0.0001 and 0.001 M NaCl. But the resistivity is significantly closer to the resistivity at 0.0001 M NaCl.

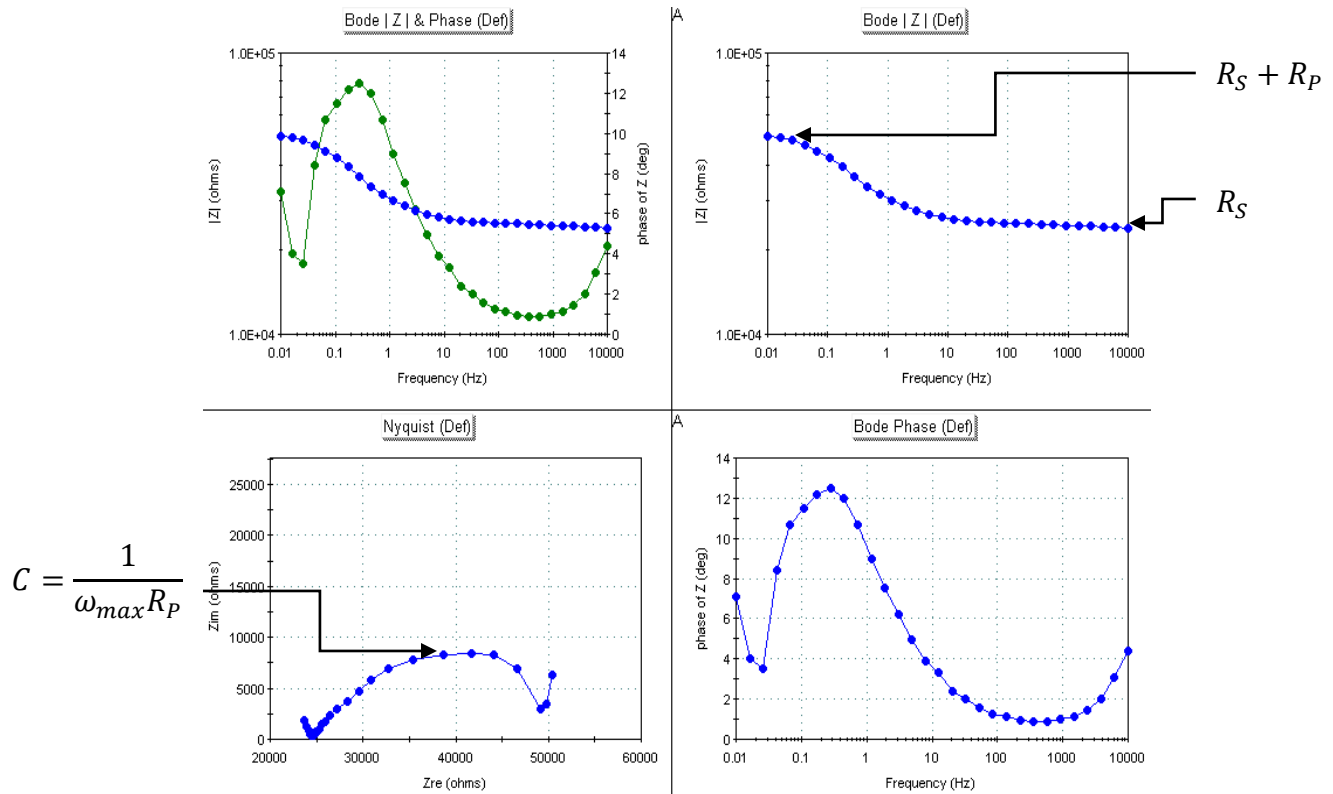


Figure 16.- Bode and Nyquist plot of galvanized steel at 0.0001 M NaCl. Acquired with PowerSINE

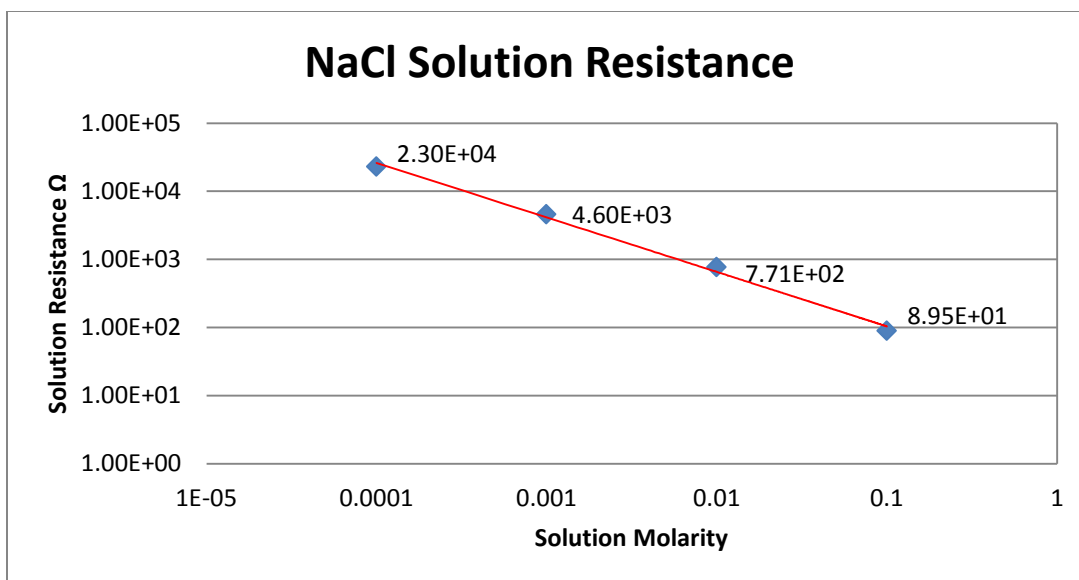


Figure 17.- Solution resistance at different NaCl molarities. Acquired with PowerSINE.

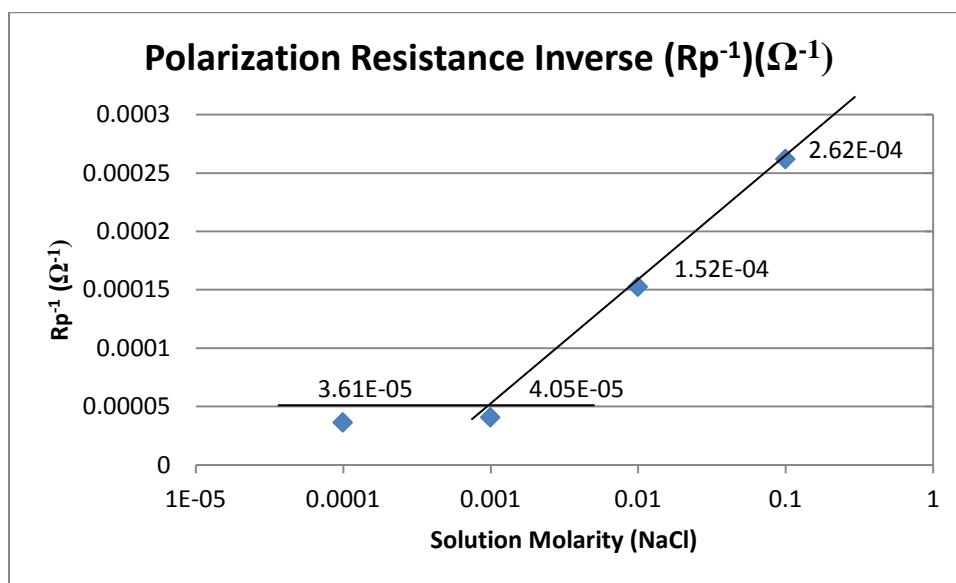


Figure 18.- Inverse of polarization resistance with respect to the solution molarity. Acquired with PowerSINE

Table 1.- Resistivities with respect to the solution molarity in addition to the resistivity of Odessa soil solution after 15 months.

Molarity	Resistivity (Ω cm)
0.0001	3.97E+04
Odessa Soil	2.10E+04
0.001	7.94E+03
0.01	1.33E+03
0.1	154.3875

A one time-constant equivalent circuit was measured for the electrochemical impedance data acquired for a 0.0001 M NaCl solution. The time constant was obtained through the Bode and Nyquist plots in Figure 16. The equivalent circuit is composed of a solution resistance (R_s), a polarization resistance (R_p) and the double layer capacitance (C). As shown in Figure 19.

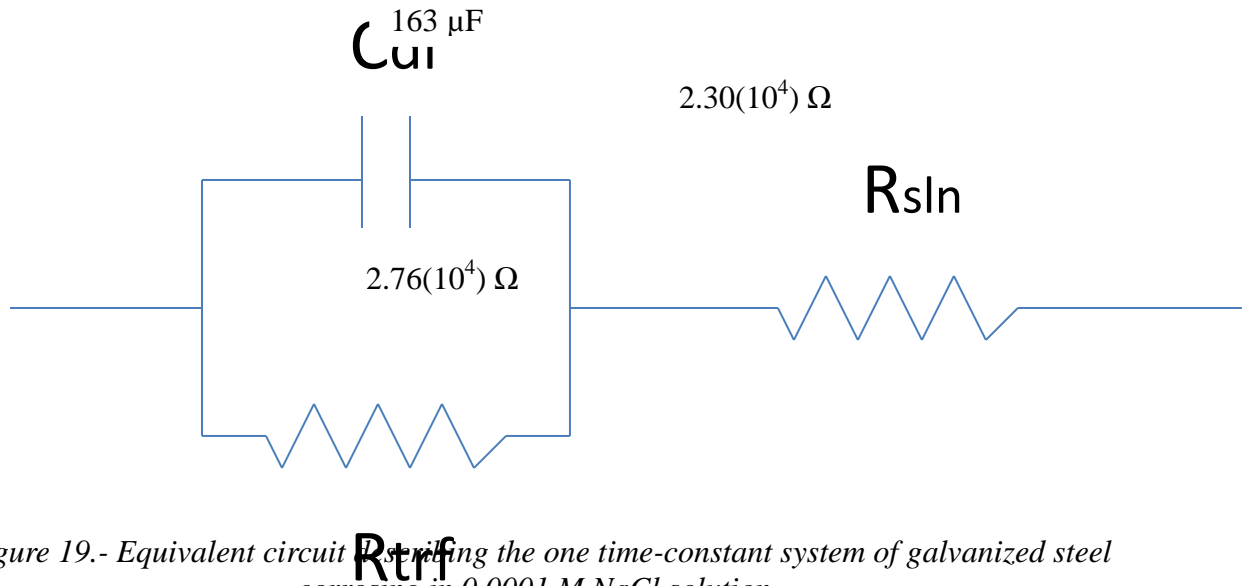


Figure 19.- Equivalent circuit describing the one time-constant system of galvanized steel corroding in 0.0001 M NaCl solution.

The polarization curve was obtained at different molarities to calculate the corrosion rate of galvanized steel at different concentrations, as well as the milli-inches per year (MPY) and the mass loss during the corrosion of the material. Special attention

was provided at the results at 0.0001 M NaCl because the concentration is closer to the actual chloride concentration of the soil in wet environment. The water used for the solution for the acquisition of the polarization curve is the same as the water used for the real time corrosion experiments with soil. The Tafel slopes were calculated at a low scan rate (0.1 mV/sec) to allow the half reactions to occur in the surface of the galvanized steel in the low molarity solution. The Tafel slopes were calculated as well as the corrosion potential. From the polarization curve, the Tafel slopes allowed for the calculation of the “k” constant.

$$k = \frac{b_a b_c}{2.303(b_a + b_c)}$$

The “k” constant along with the inverse of the polarization resistance allows for the calculation of the current density. With the current density of the system, the mass loss of the galvanized steel can be obtained. Figure 20 shows a typical polarization curve (e.g., 0.0001 M NaCl) with the Tafel slopes and the corrosion potential. The corrosion rate in terms of mils lost per year (MPY) was also calculated for the galvanized steel at the different NaCl molarities.

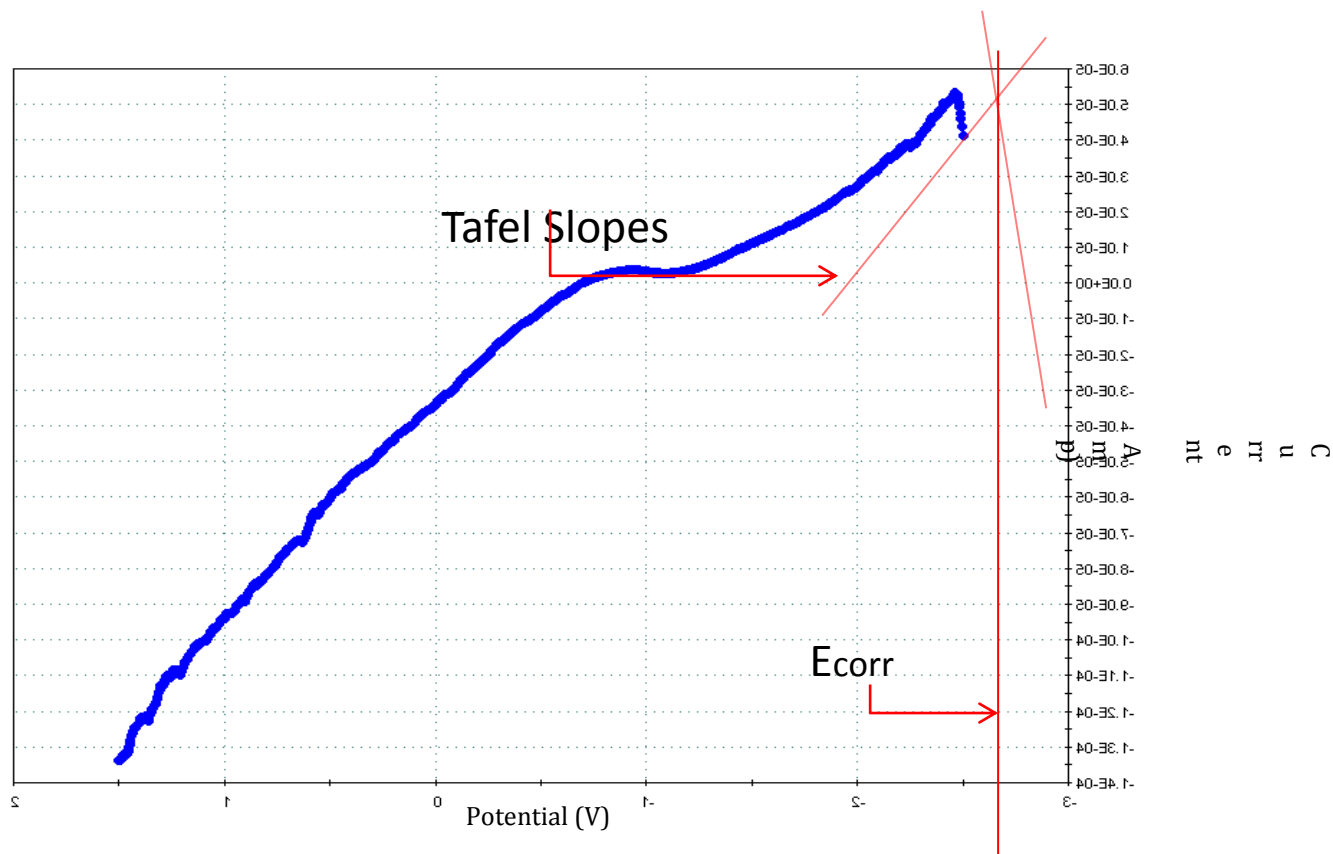


Figure 20.- Polarization curve of galvanized steel in 0.0001 M NaCl. Acquired with PowerCV.

Table 2 shows the Tafel constants determined from the polarization curve for galvanized steel, as well as the calculated corrosion parameters at 0.0001 M NaCl solution and other NaCl molarities.

Table 2.- Corrosion rate results for galvanized steel at different NaCl molarities.

Molarity	ba (V/decade)	bc (V/decade)	Rp (Ω)	k	icorr (Amps/cm ²)	ΔM (gr/cm ²)	MPY (mils/year)	$\mu\text{m/yr}$
0.1	0.555	1.3	3820	0.17	8.84E-05	8.63E-04	37.484	952.09
0.01	0.67	0.61	6560	0.14	4.23E-05	4.13E-04	17.919	455.13
0.001	0.065	0.395	11500	0.02	4.21E-06	4.11E-05	1.787	45.38
0.0001	1.44	0.024	27666	0.01	7.41E-07	7.23E-06	0.314	7.98

Figure 21 shows the change in the current density as the NaCl molarity of the solution increases. And Figure 22 shows the changes in MPY (Mils/yr) as the molarity increases. Similarly Figure 23 shows the change in μm lost per year in the coating. The changes from 0.0001 to 0.001 M NaCl are significantly small compared to the changes from 0.001 to 0.01 M NaCl or the changes from 0.01 to 0.1 M NaCl. These changes were expected since the increment in chloride concentration from 0.0001 to 0.001 M NaCl is very small (~ 0.0525 gr/L).

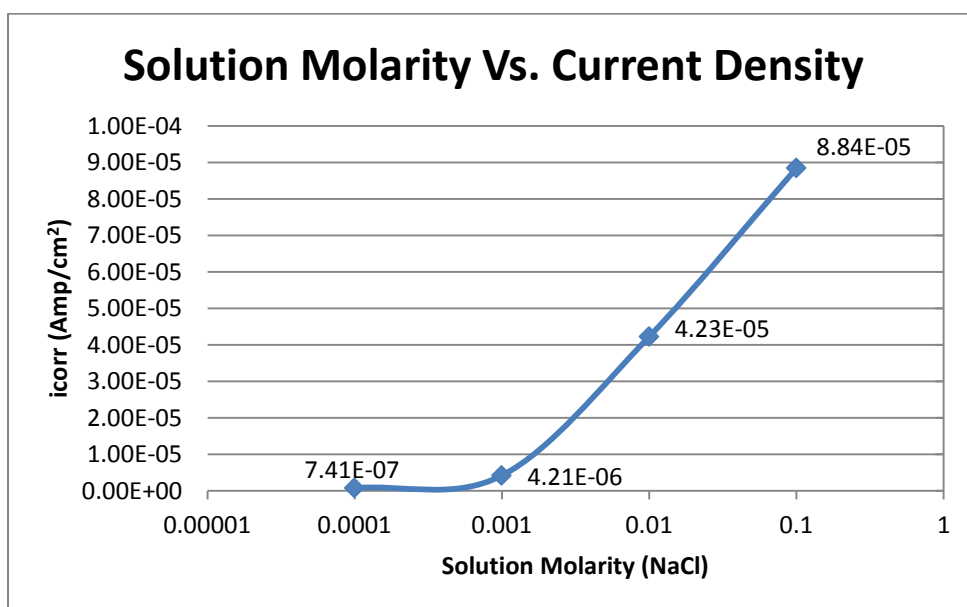


Figure 21.- Change in current density as the NaCl molarity increases.

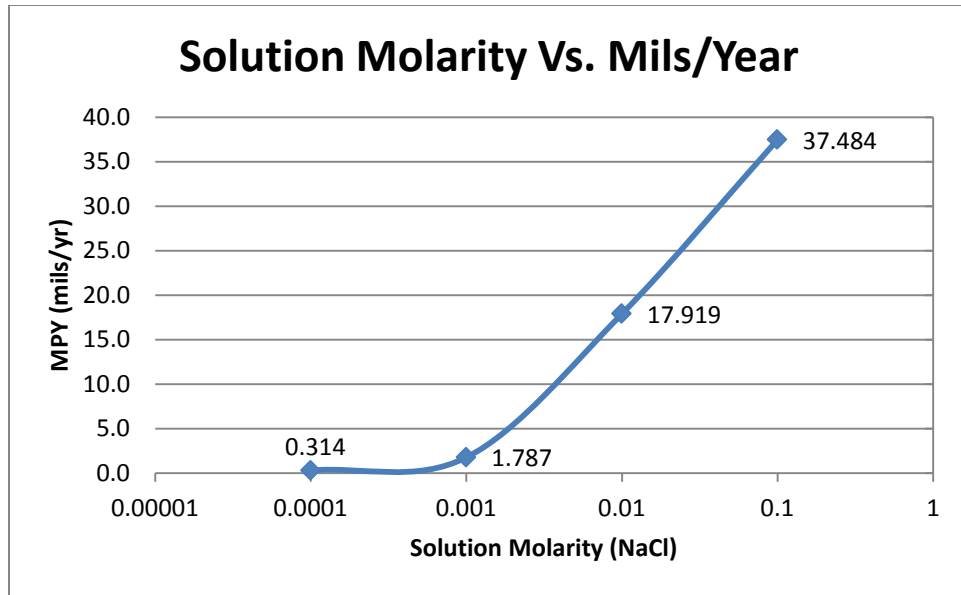


Figure 22.-Change in MPY as the NaCl molarity increases.

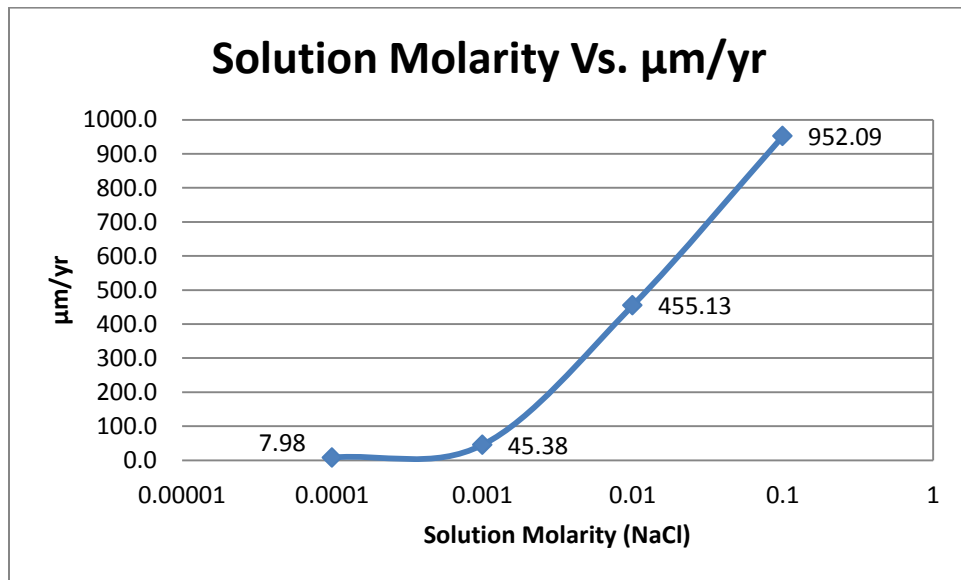


Figure 23.- Change in $\mu\text{m/yr}$ as the NaCl molarity increases.

Figure 24 demonstrates the Elias graph which shows the corrosion rate of zinc in $\mu\text{m/yr}$. The graph also includes the corrosion rate of zinc at 0.0001 and 0.001 M NaCl. The corrosion rate for 200 ppm Cl (0.0002 M Cl) is located between the corrosion rates at 0.0001 and 0.001 M NaCl (45.38 and 7.98 μm respectively).

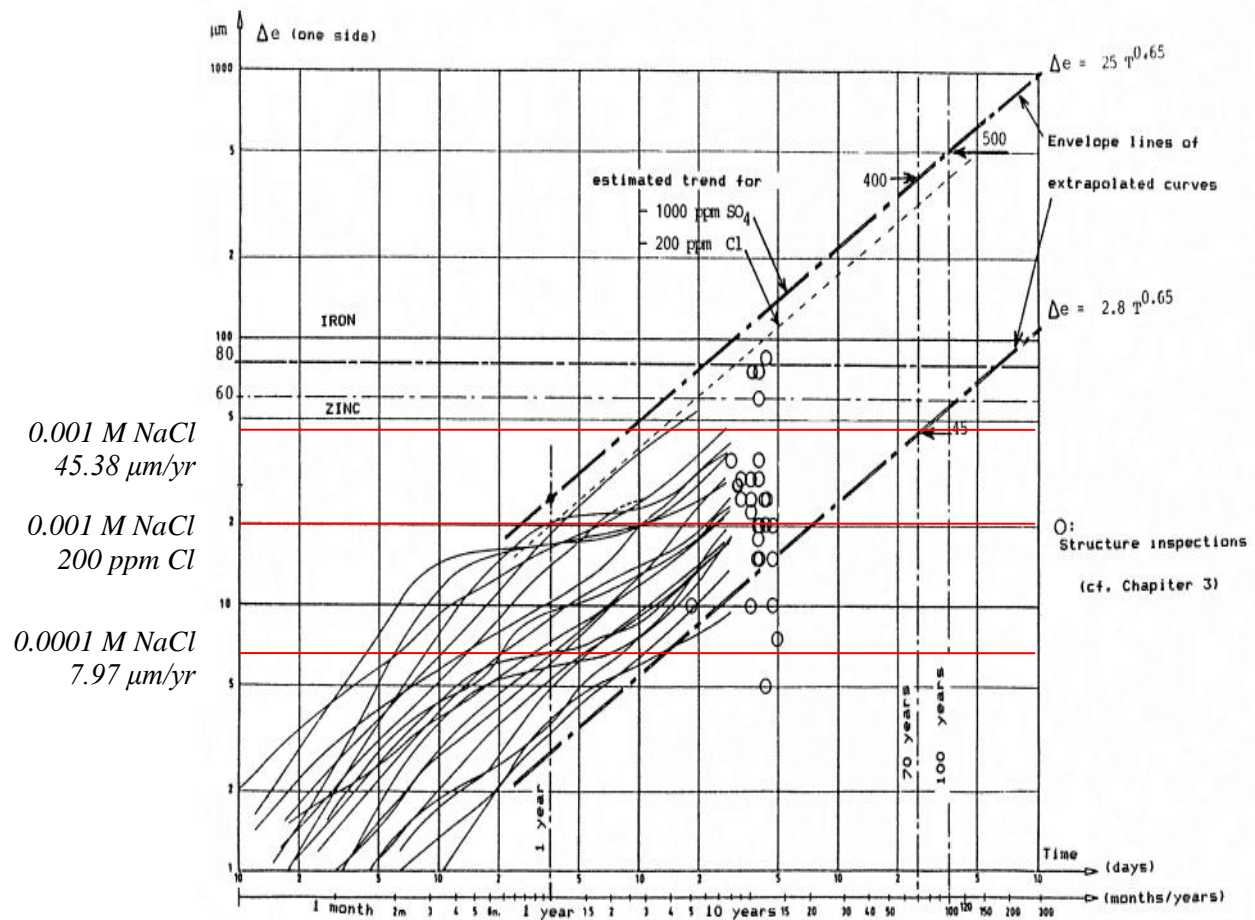


Figure 24.- Elias' diagram showing the corrosion rates for zinc at 0.0001 and 0.001 M NaCl and 200 ppm Cl (0.0002 Cl).

4.2 Voltage/Current Response at Low Chloride Contents

An experiment was conducted to measure the voltage and current response of the system with a galvanized steel electrode as a working electrode, a platinum wire as a counter electrode and an Ag/AgCl with saturated KCl reference electrode. The solutions were prepared with triple distilled water to minimize the errors in measurements from contaminants. This experiment was conducted to show the difference in voltage and current when the chloride content in the solution was extremely low (< 0.0001 M NaCl).

The experiment showed that during the change from 0.00001 M NaCl to 0.0001 M NaCl, the change in potential and current is negligible as shown in Figure 25 (potential) and Figure 26 (current). Therefore, the solution molarity of 0.0001 M NaCl is used to compare to the chloride concentration in the soil.

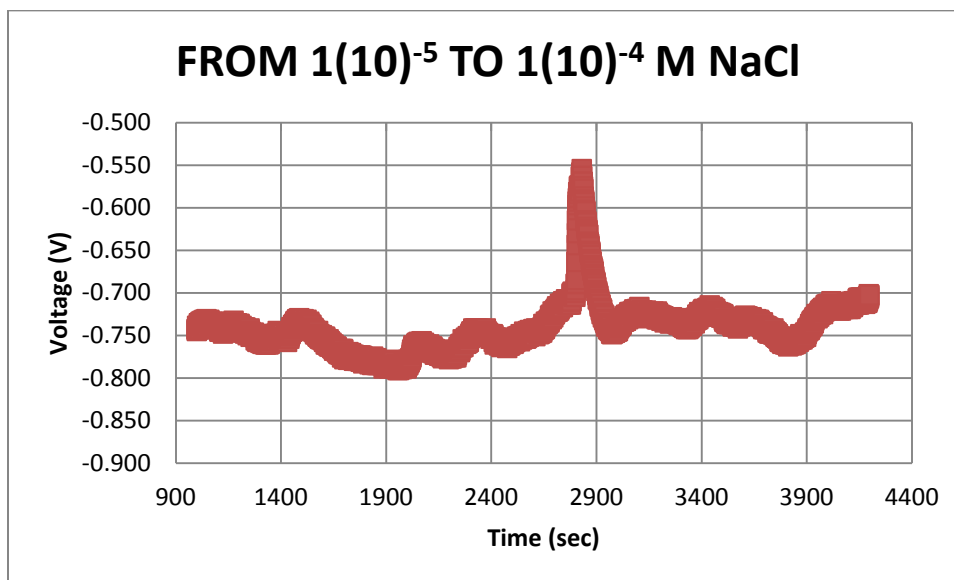


Figure 25.- Change in potential from 0.00001 to 0.0001 M NaCl

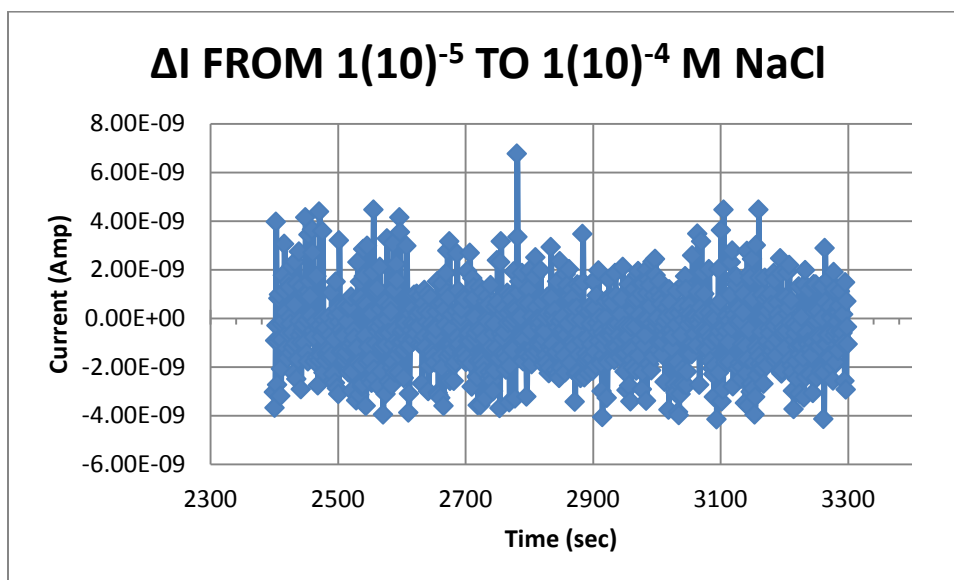


Figure 26.- Change in current from 0.00001 to 0.0001 M NaCl

4.3 Electrochemical Noise

The current and potential noise on cycles of wet and dry was recorded for several months and was analyzed by calculating the power spectral density (PSD). The PSD was calculated through fast Fourier transform (FFT) and through maximum entropy method (MEM). The PSD was obtained through MEM to support the results obtained through FFT and also to obtain a smoother spectrum which can also describe the corrosion behavior of the system.

The electrochemical noise analysis was performed in a sample of the data to explain the interpretations possible from the acquired results. The sample data has to be in the order of a power of 2, so the number of sample data was chosen to be 1024 to simplify the analysis and obtain a clearer spectrum. Figure 27 shows an example of the voltage data obtained from galvanized steel in wet/dry cycles buried in Odessa's soil. Figure 28 shows the correspondent current noise data for the specific specimen. The specimen was underground during the wet/dry cycle experiment for about 280 days.

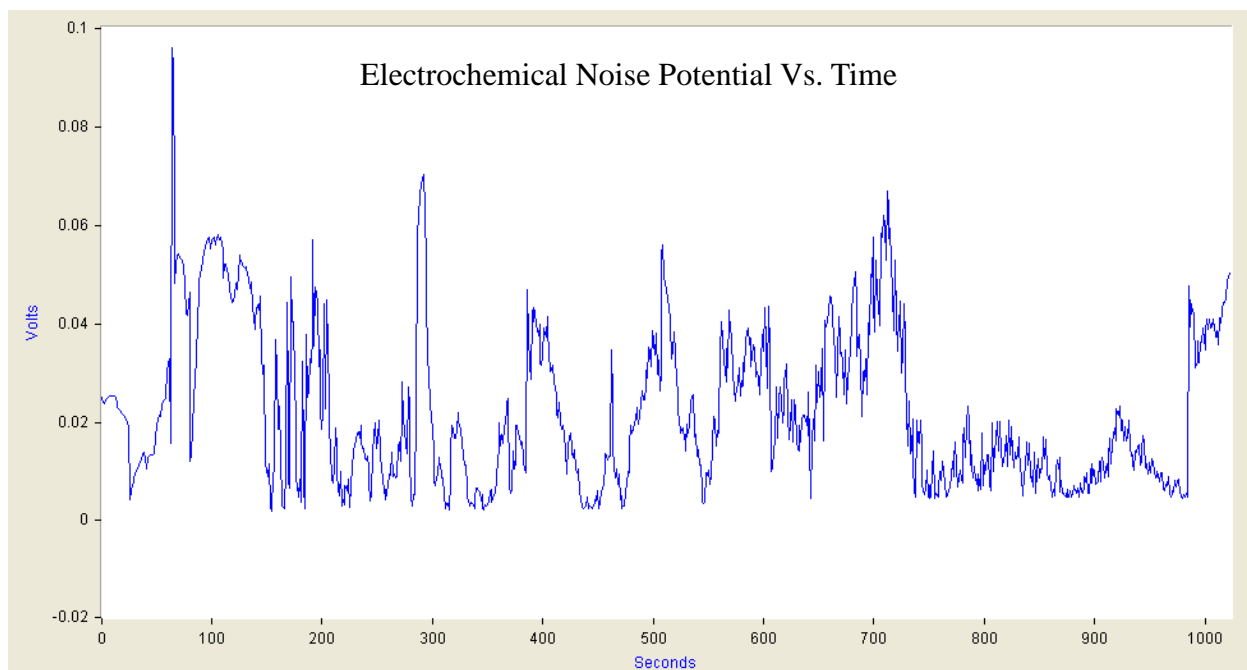


Figure 27.- Potential electrochemical noise data corresponding to Odessa. (1024 points sample).

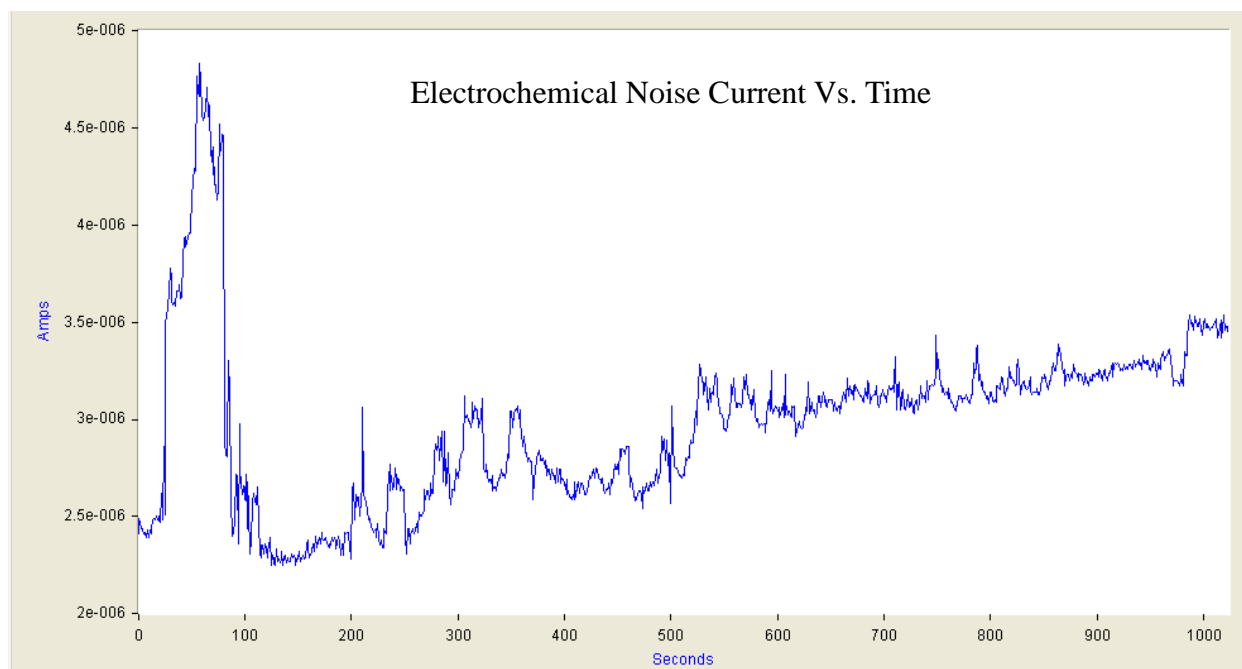


Figure 28.- Current electrochemical noise data corresponding to Odessa. (1024 points sample).

The rate of acquisition of the data for electrochemical data is 40 minutes. This

fact causes the frequency to be shorter than it would normally be in similar studies.

Figure 29 shows the PSD acquired from the fast Fourier transform (FFT) for a sample data of 1024 samples from the potential electrochemical data from Odessa. Figure 30 shows the PSD acquired from the maximum entropy method (MEM) for the same sample data in question. The PSD acquired from the MEM estimates the spectrum by calculating poles. The more poles were used the closer it will acquire the PSD from the FFT for the same data. The extrapolation of data to improve the frequency resolution is an advantage provided by the MEM method of PSD calculation. Figure 31 shows the PSD acquired from both FFT and MEM, the graph shows that the MEM acquired PSD has a level high enough to simulate the FFT acquired PSD.

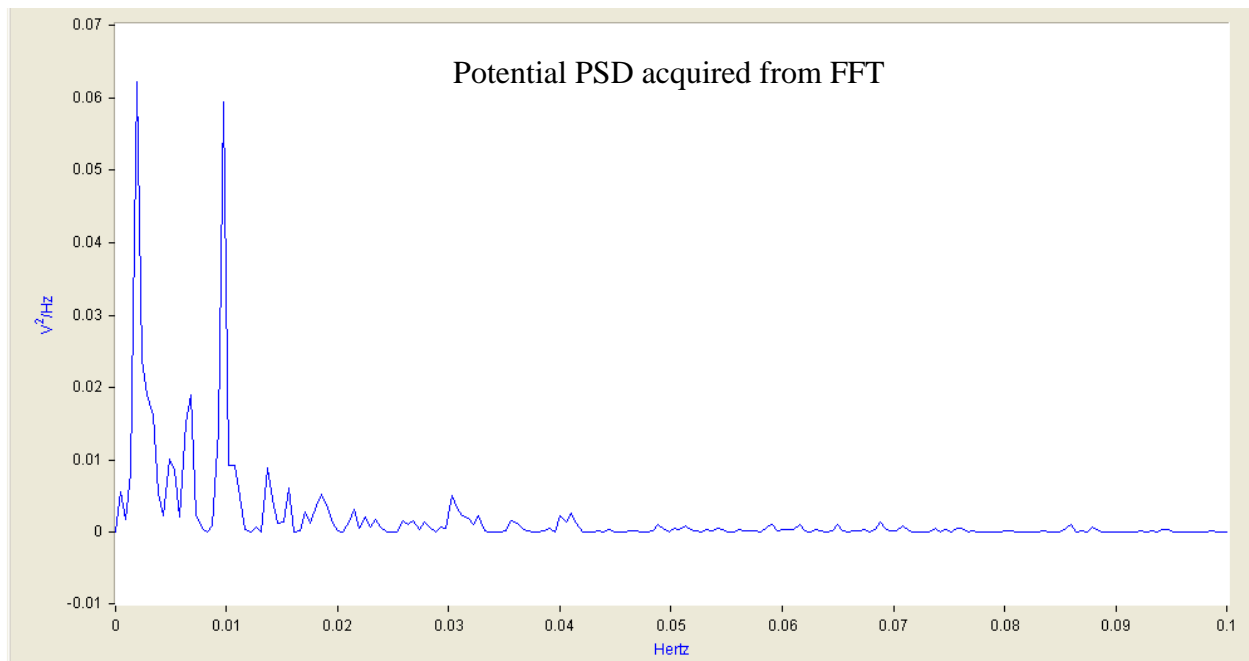


Figure 29.- Potential PSD acquired from the FFT for a 1024 sample from Odessa's data. Acquired with Dadisp.

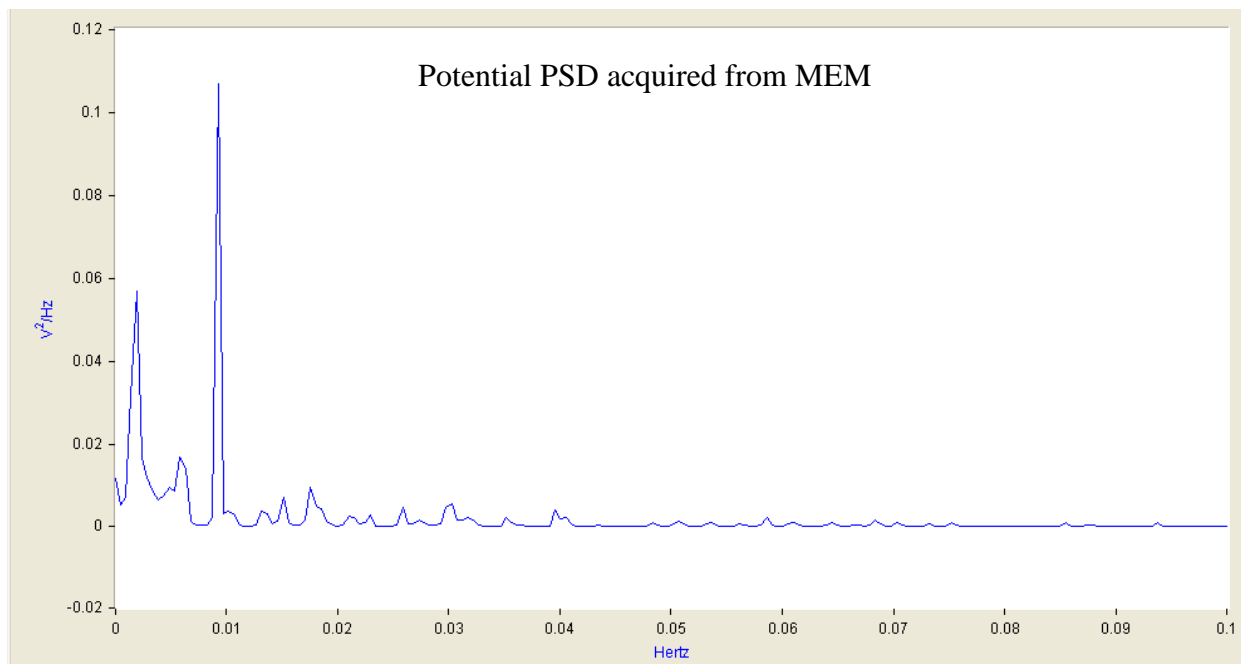


Figure 30.- Potential PSD acquired from MEM for a 1024 sample from Odessa's data. Acquired with Dadisp

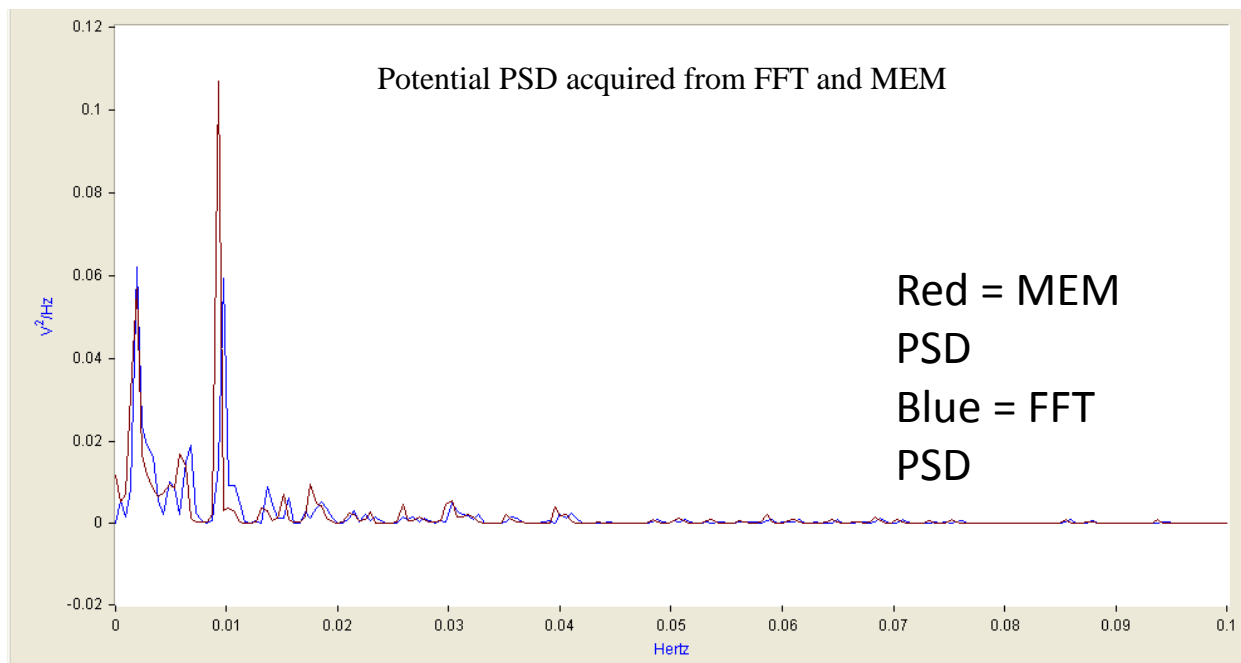


Figure 31.- MEM acquired potential PSD overlapped with FFT acquired potential PSD. Acquired with Dadisp.

The same analysis was performed to analyze the 1024 sample data from the current electrochemical noise data. Figure 32 displays the PSD acquired from the FFT

method. And Figure 33 shows the PSD acquired from the MEM method for the corresponding current data. Figure 34 shows both PSD in the same graph for comparison purposes. The power spectrum densities for the current noise data proved to be more similar than the PSD acquired for the potential sampled data.

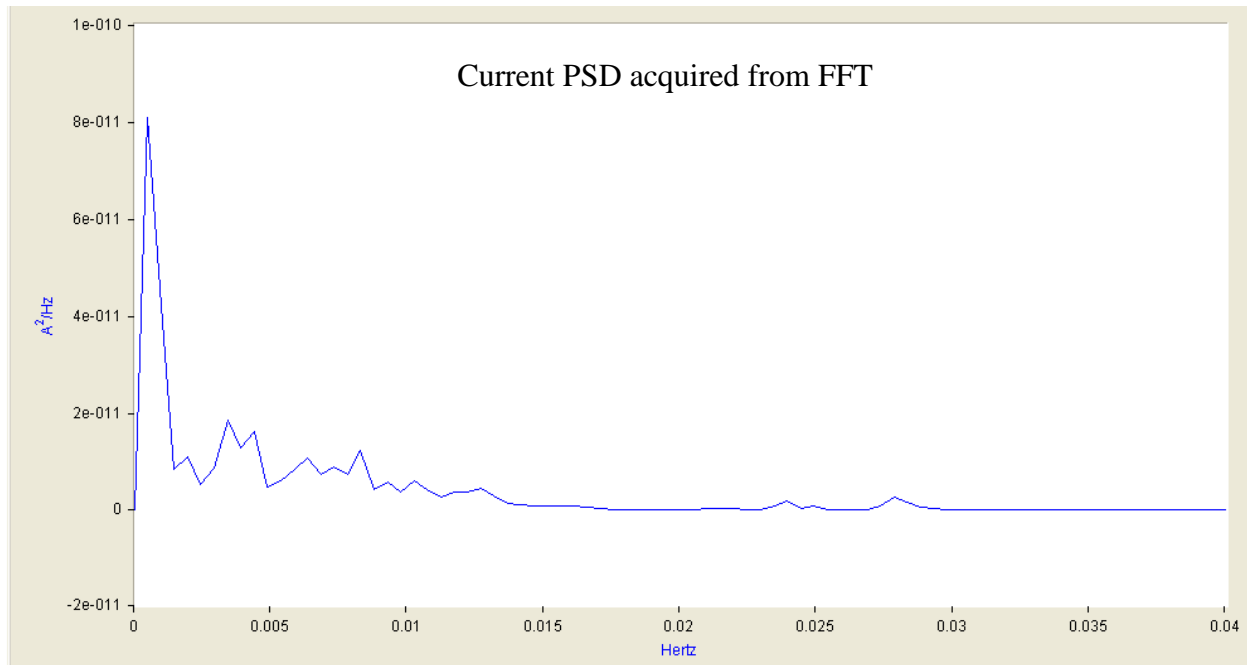


Figure 32.- Current PSD acquired from the FFT for a 1024 sample from Odessa's data. Acquired with Dadisp.

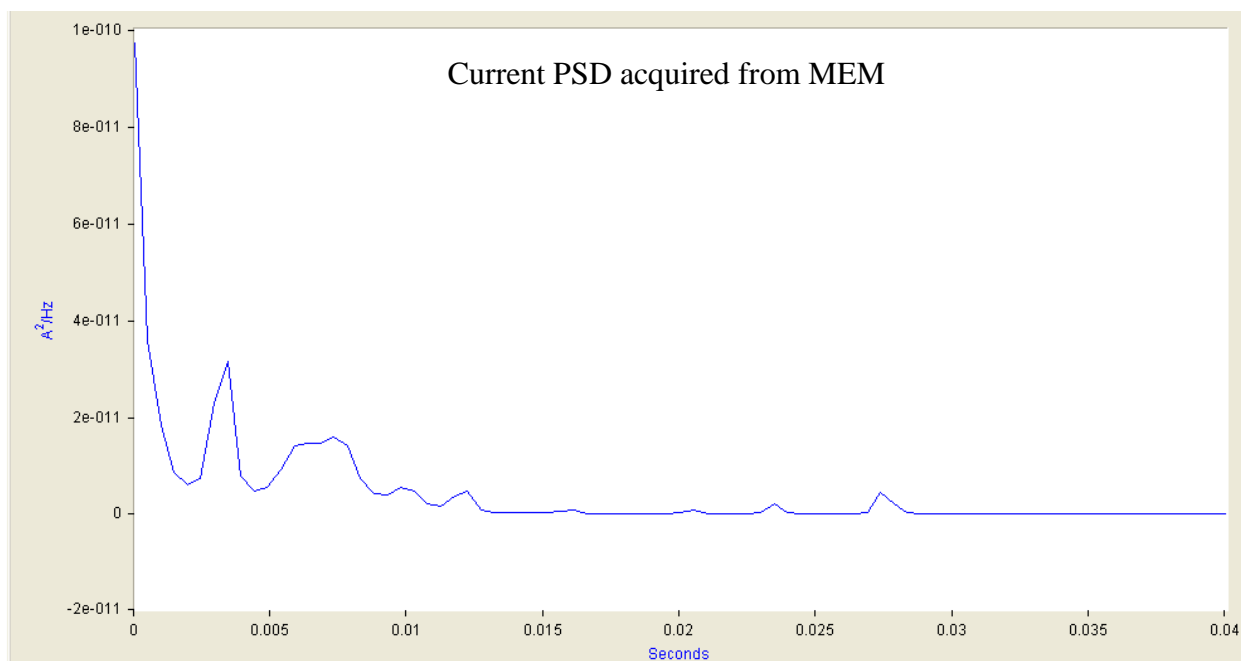


Figure 33.- Current PSD acquired from the MEM for a 1024 sample from Odessa's data. Acquired with Dadisp.

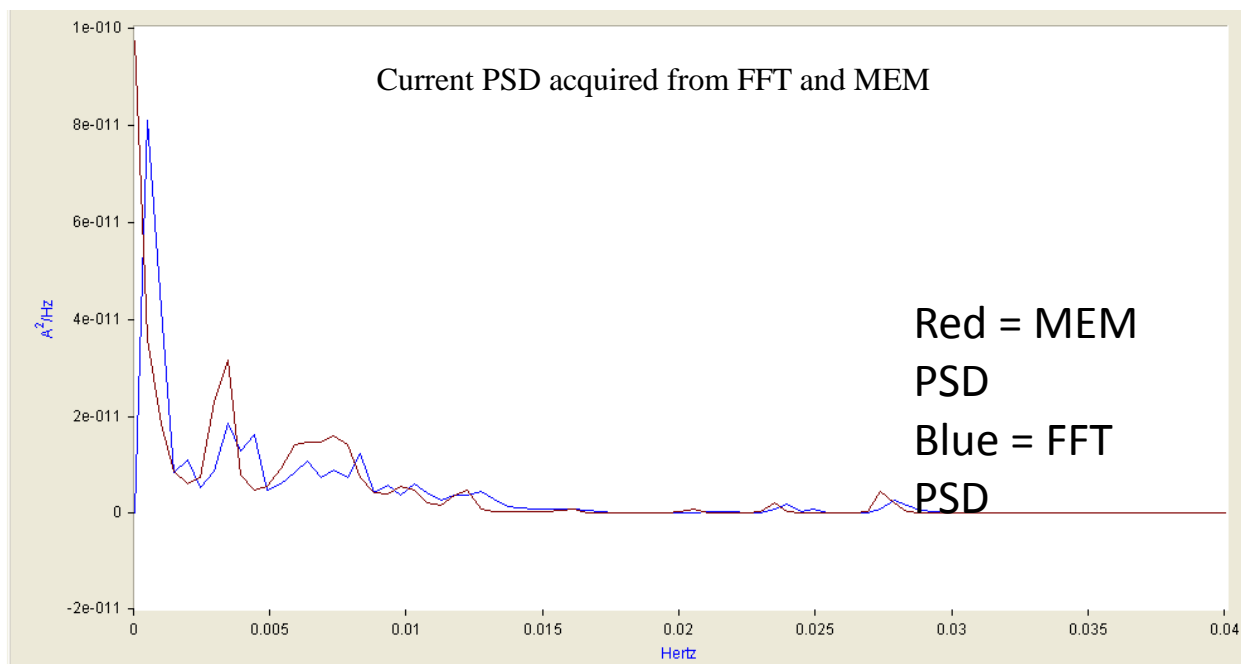


Figure 34.- MEM acquired current PSD overlapped with FFT acquired current PSD. Acquired with Dadisp.

From the electrochemical potential and current noise the noise resistance can be calculated. The noise resistance is acquired by dividing the standard deviation of the

potential by the standard deviation of the current.

$$\text{Noise Resistance} = 36\,899.06\,\Omega$$

Several authors such as Bierwagen, Balbyshev and Mills have considered before the noise resistance to be equivalent to the polarization resistance (Bierwagen, et al. 1994). But these analyses assume that the potential noise can be represented as the action of the current noise on the impedance between the working electrode and the solution, while the working electrode-solution impedance is usually treated as the potential resistance (Cottis 2001).

The electrochemical noise impedance can be calculated similarly to the electrochemical noise resistance. The following equation describes the noise impedance with respect to the potential and current PSD where the impedance is acquired at every valid frequency.

$$\text{Noise impedance} = \sqrt{\frac{\psi_E}{\psi_I}}$$

According to Cottis, it is possible to obtain a realistic estimate for the noise impedance if the potential and current noise is well correlated. However it is commonly assumed that the potential and current noise will be poorly correlated due to the fact that the potential is proportional to the sum of currents from both working electrodes. And the current is proportional to the difference between the two currents. Figure 35 shows the noise impedance acquired from the PSD calculated from the FFT of potential and current noise. And Figure 36 shows the noise impedance acquired with the PSD from the MEM of potential and current noise.

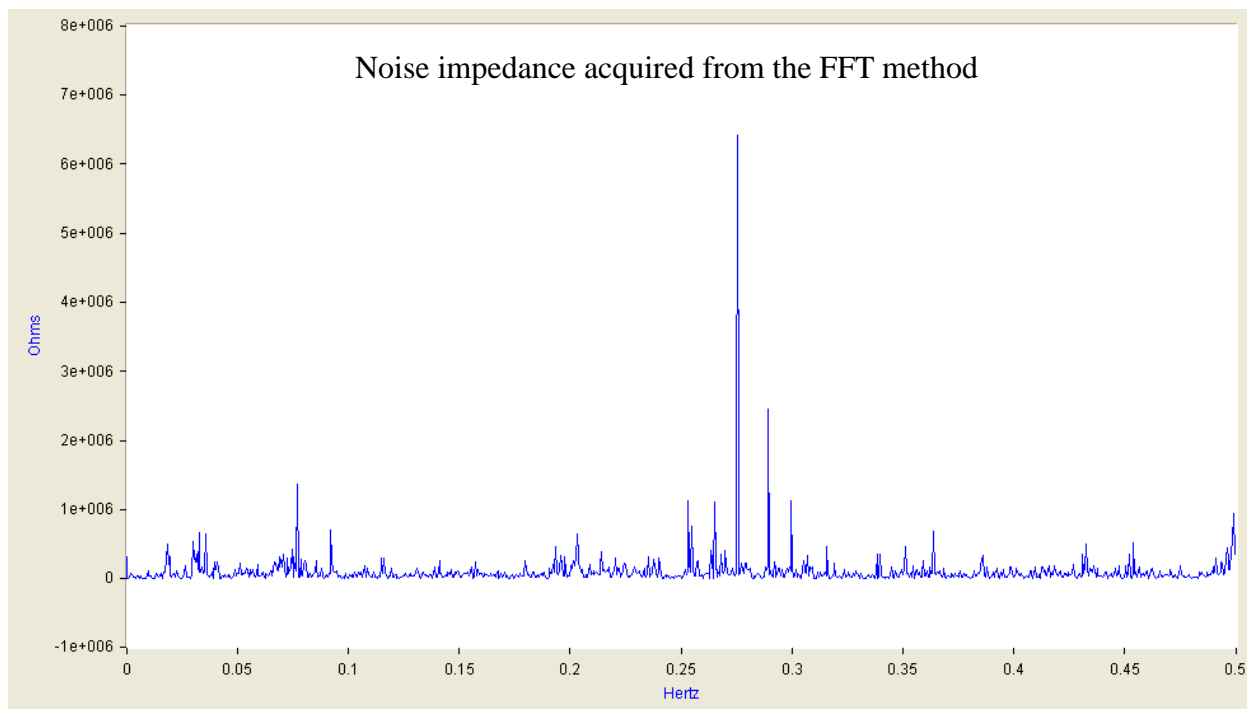


Figure 35.- Noise impedance calculated with the PSD from the FFT of the potential and current. Acquired with Dadisp

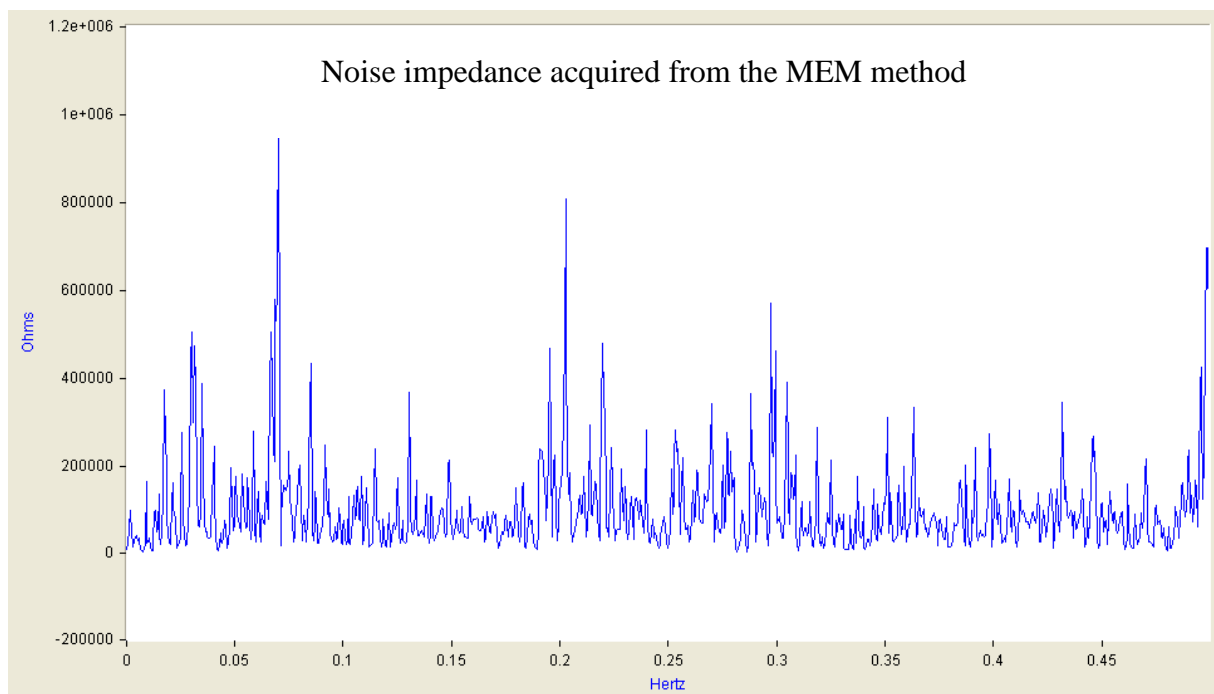


Figure 36.- Noise impedance calculated with the PSD from the MEM of the potential and current. Acquired with Dadisp

4.4 Microstructure and corrosion products

The SEM image in Figure 37 shows the microstructure of the galvanized steel along with the thickness of the zinc coating and the thickness of the Fe-Zn inter-metallic. The thickness of zinc layer approximated $\sim 106\ \mu\text{m}$. And the Fe-Zn inter-metallic showed an average thickness of about $\sim 22\ \mu\text{m}$. Figure 37 also showed a thin layer of what was identified by Marden et al. as the gamma phase. Marden identified the thin layer as being composed of both Γ phase ($\text{Fe}_3\text{Zn}_{10}$) with an iron composition range of 23.5 –28.0 wt% and Γ_1 phase ($\text{Fe}_5\text{Zn}_{21}$) with an iron composition range of 17.0 -19.5 wt%. Followed by the gamma phase is the delta phase. The δ (FeZn_{10}) phase has a lower iron composition range than the Γ phase with 7.0 -11.5 wt%. Finally the zeta phase being the largest phase in the sample has an iron range composition of 5 -6 wt% (Marder 2000). Figure 38 shows the SEM image of the zinc coating of a galvanized steel electrode after being corroded on 0.1 M NaCl solution for 12 hours. The microstructure shows that the galvanized coating underwent a general corrosion reducing the thickness of the coating uniformly in the surface.

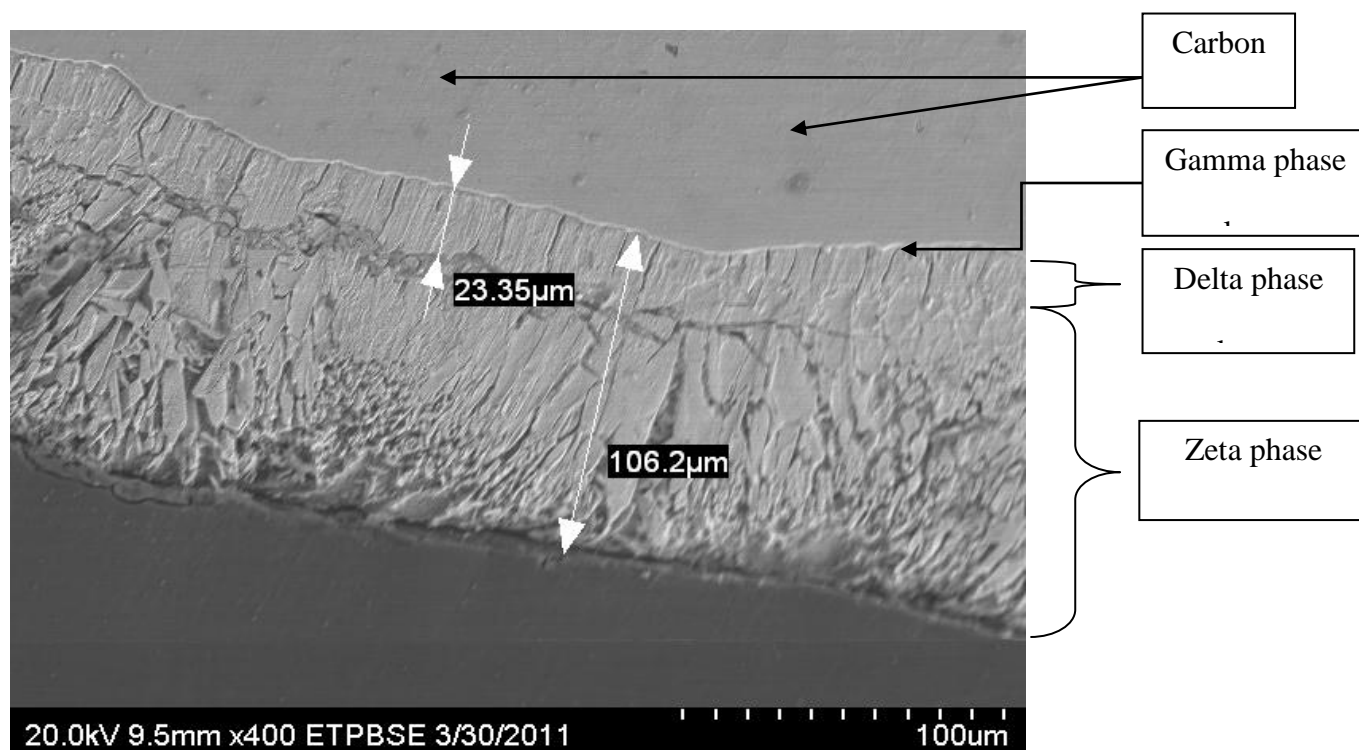


Figure 37.- SEM image of the galvanized steel microstructure.

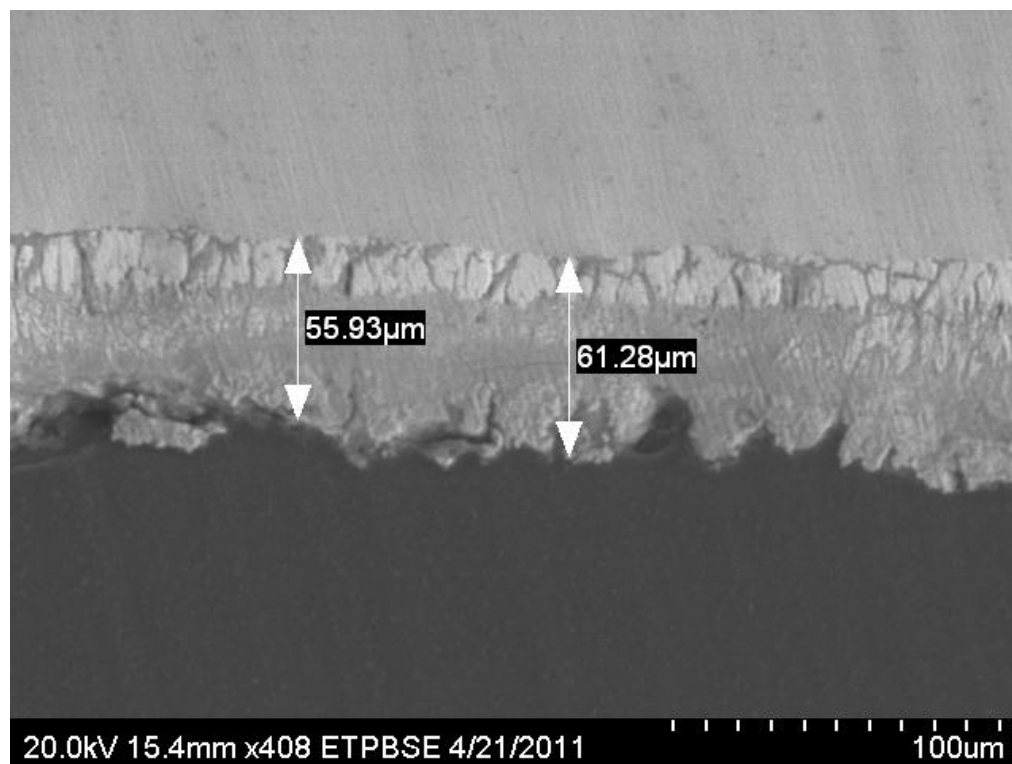


Figure 38.- SEM image of galvanized steel electrode in 0.1 M NaCl solution.

Figure 39 shows a line scan analysis demonstrating the change of elements between zinc and iron across the metallic interface. At a distance range from 0 μm to about 48 μm the weight % of iron is significantly great and the weight % of zinc is almost zero. The slope created at a distance of about 50 μm represents when the iron weight % starts to decrease and the zinc weight % starts to increase. After the slope the weight % of the zinc increases and the weight % of the iron is reduced to about zero.

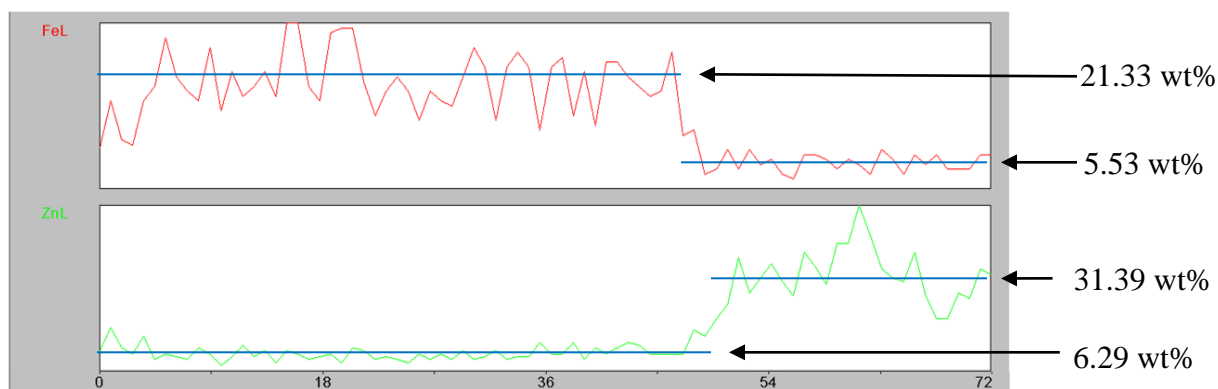


Figure 39.- Line scan analysis of the microstructure of galvanized steel at the Fe-Zn interface.

Elemental area analyses were performed on the microstructure to identify the various elements in the sample. Figure 40 shows the area analysis of the galvanized coating without being corroded. The plot shows that the major elements in the microstructure are zinc and iron as it would be expected as well as some carbon. Figure 41 shows the area that was analyzed in the sample.

Elemental area analyses were also performed on the microstructure of a corroded sample on 0.1 M NaCl solution. The solution was prepared with triple distilled water and was corroded for 12 hours. Figure 42 shows the element analysis in of the microstructure. Figure 43 shows the area that was analyzed in the microstructure. The

analysis shows the presence of chlorine and oxygen in addition to zinc, iron and carbon. The presence of chlorine and oxygen is an indication of the production of corrosion products during the corrosion of the electrode. The corrosion did not reach the steel substrate, which means that the corrosion products must be composed mainly of ZnCl_2 , $4\text{Zn}(\text{OH})_2$, and ZnO as it was identified by Yadav et al as the first two stages of the corrosion mechanism of galvanized steel in chloride solution in wet/dry cycles (Yadav, Nishikata and Tsuru 2004).

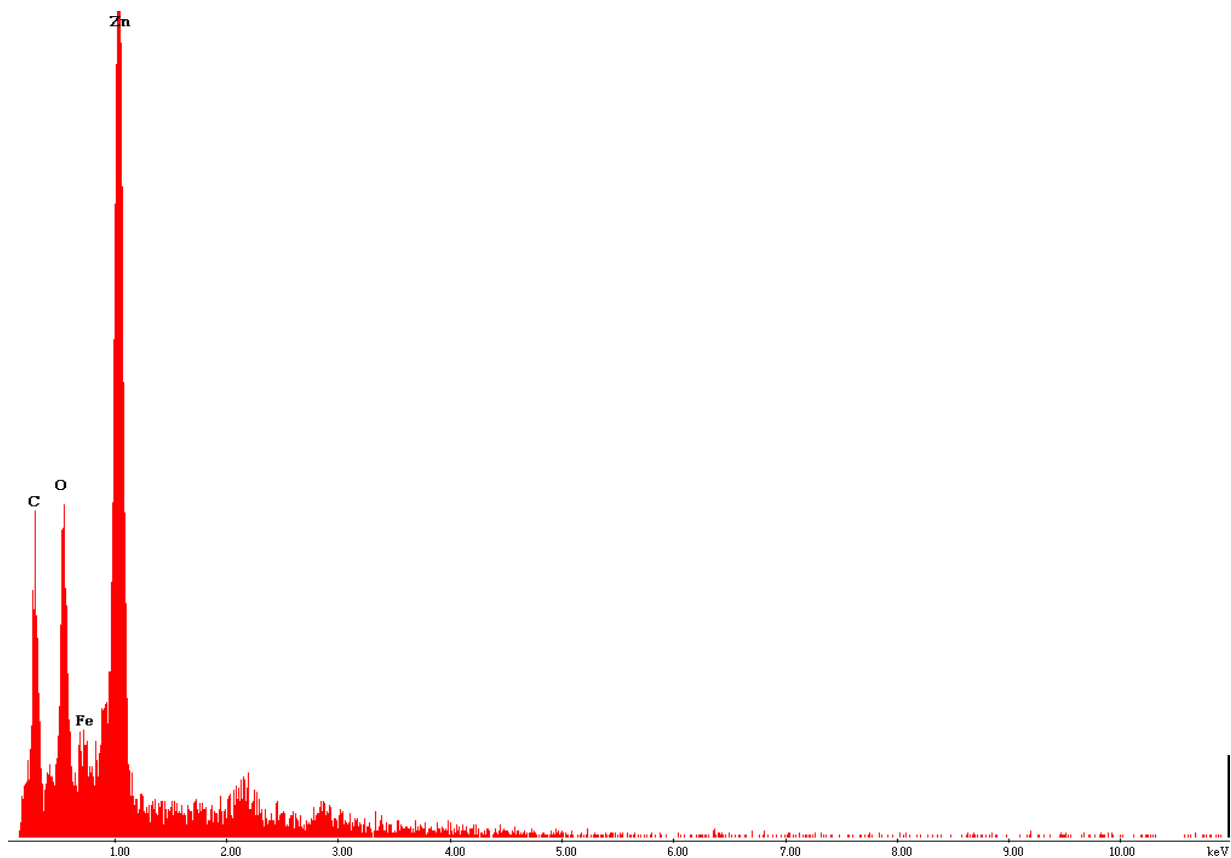


Figure 40.- Area analysis of zinc coating. Analysis performed with EDAX.



Figure 41.- Area analyzed for elements on zinc coating. (SEM image)

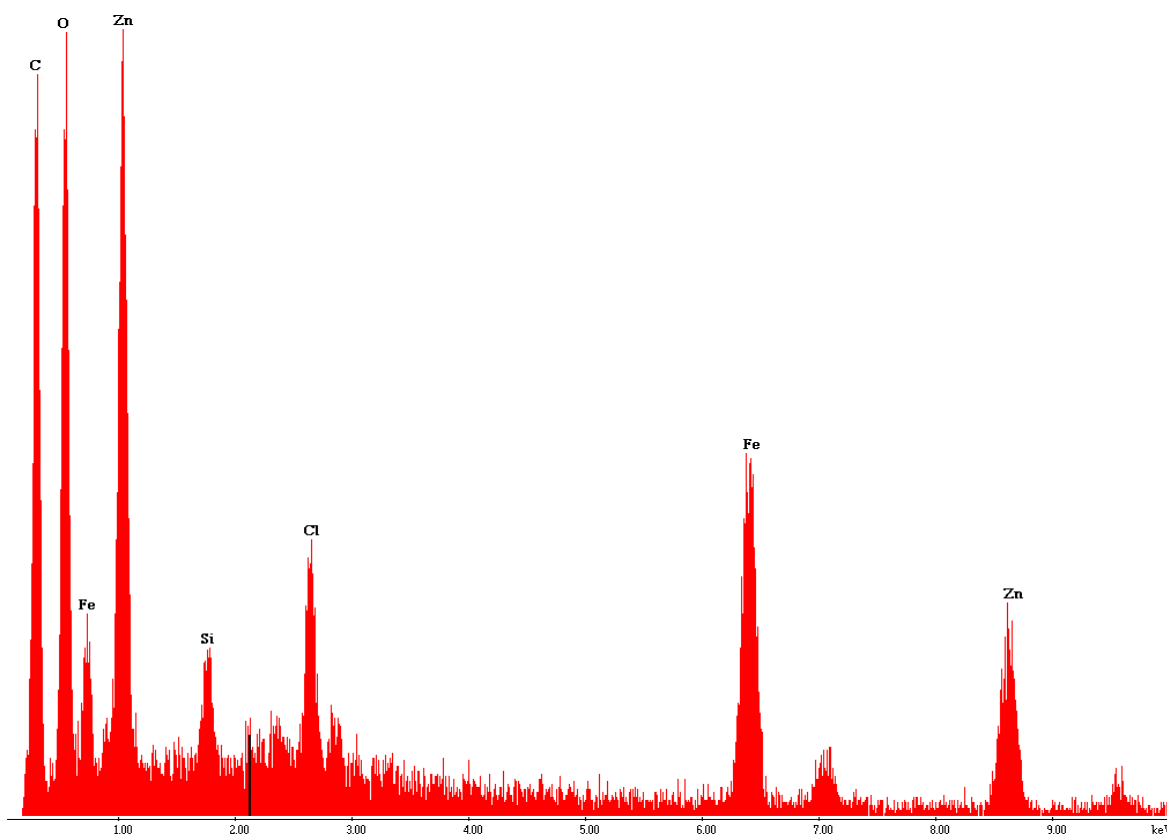


Figure 42.- Area analysis on the microstructure of a galvanized steel corroded on 0.1 M NaCl for 12 hrs. Analysis performed with EDAX.

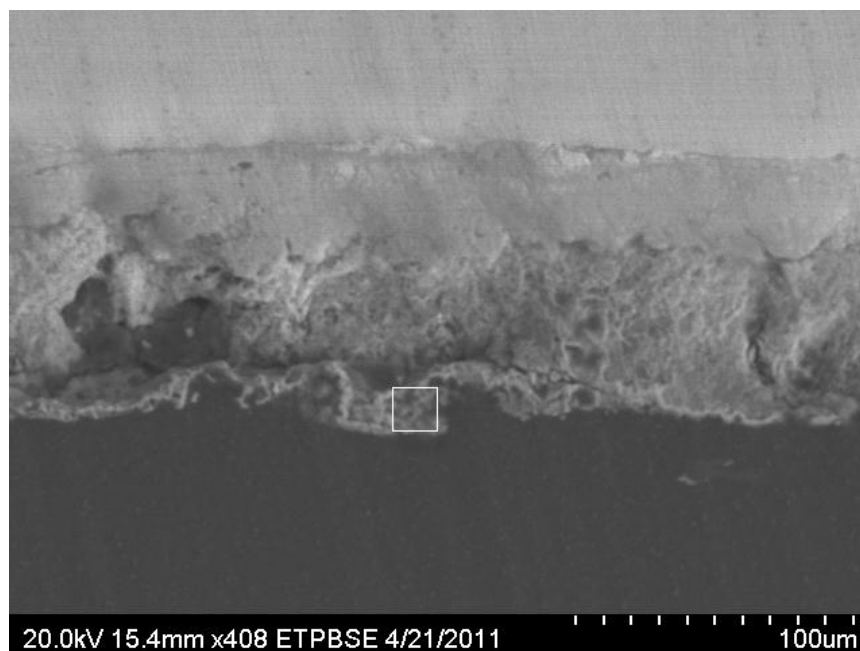


Figure 43.- Area analyzed for elements on the microstructure of corroded galvanized steel on 0.1 M NaCl. (SEM image)

SEM analyses along with area analyses were performed on the extracted electrode from the electrochemical noise experiment performed with soil from Odessa. The electrode underwent wet/dry cycles for 280 days. The microstructure of the zinc coating shows that corrosion products had started to produce in the surface. These corrosion products indicate that the galvanized steel is undergoing a passive corroding state. The elemental area analyses did not show any x-ray peaks of iron, meaning that the underlying steel was not yet reached by the corrosion front. The SEM image illustrates that the thickness of the coating is significantly thicker than the average $\sim 106 \mu\text{m}$ as shown in Figure 44. Figure 44 also shows the area that was analyzed in Figure 45. Figure 45 shows that the element analyzed is mainly composed of zinc and oxygen, these elements suggest that the principal component is ZnO. According to Yadav et al. the galvanized steel is in the first stage of corrosion mechanism in a chloride

environment (Yadav, Nishikata and Tsuru 2004).

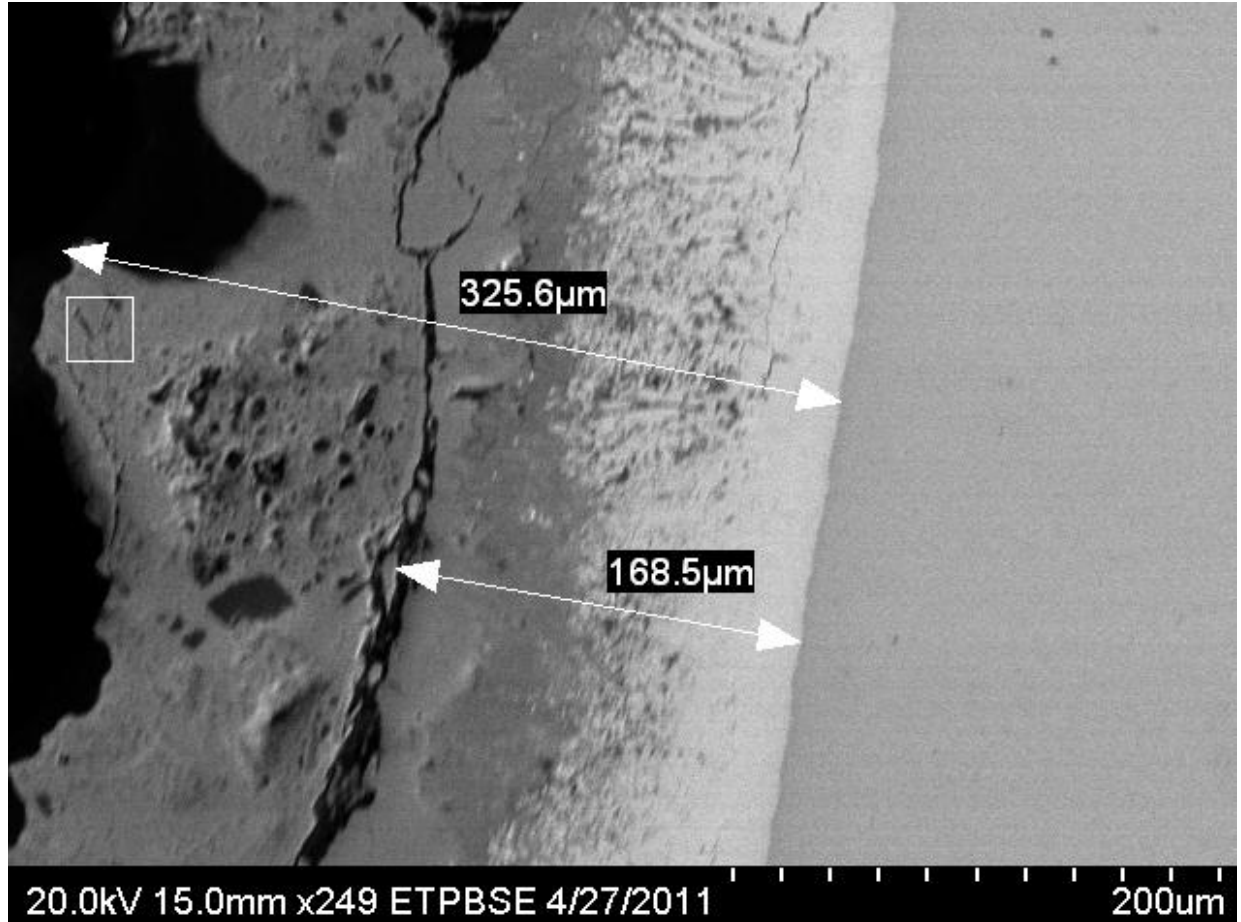


Figure 44.- Microstructure of galvanized steel under real time corrosion for 280 days. Microstructure shows passive corrosion. (SEM image).

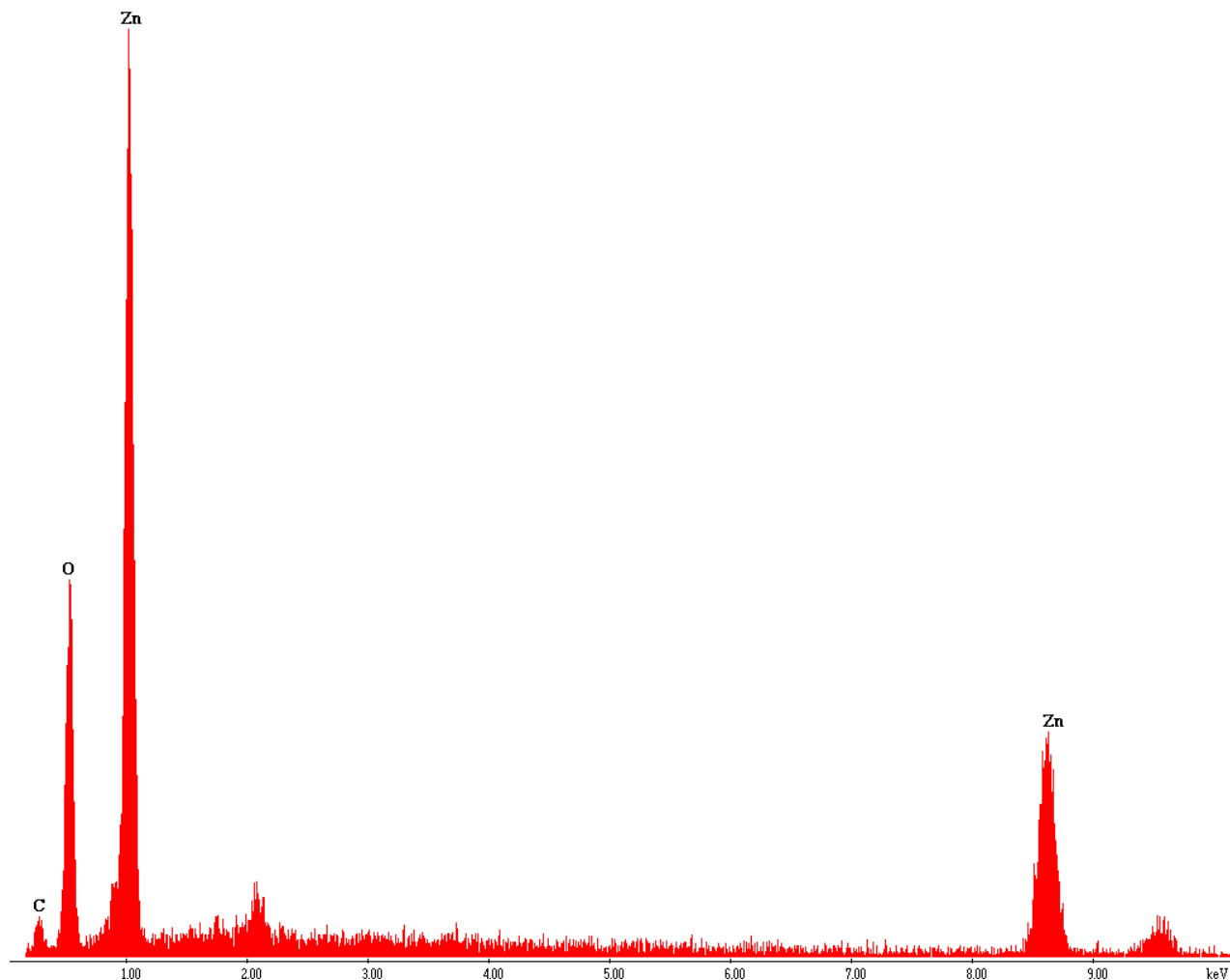


Figure 45.- Area analysis of microstructure of galvanized steel under real time corrosion for 280 days. Acquired with EDAX.

Figure 46 shows an analysis on the concentration of the chlorides in the soil performed by Dr. Borrok and Anita Thapalia. The analysis was performed on the solution drained after the wet cycle in the electrochemical noise experiments. The analysis demonstrates how the chloride concentration diminishes as the cycles continue. After the water is drained in every cycle, the chlorides are drained away from the soil along with the rest of the ions in the soil. As the chlorides (the principal corrosive

ion) and the rest of the ions are extracted from the soil, the corrosion rate is reduced.

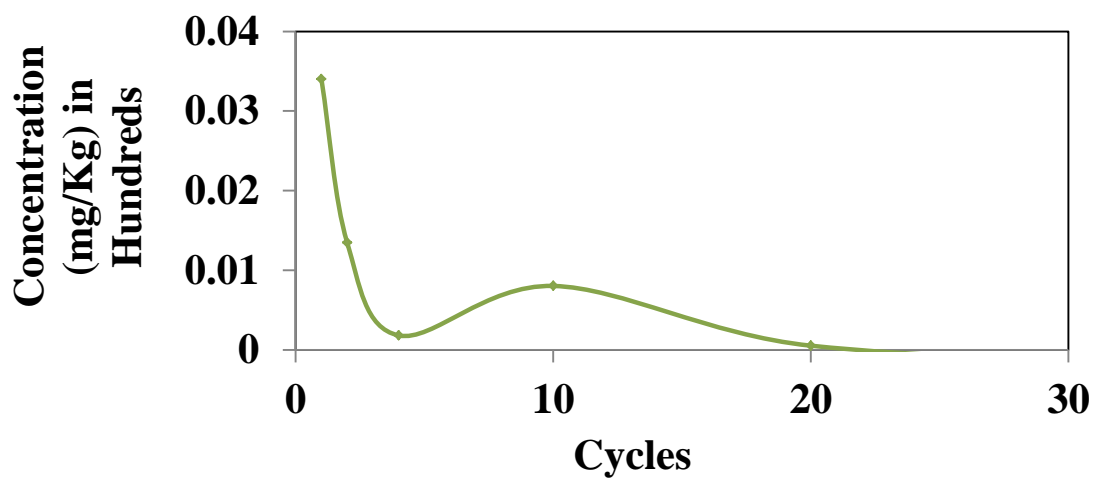


Figure 46.- Chloride concentration analysis on the solution extracted from every wet cycle in the electrochemical noise experiments. Analysis performed by Dr. Borrok and Anita Thapalia.

Chapter 5: Conclusion

The corrosion of galvanized steel exposed to soil has been the focus of the study primarily to determine the long-term behavior based on laboratory tests, as well as developing a sampling technique for monitoring corrosion applicable to field-testing. The monitoring tests consisted of acquiring potential and current transients or electrochemical noise to determine the dissolution of the zinc coating, the intermetallic Fe-Zn layer and the underlying carbon steel. The electrochemical noise was then analyzed by examining the frequencies to link with the corrosion behavior.

In addition, electrochemical impedance spectroscopy (EIS) of the galvanized steel was analyzed to determine the effect of diluted chloride solutions. From the EIS, the corrosion rate was acquired when coupled with the direct current technique, or polarization scan. The corrosion rate for the galvanized steel reached 37.5 mils/yr at the high chloride content (i.e., 0.1 M NaCl) and 0.314 mils/year for the low chloride content (i.e., 0.0001 M NaCl). In comparing the corrosion rates available from field bilogarithmic trends and the acquired laboratory studies, the laboratory corrosion rates of 0.314 and 37.484 $\mu\text{m/yr}$ at 0.0001 and 0.001 M NaCl, respectively, corresponded to the field corrosion rate of 20 $\mu\text{m/yr}$ at 200 ppm Cl (approximating 0.0002 M Cl).

For the electrochemical noise analysis, the power spectrums were acquired for corrosion coupons embedded in soil. The power spectrums for embedded coupons indicated a uniform corrosion. The link between the passive electrochemical noise and EIS seemed related to respective noise resistance and polarization resistance, respectively.

Chapter 6: Future Work

Future work will require a better connectivity between the passive electrochemical noise investigations and electrochemical impedance measurements. The present study initiated a linkage between the potential and current signals taken from galvanized steel embedded in soils, but the linkage must be improved. One of the main problems presented in the process of taking measurements of electrochemical noise is that crevice corrosion was being presented. To prevent future crevice corrosion the electrodes edges must be sealed prior and after the assembly of the coupon. The sealing must be done without covering any surface of the electrode since this would lead to erroneous measurements.

References

1. Aal, E.E. Abd El, and S. Abd El Wanees. "Galvanostatic study of the breakdown of Zn passivity by sulphate anions." *Corrosion Science*, 2009: 1780-1788.
2. Annergren, I., F. Zou, and D. Thierry. "Application of localized electrochemical techniques to study kinetics of initiation and propagation during pit growth." *Electrochimica Acta*, 1999: 4383-4393.
3. Asami, K., and M. Kikuchi. "In-depth distribution of rusts on a plain carbon steel and weathering steels exposed to coastal-industrial atmosphere for 17 years." *Corrosion Science*, 2003: 2671-2688.
4. Bertocci, U., J. Frydman, C. Gabrielli, F. Huet, and M. Keddam. "Analysis of Electrochemical Noise by Power Spectral Density Applied to Corrosion Studies." *Journal of Electrochemical Society* , 1998: 2780-2786.
5. Bierwagen, G. P., V. Balbyshev, D. Mills, and D. Tallman. "'Fundamental condideration on electrochemical noise methods to examin corrosion under organic coatings." *Electrochemical Society*, 1994.
6. Cottis, R. A. "Interpretation of Electrochemical Noise Data." *Corrosion*, 2001: 265-285.
7. Cottis, R. A., and S. Turgoose. "Electrochemical noise measurements - a theoretical basis." *Materials Science Forum*, 1995: 663-672.
8. El-Mahdy, Gamal Ahmed, Atsushi Nishikata, and Tooru Tsuru. "Electrochemical corrosion monitoring of galvanized steel under cyclic wet-dry conditions." *Corrosion Science*, 2000: 183-194.
9. Fontana, Mars Guy. *Corrosion Engineering*. New York: McGraw-Hill, 1986.

10. Gabrielli, C., F. Huet, and R. Oltra. "A review of the probabilistic aspects of localized corrosion." *Corrosion*, 1990: 266-278.
11. Gouda, V. K., M. G. A. Khedr, and A. M. Shams El Din. "Role of anions in the corrosion and corrosion-inhibition of zinc in aqueous solutions." *Corrosion Science*, 1967: 221-230.
12. Guan, X., and D. D. Macdonald. "Determination of corrosion mechanisms and estimation of electrochemical kinetics of metal corrosion in high subcritical and supercritical aqueous systems." *Corrosion*, 2009: 376-387.
13. Horstmann, D. "Reaction between zinc and iron." *Zinc development association*, 1978.
14. Ishikawa, Tatsuo, Minoru Kumagai, Akemi Yasukawa, Kazuhiko Kandori, Takenori Nakayama, and Fumio Yuse. "Influences of metal ions on the formation of γ -FeOOH and magnetite rust." *Corrosion Science*, 2002: 1073-1086.
15. Ishikawa, Tatsuo, Sho Miyamoto, Kazuhiko Kandori, and Takenori Nakayama. "Influence of anions on the formation of β -FeOOH rusts ." *Corrosion Science*, 2005: 2510-2520.
16. Jones, Denny A. *Principles and Prevention of Corrosion*. New York: Macmillan Publishing Company, 1992.
17. Kaesche, Helmut. "Electrode Impedance Spectroscopy." In *Corrosion of Metals; Physicochemical Principles and Current Problems*, by Helmut Kaesche, 562-580. Berlin: Springer, 2003.
18. Kamimura, T., et al. "Influence of cations and anions on the formation of β -FeOOH." *Corrosion Science*, 2005: 2531-2542.

19. Kubachewski, O., and T. Massalski. "Binary alloy phase diagrams." *ASM*, 1986: 1128.
20. Laycock, N. J., and R. C. Newman. "Localised Dissolution Kinetics, Salt Films and Pitting Potentials." *Corrosion Science*, 1997: 1771-1790.
21. Macdonald, Digby D., Chun Liu, and Michael P. Manahan. "Electrochemical noise measurement on carbon and stainless steels in high subcritical and supercritical aqueous environments." *American Society for Testing and Materials*, 1996: 247-265.
22. Mansfeld. "Recording and Analysis of AC Impedance Data for Corrosion Studies." *Corrosion*, 1981: 301-307.
23. Mansfeld, F., and C. C. Lee. "The frequency dependence of the noise resistance for polymer-coated metals." *Journal of Electrochemical Society*, 1997: 2068-2071.
24. Mansfeld, F., and H. Xiao. "Electrochemical noise analysis of iron exposed to NaCl solutions of different corrosivity." *Journal of electrochemical society*, 1994: 1402-1404.
25. Mansfeld, F., S. Lin, Y. C. Chen, and H. Shih. "Minimization of high-frequency phase shift in impedance measurements." *Journal of Electrochemical Society*, 1988: 906-908.
26. Mansfeld, F., Z. Sun, and C. H. Hsu. "Electrochemical noise analysis (ENA) for active and passive systems in chloride media." *Electrochimica Acta*, 2000: 3651-3664.
27. Mansfeld, Florian. "Electrochemical Impedance Spectroscopy (EIS) as a new tool

- for investigating methods of corrosion protection." *Electrochimica Acta*, 1990: 1533-1544.
28. Marder, A. R. "The metallurgy of zinc coated steel." *Progress in materials science*, 2000: 191-271.
29. Nishikata, A., Y. Ichihara, and T. Tsuru. "An application of electrochemical impedance spectroscopy to atmospheric corrosion study." *Corrosion Science*, 1995: 897-911.
30. Refait, P., and J.-M.R. Genin. "The mechanisms of oxidation of ferrous hydroxychloride β -Fe₂(OH)₃Cl in aqueous solution: the formation of akaganeite Vs goethite." *Corrosion Science*, 1997: 539-553.
31. Tanaka, Hidekazu, Junko Wakatsuki, Kazuhiko Kandori, Tatsuo Ishikawa, and Takenori Nakayama. "Role of zinc on the formation, morphology, and adsorption characteristics of β -FeOOH rusts." *Corrosion Science*, 2010: 2973-2978.
32. Vera Cruz, R. P., A. Nishikata, and T. Tsuru. "AC Impedance monitoring of pitting corrosion of stainless steel under a wet-dry cyclic condition in chloride-containing environment." *Corrosion Science*, 1996: 1397-1406.
33. Walter, G. W. "Corrosion rates of zinc, zinc coatings and steel in aerated slightly acidic chloride solutions calculated from low polarization data." *Corrosion Science*, 1976: 573-586.
34. Walter, G. W. "Critical Analysis of Some Electrochemical Techniques Including Polarization Resistance, for the Study of Zinc Coating Performance in Near Neutral Chloride Solutions." *Corrosion Science*, 1975: 47-56.
35. Yadav, A. P., A. Nishikata, and T. Tsuru. "Electrochemical impedance study on

galvanized steel corrosion under cyclic wet-dry conditions-- influence of time of wetness." *Corrosion Science*, 2004: 169-181.

36. Yadav, A.P., H. Katayama, K. Noda, H. Masuda, A. Nishikita, and T. Tsuru.

"Surface potential distribution over zinc/steel galvanic couple corroding under thin layer of electrolyte." *Electrochimica Acta* 52, 2007: 3121-3129.

37. Yadav, Amar Prasad, Atsushi Nishikata, and Tooru Tsuru. "Degradation

mechanism of galvanized steel in wet-dry cyclic environment containing chloride ions." *Corrosion Science* 46, 2004: 361-376.

38. Yadav, Amar Prasad, Atsushi Nishikata, and Tooru Tsuru. "Oxygen reduction

mechanism on corroded zinc." *Journal of Electroanalytical Chemistry*, 2005: 142-149.

39. Yamashita, M., H. Konishi, T. Kozakura, J. Mizuki, and H. Uchida. "In situ

observation of initial rust formation process on carbon steel under Na₂SO₄ and NaCl solution films with wet/dry cycles using synchrotron radiation X-rays." *Corrosion Science*, 2005: 2492-2498.

40. Zhang, X. G., and E. M. Valeriete. "Galvanic protection of steel and galvanic

corrosion of zinc under thin layer electrolytes." *Corrosion Science*, 1993: 1957-1972.

Appendix

Polarization curves

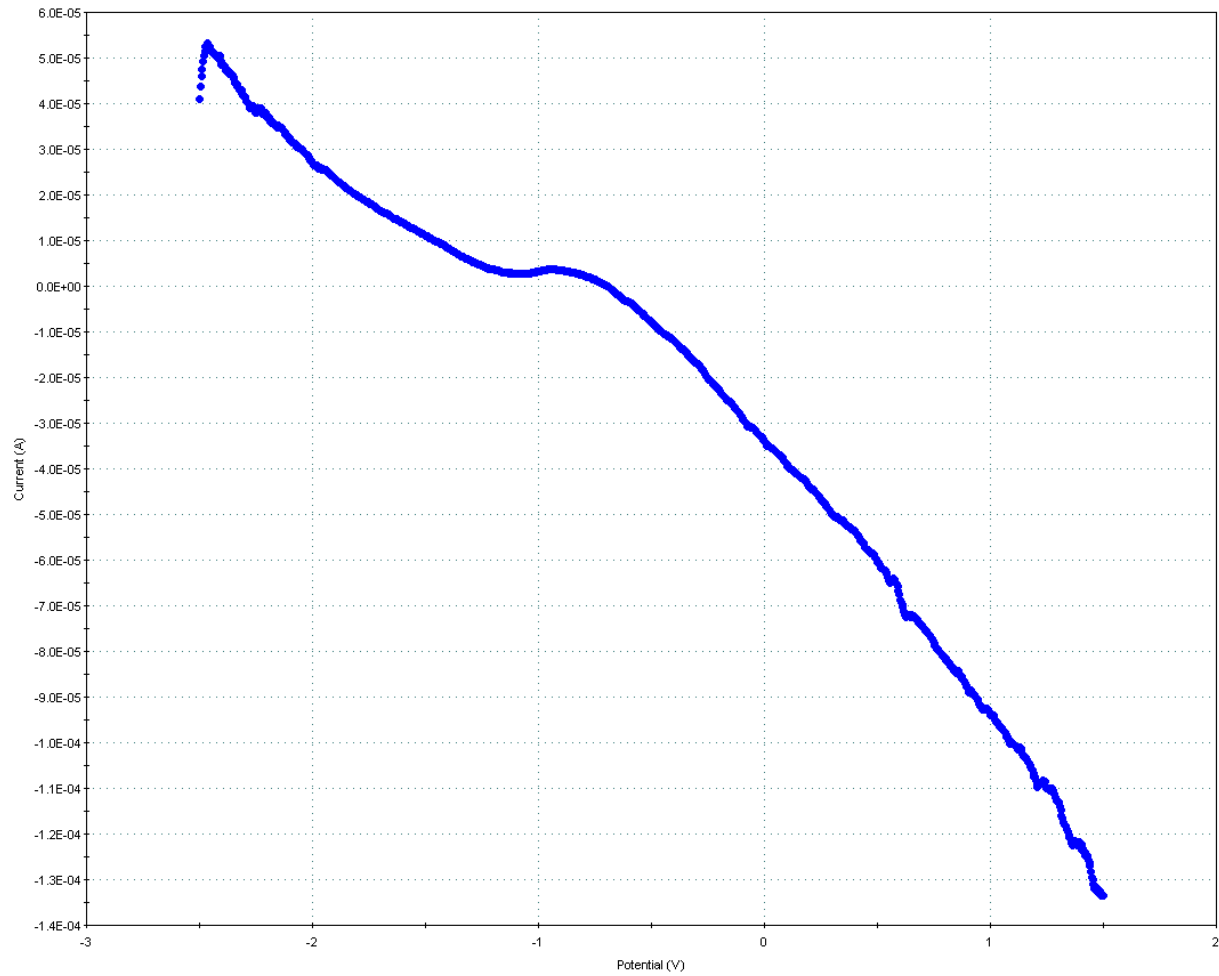


Figure 47.- Polarization curve for galvanized steel in 0.0001 M NaCl solution.

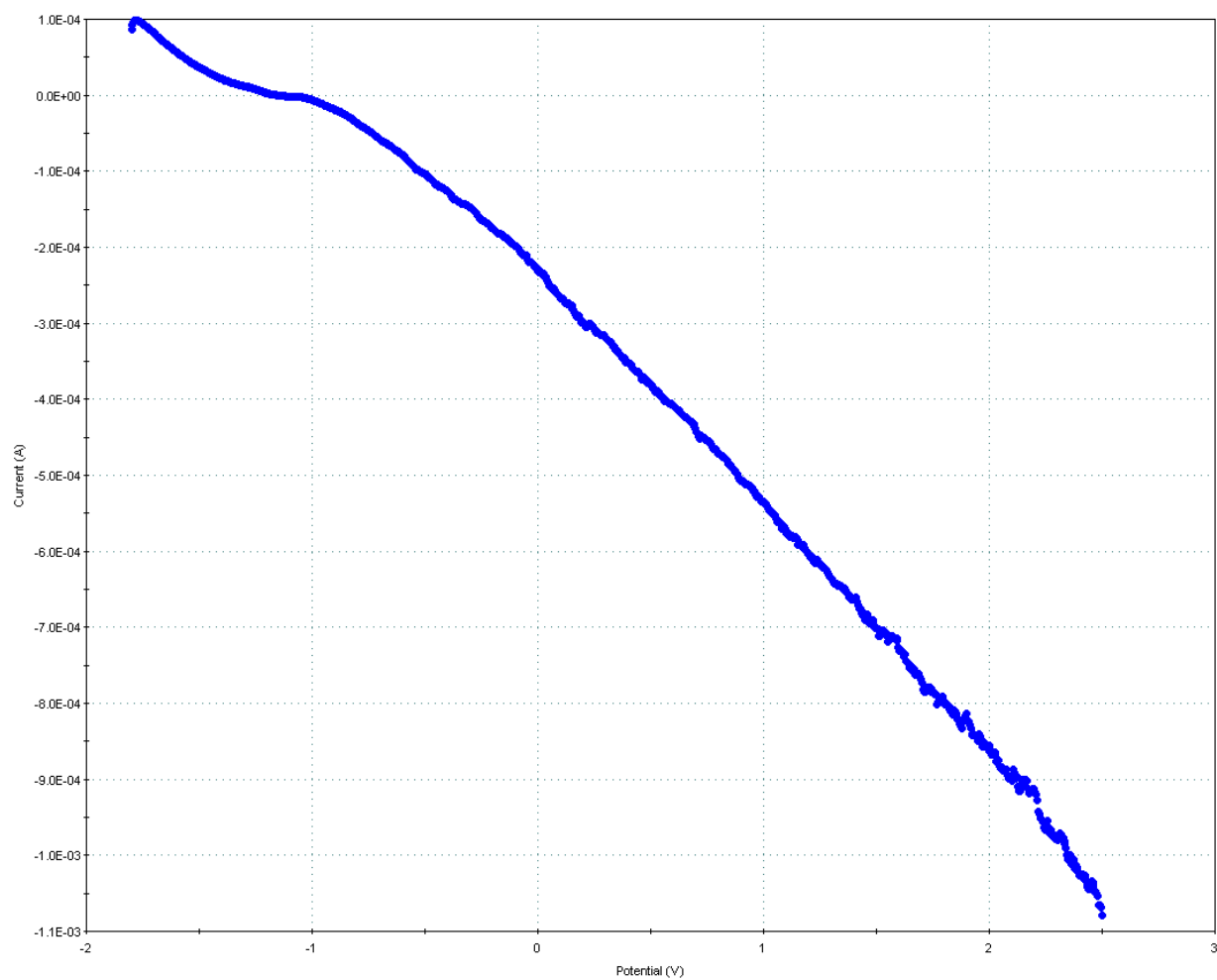


Figure 48.- Polarization curve for galvanized in 0.001 M NaCl solution.

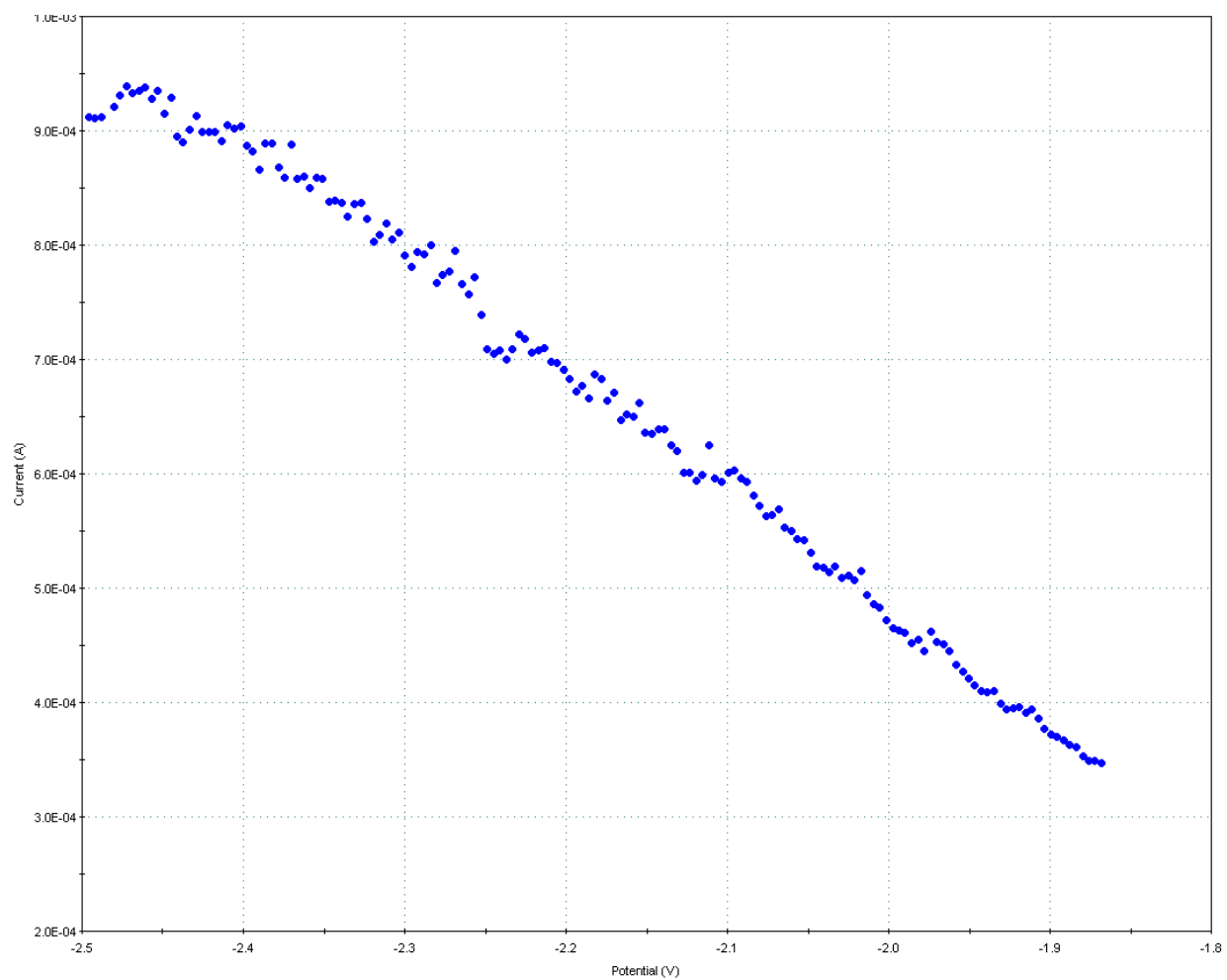


Figure 49.- Polarization curve for galvanized in 0.01 M NaCl solution.

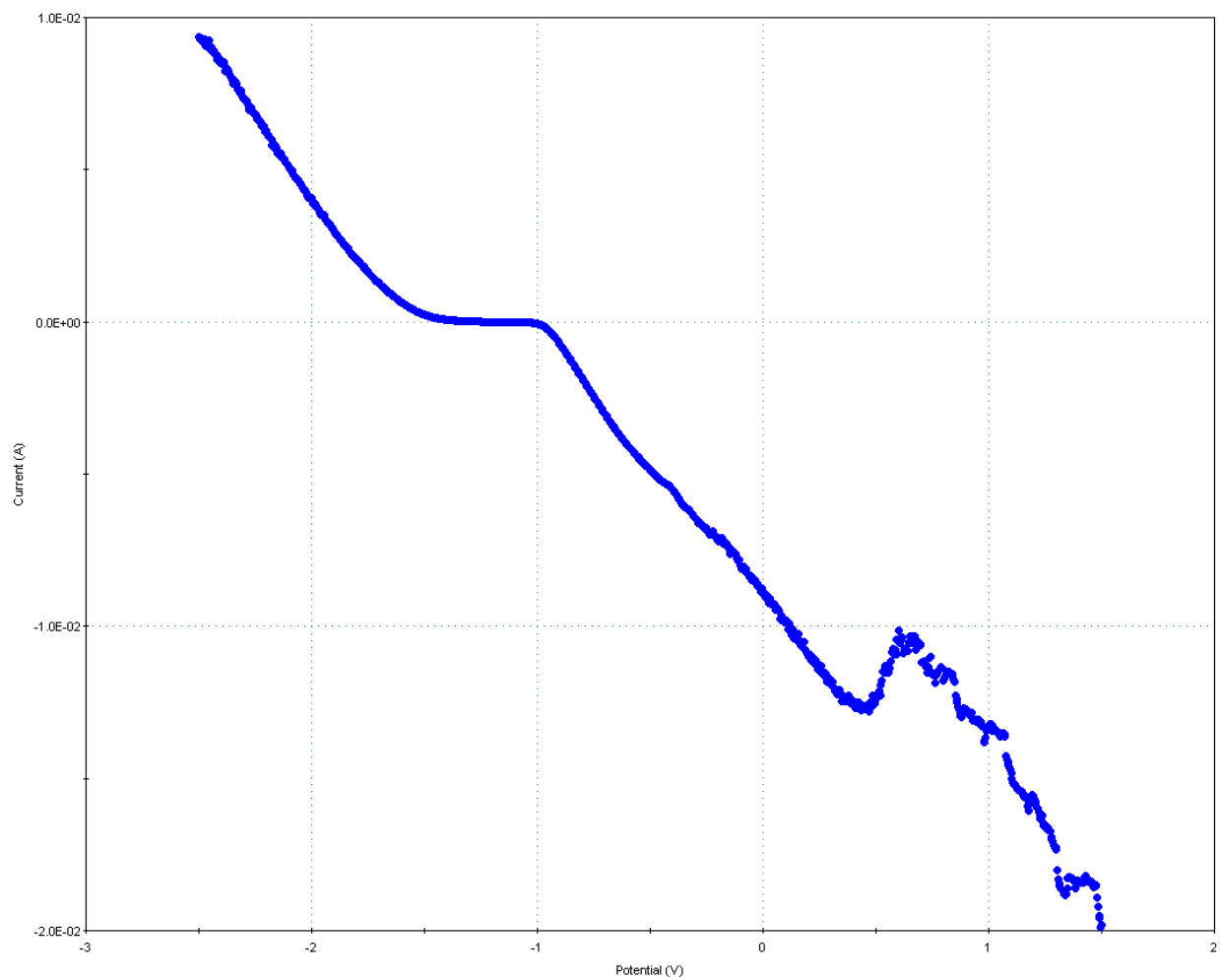


Figure 50.- Polarization curve for galvanized in 0.1 M NaCl solution.

Electrochemical impedance spectroscopy graphs

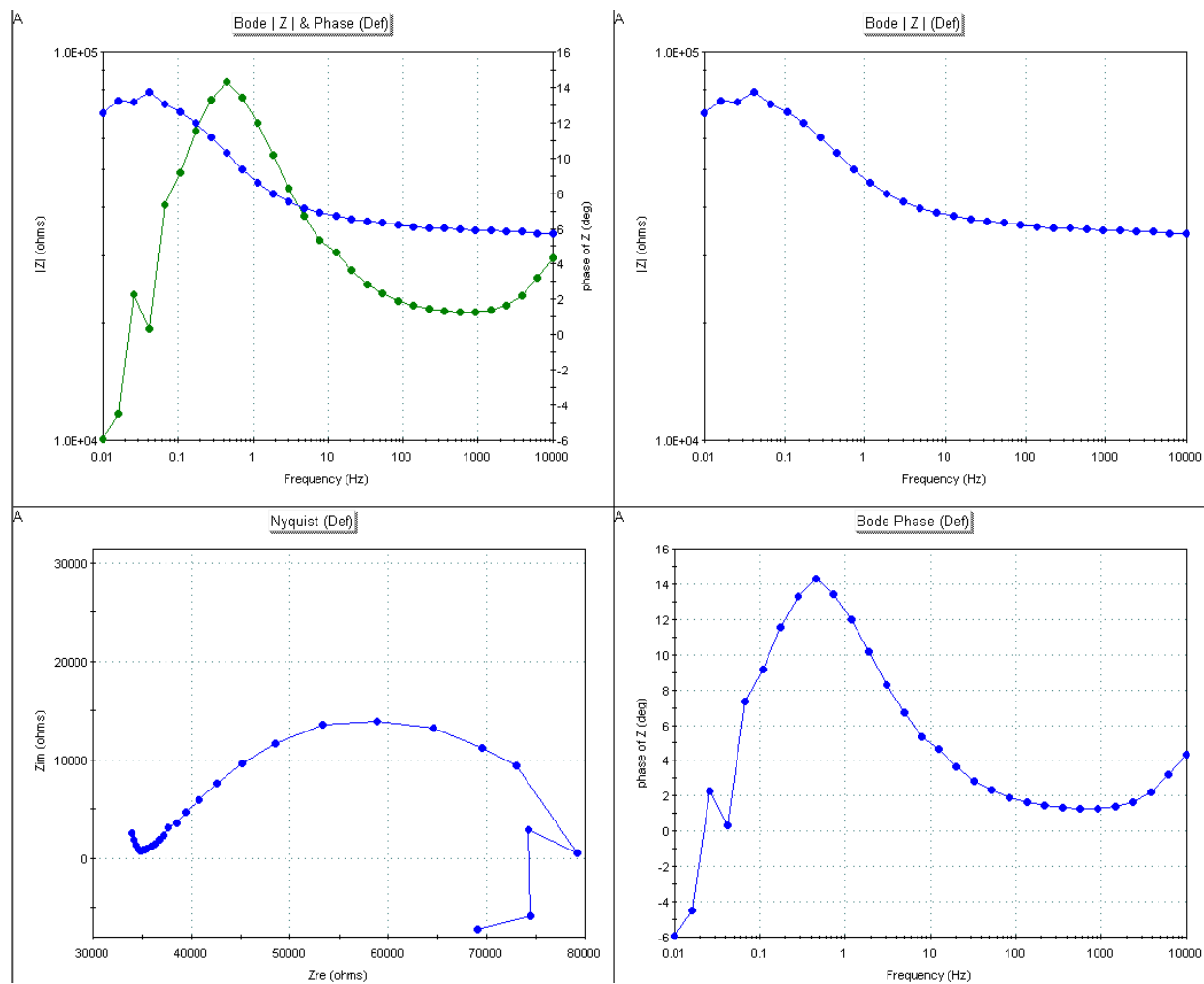


Figure 51.- Bode and Nyquist plots for galvanized steel at 0.0001 M NaCl solution.

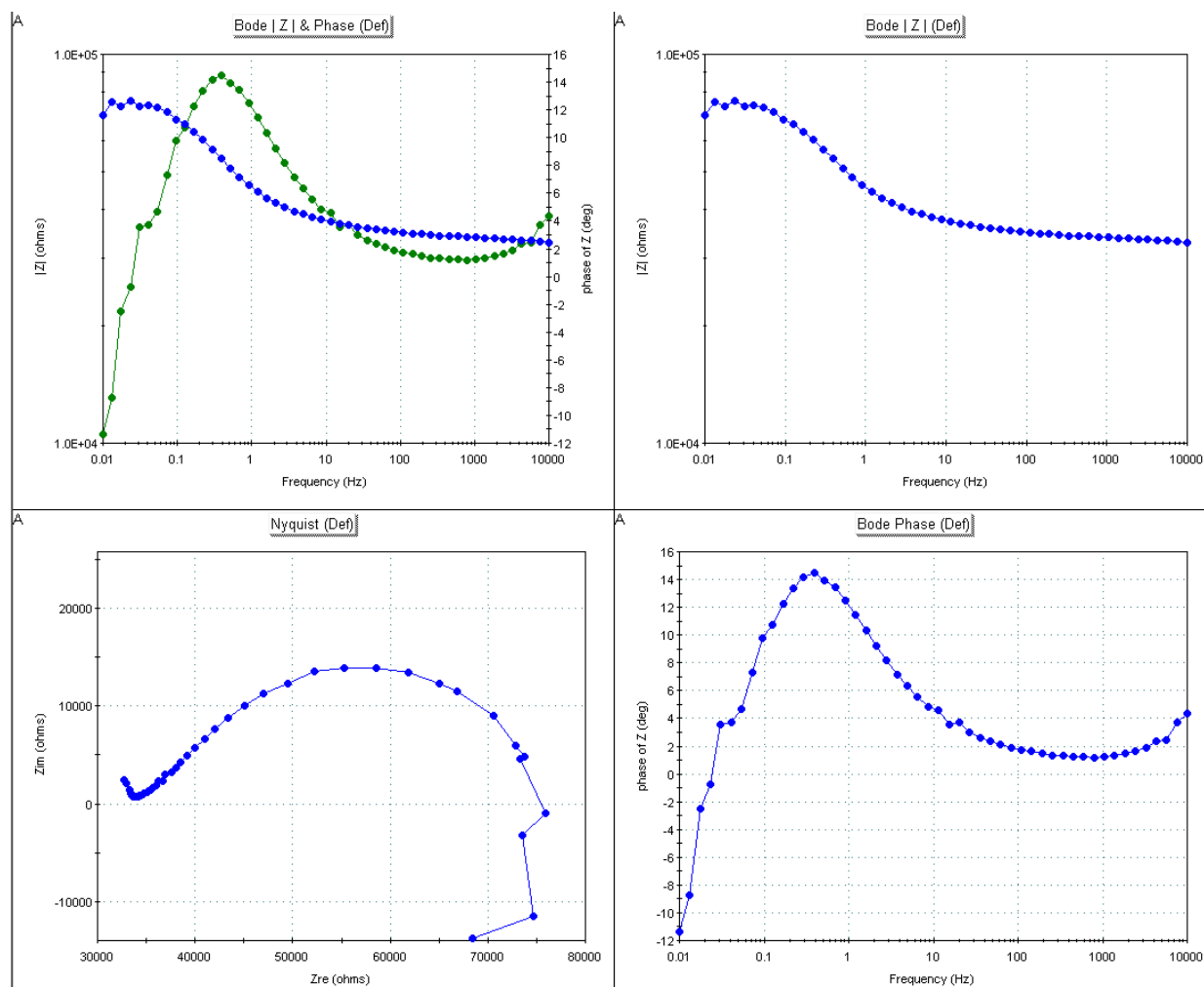


Figure 52.- Bode and Nyquist plots for galvanized steel at 0.0001 M NaCl solution.

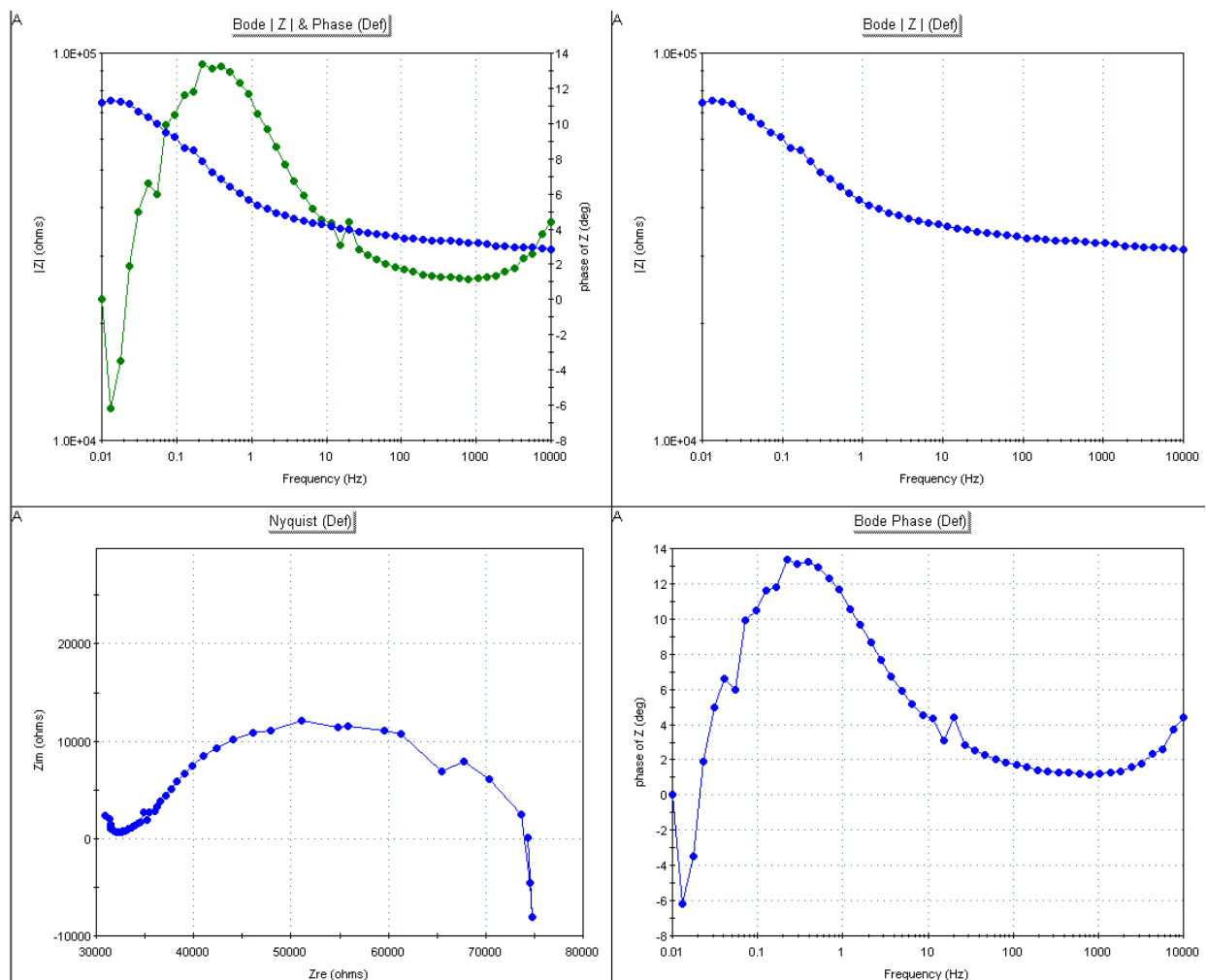


Figure 53.- Bode and Nyquist plots for galvanized steel at 0.0001 M NaCl solution.

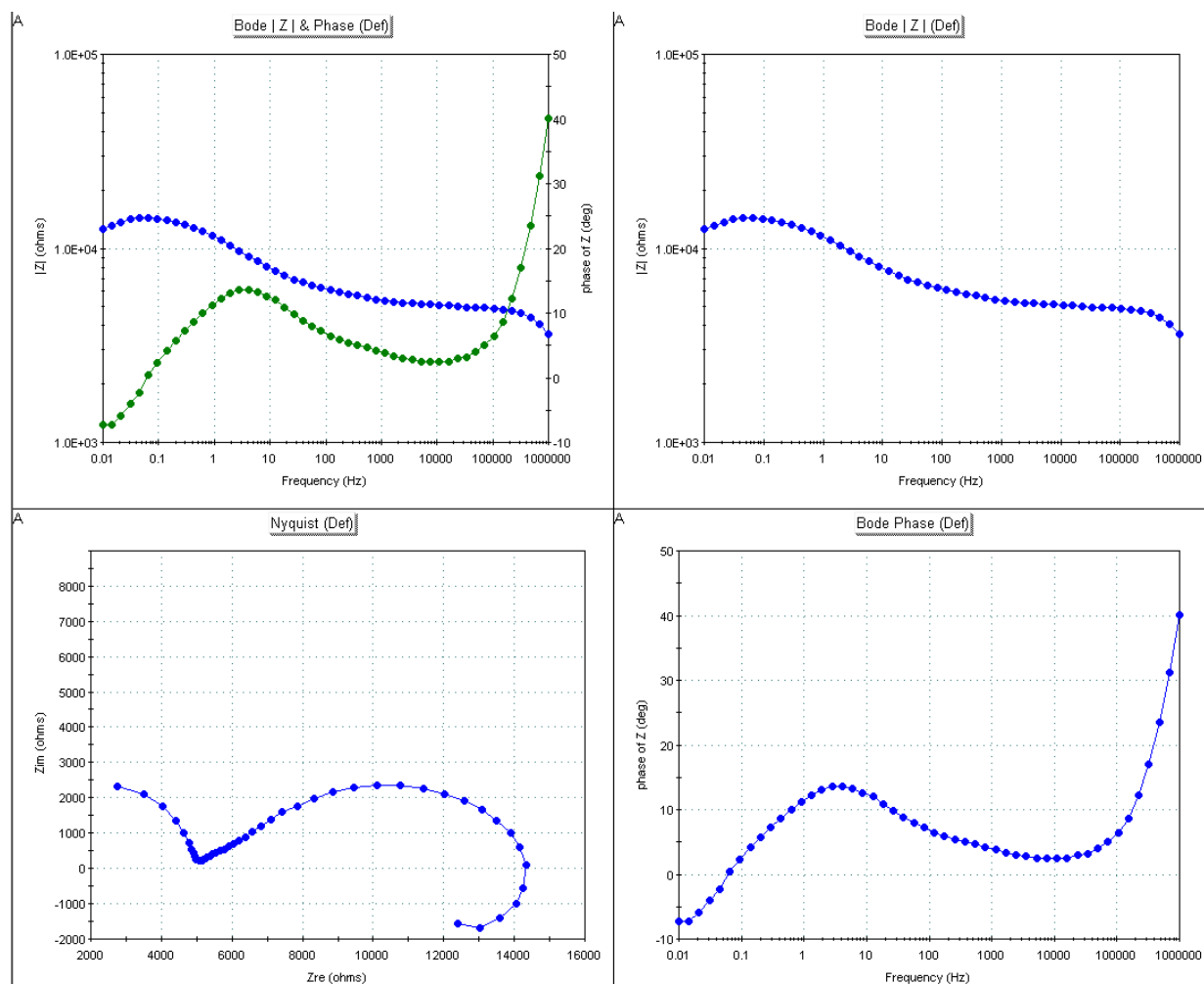


Figure 54.- Bode and Nyquist plots for galvanized steel at 0.001 M NaCl solution.

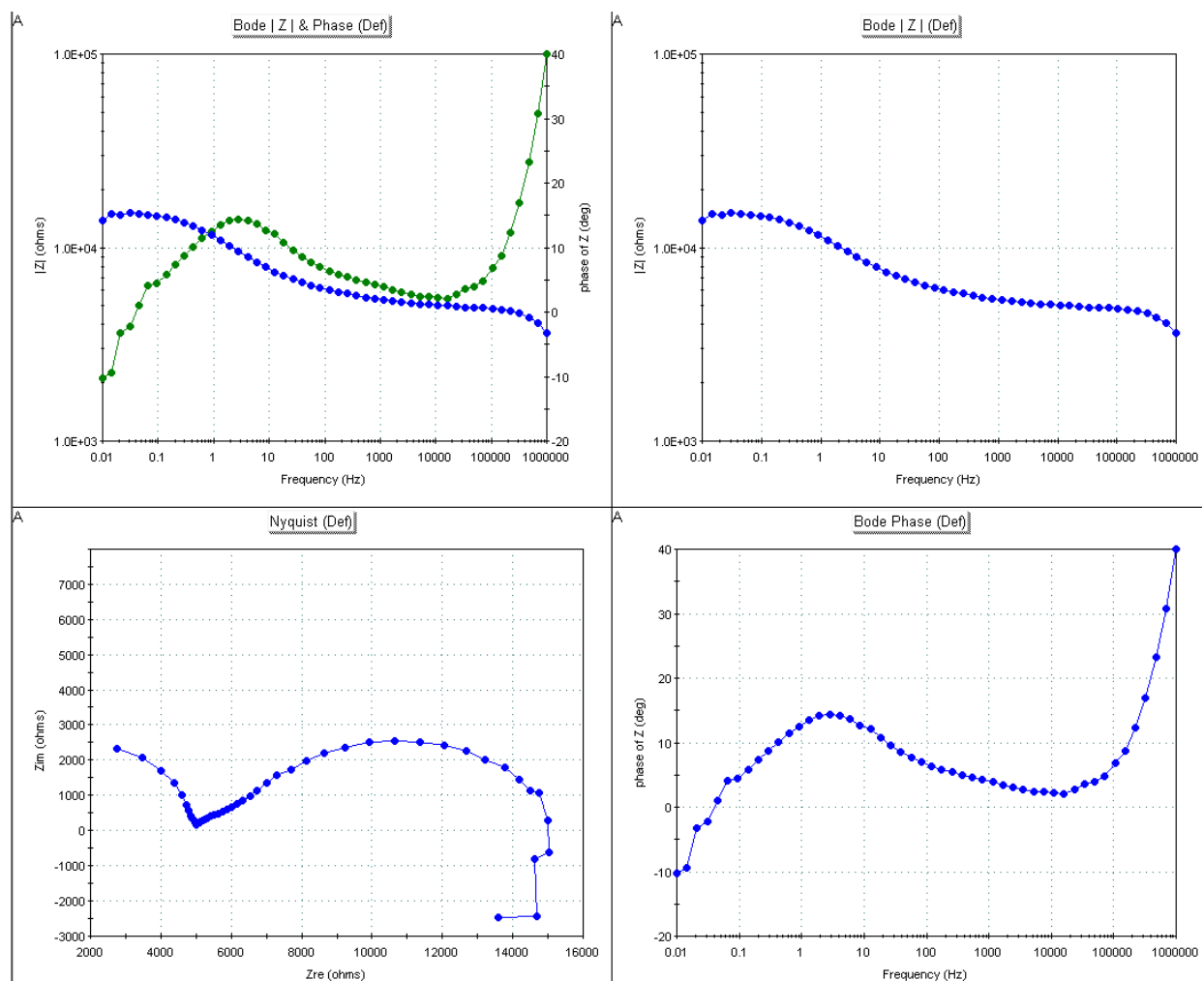


Figure 55.- Bode and Nyquist plots for galvanized steel at 0.001 M NaCl solution.

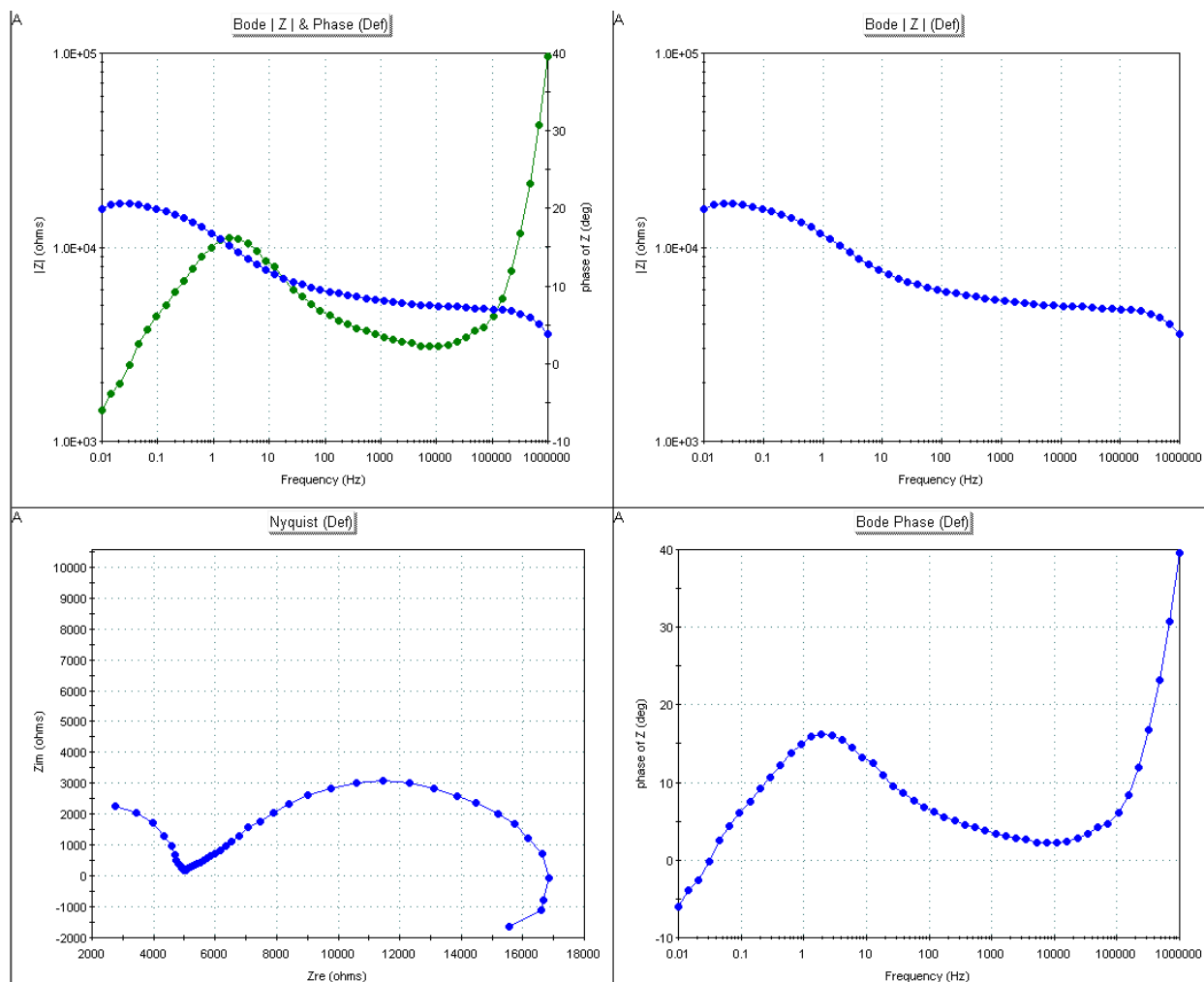


Figure 56.- Bode and Nyquist plots for galvanized steel at 0.001 M NaCl solution.

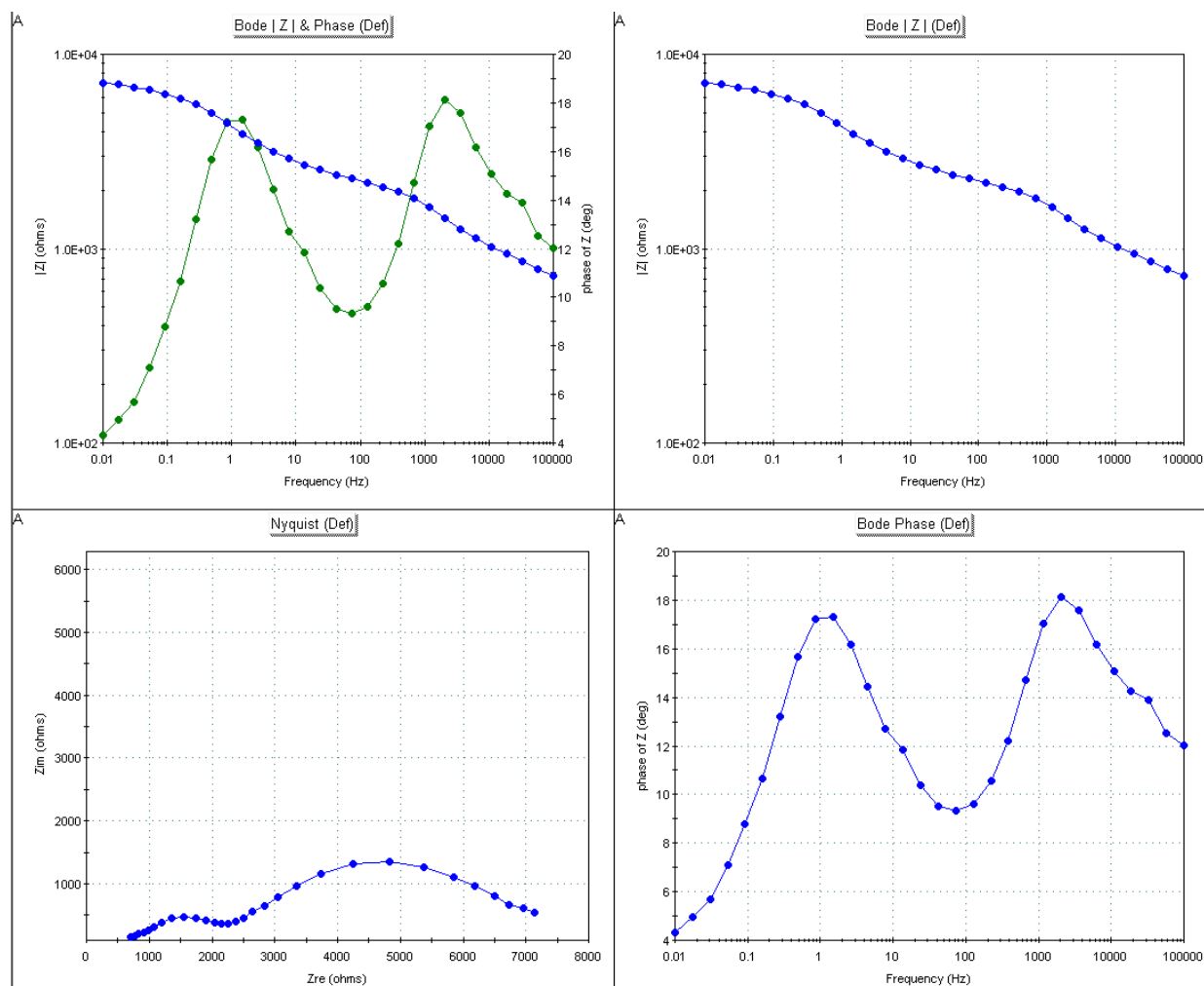


Figure 57.- Bode and Nyquist plots for galvanized steel at 0.01 M NaCl solution.

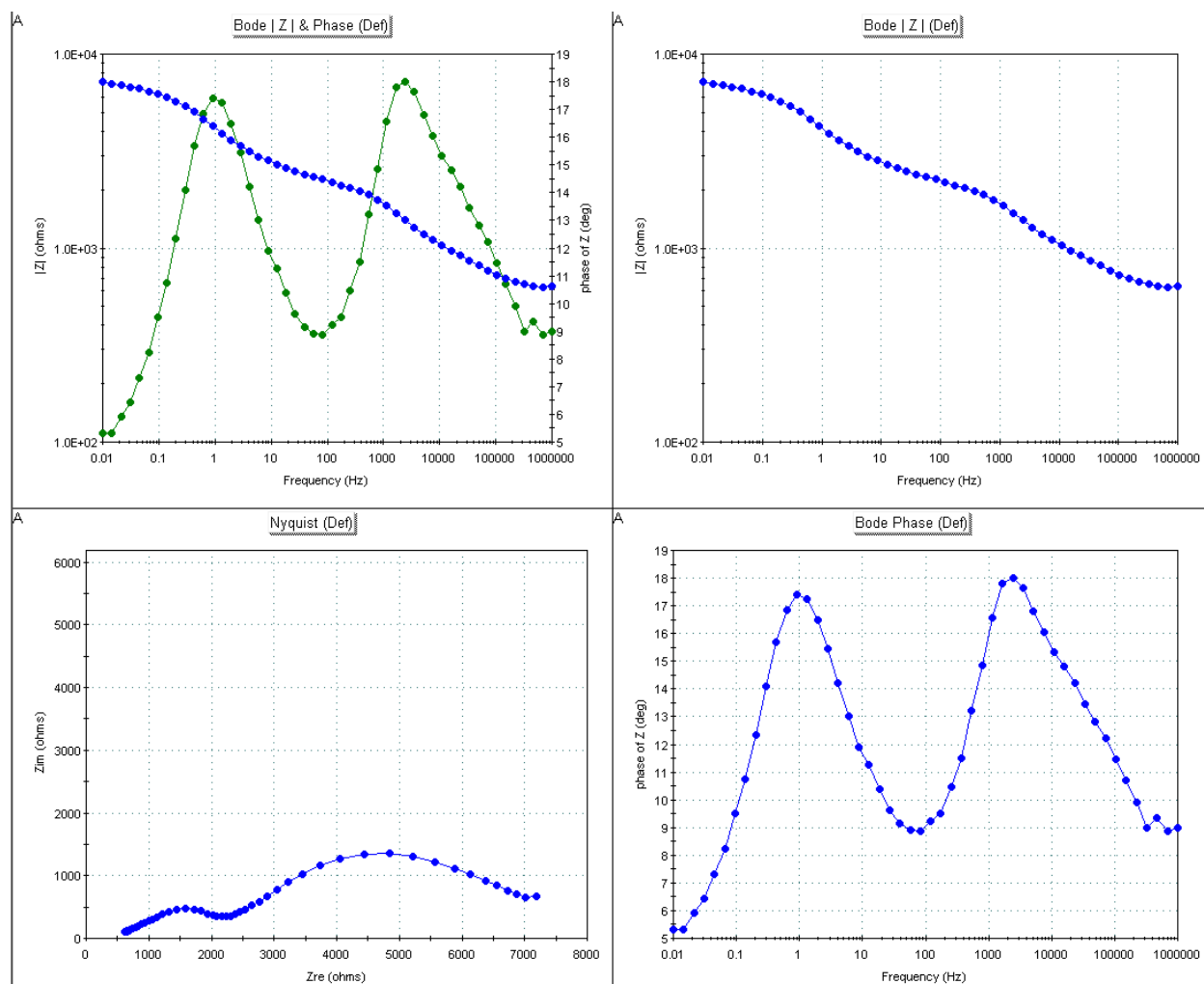


Figure 58.- Bode and Nyquist plots for galvanized steel at 0.01 M NaCl solution.

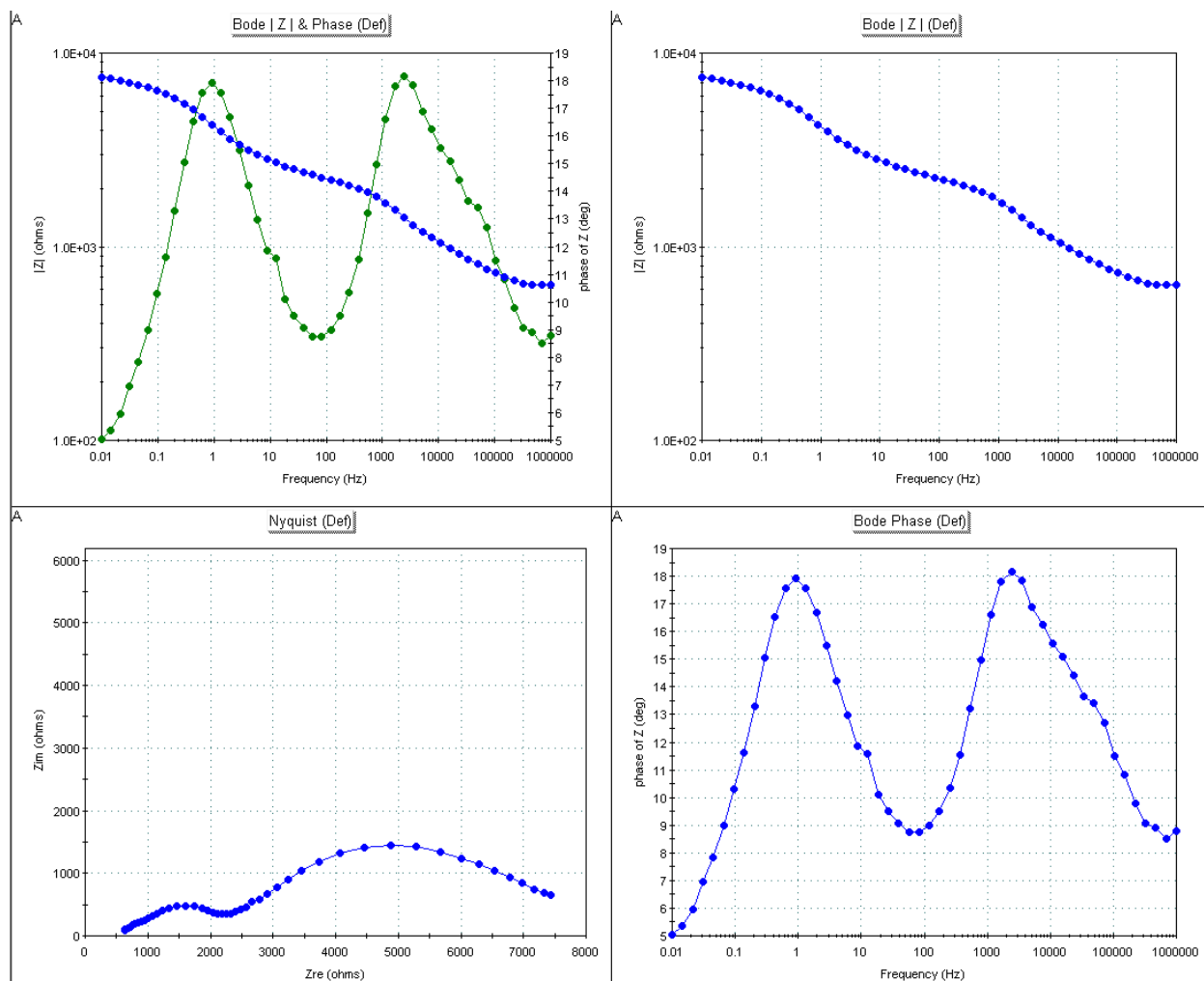


Figure 59.- Bode and Nyquist plots for galvanized steel at 0.01 M NaCl solution.

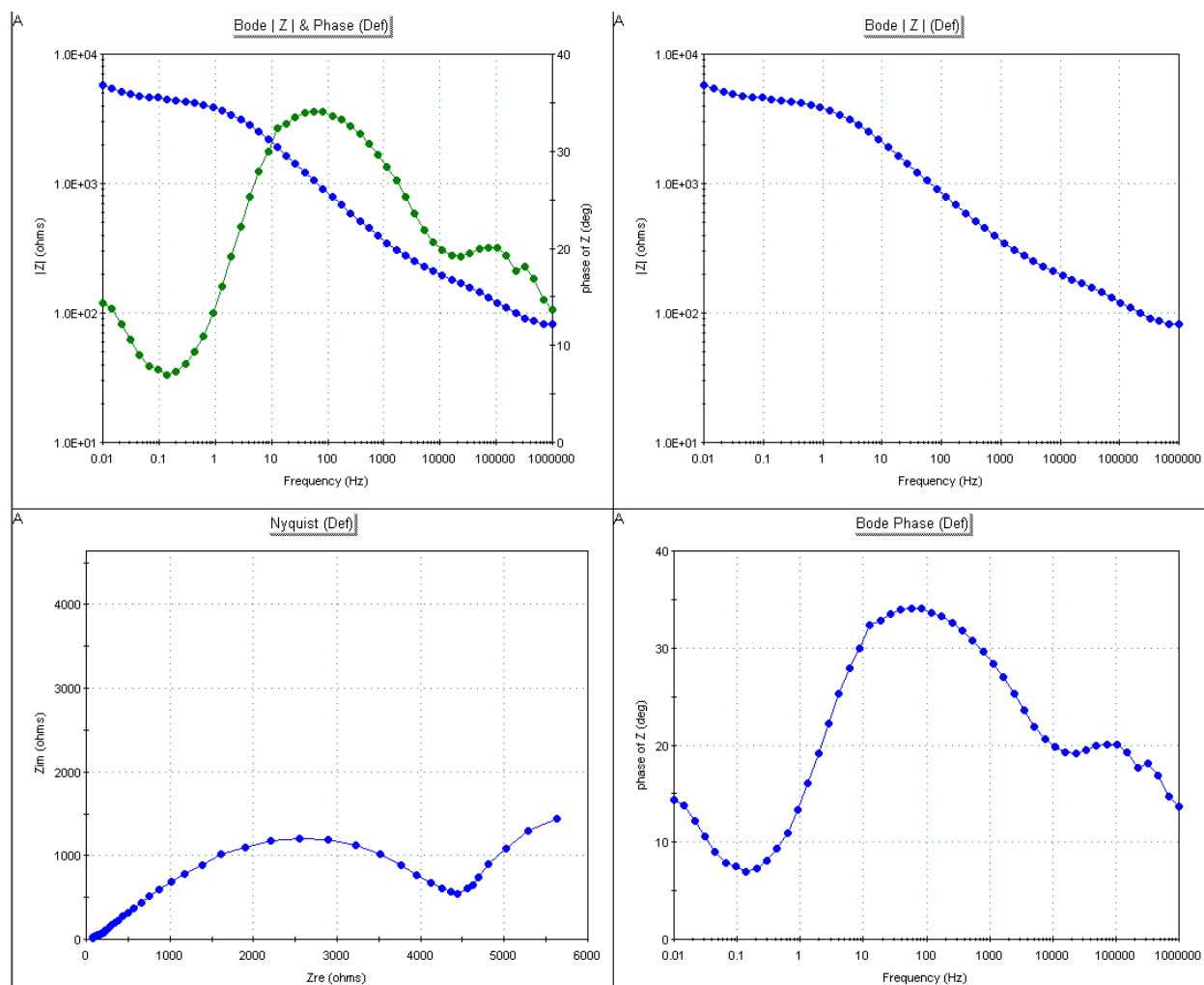


Figure 60.- Bode and Nyquist plots for galvanized steel at 0.1 M NaCl solution.

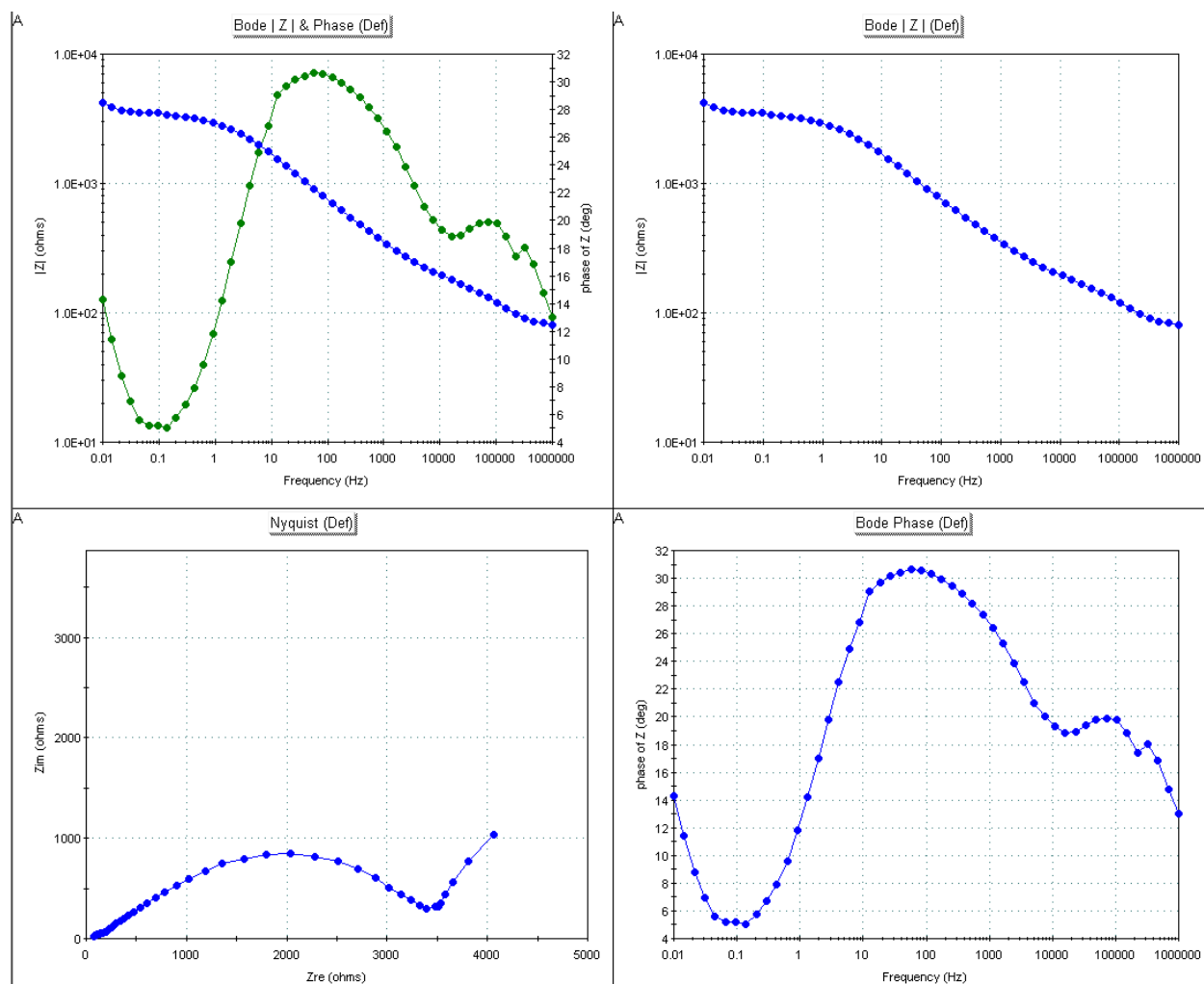


Figure 61.- Bode and Nyquist plots for galvanized steel at 0.1 M NaCl solution.

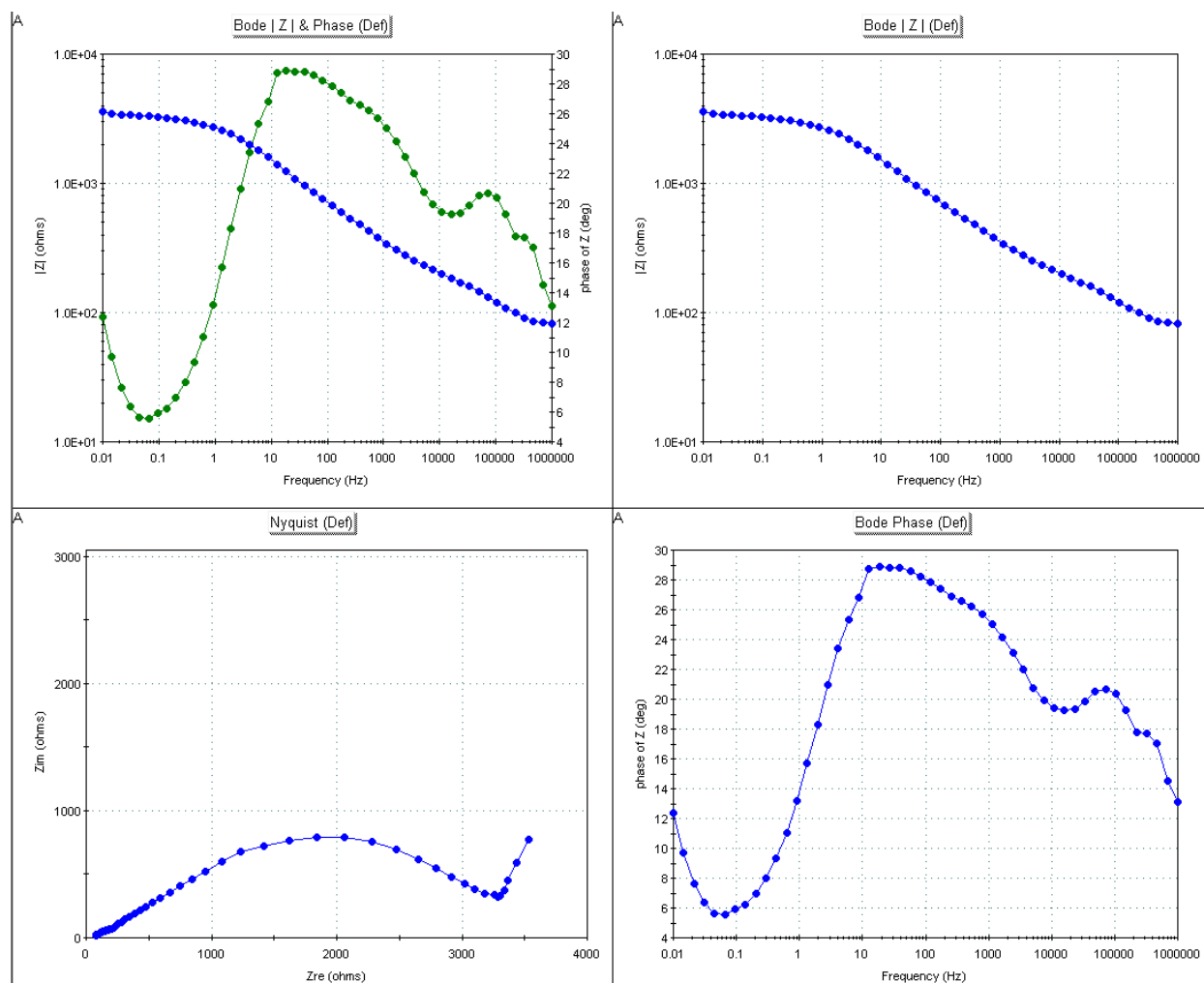


Figure 62.- Bode and Nyquist plots for galvanized steel at 0.1 M NaCl solution.

Electrochemical noise graphs

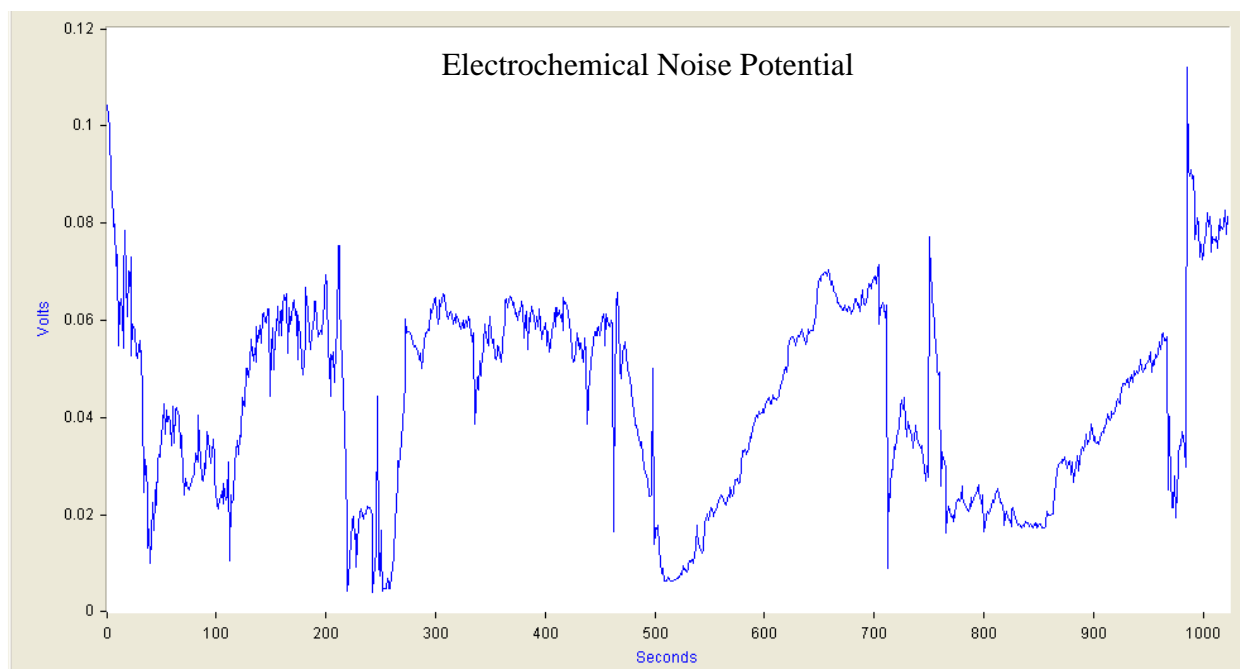


Figure 63.- Electrochemical noise potential for Odessa (sample 2). Acquired with Dadisp.

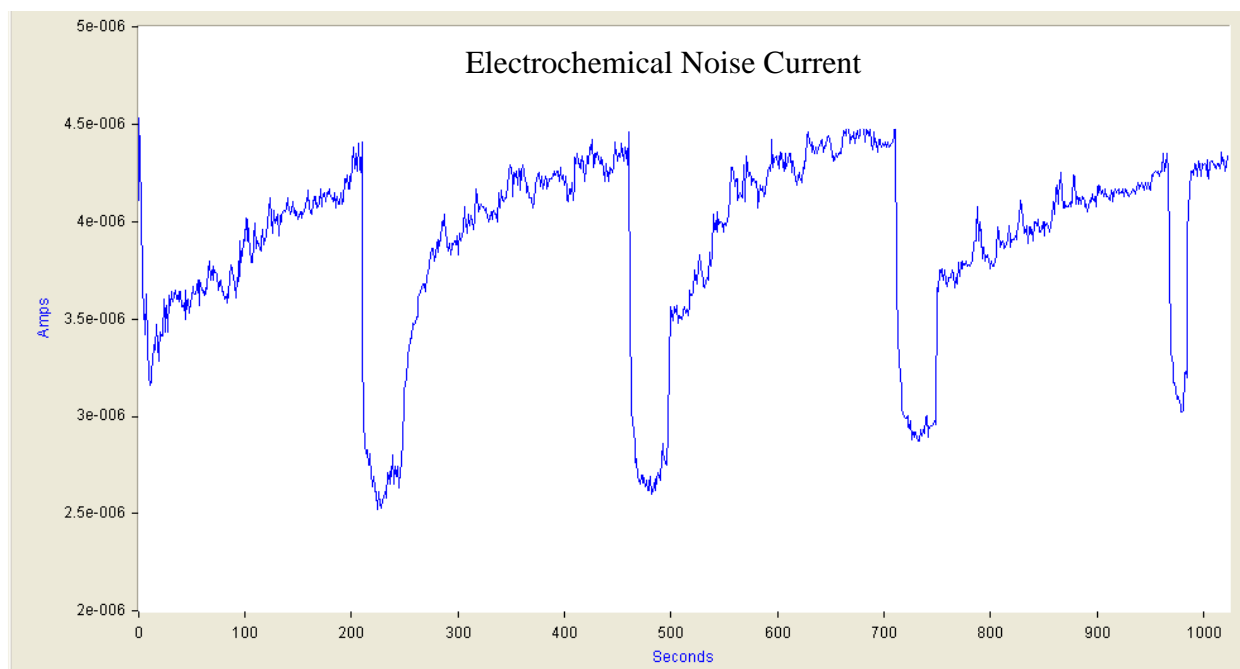


Figure 64.- Electrochemical noise current for Odessa (sample 2). Acquired with Dadisp.

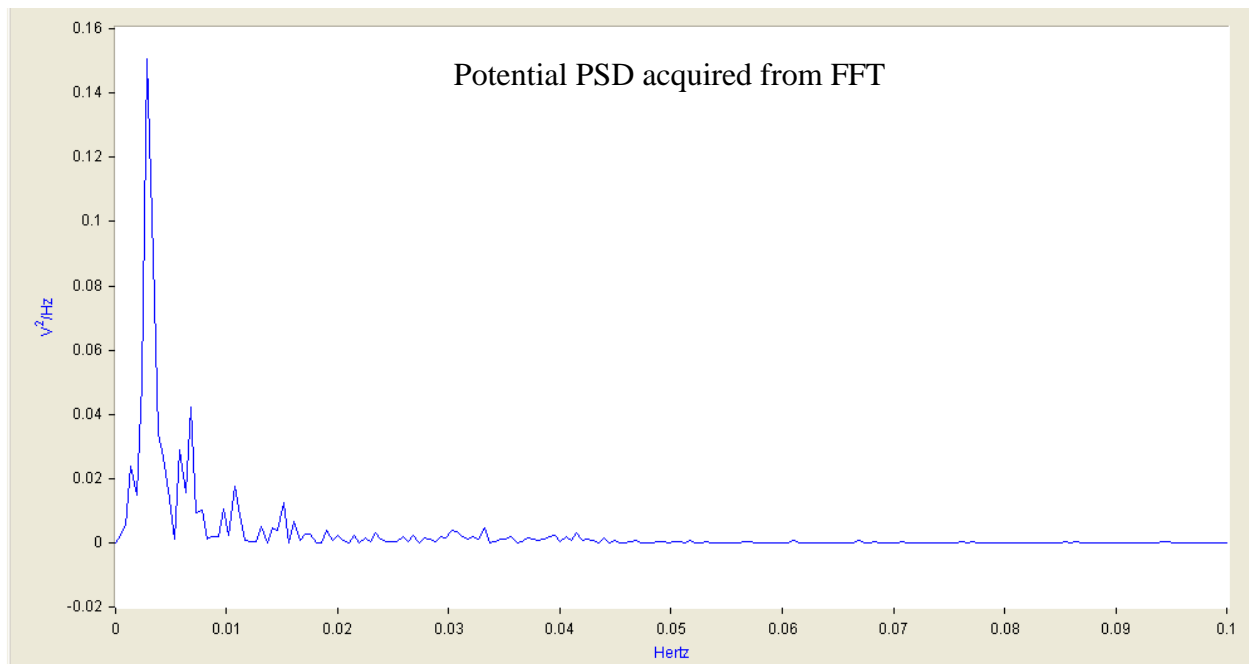


Figure 65.- Potential PSD acquired from FFT method for Odessa (sample 2). Acquired with Dadisp.

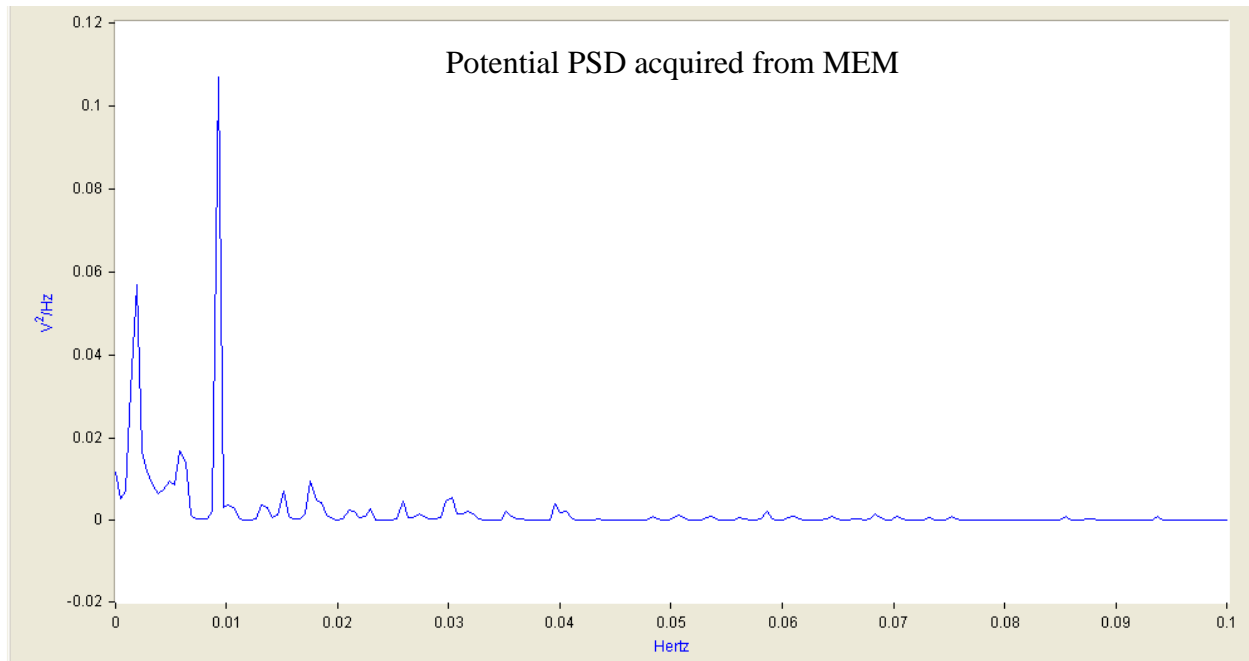


Figure 66.- Potential PSD acquired from MEM method for Odessa (sample 2). Acquired with Dadisp.

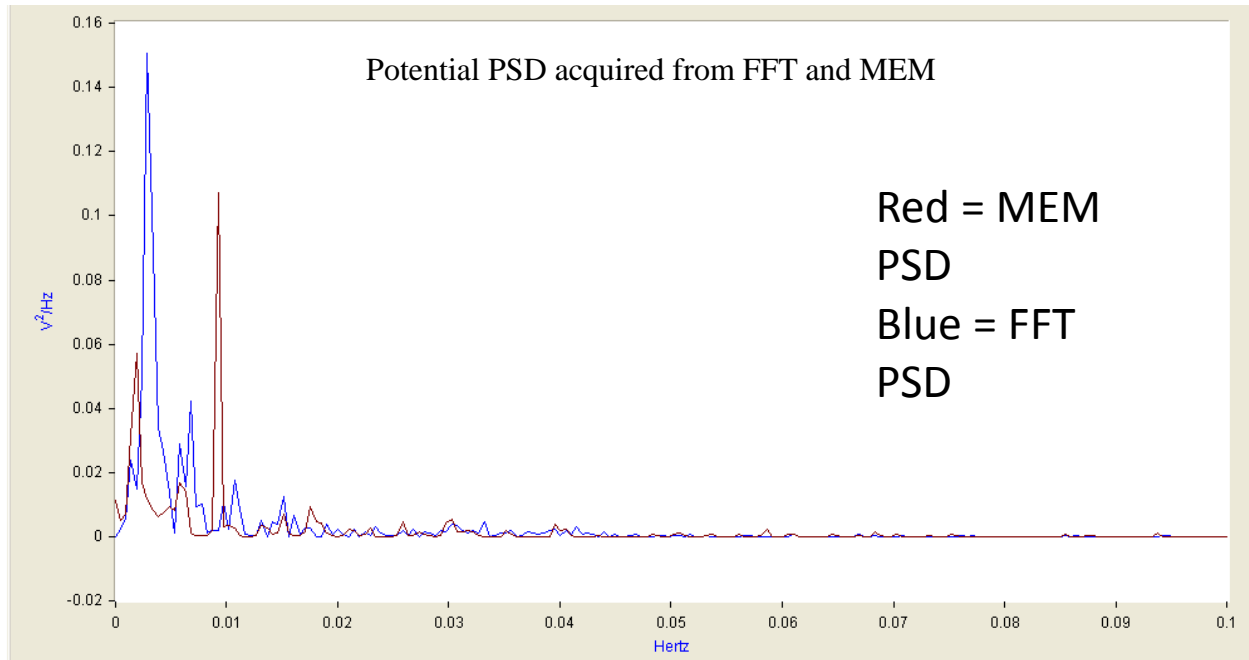


Figure 67.- Potential PSD acquired from FFT and MEM methods for Odessa (sample 2).
Acquired with Dadisp.

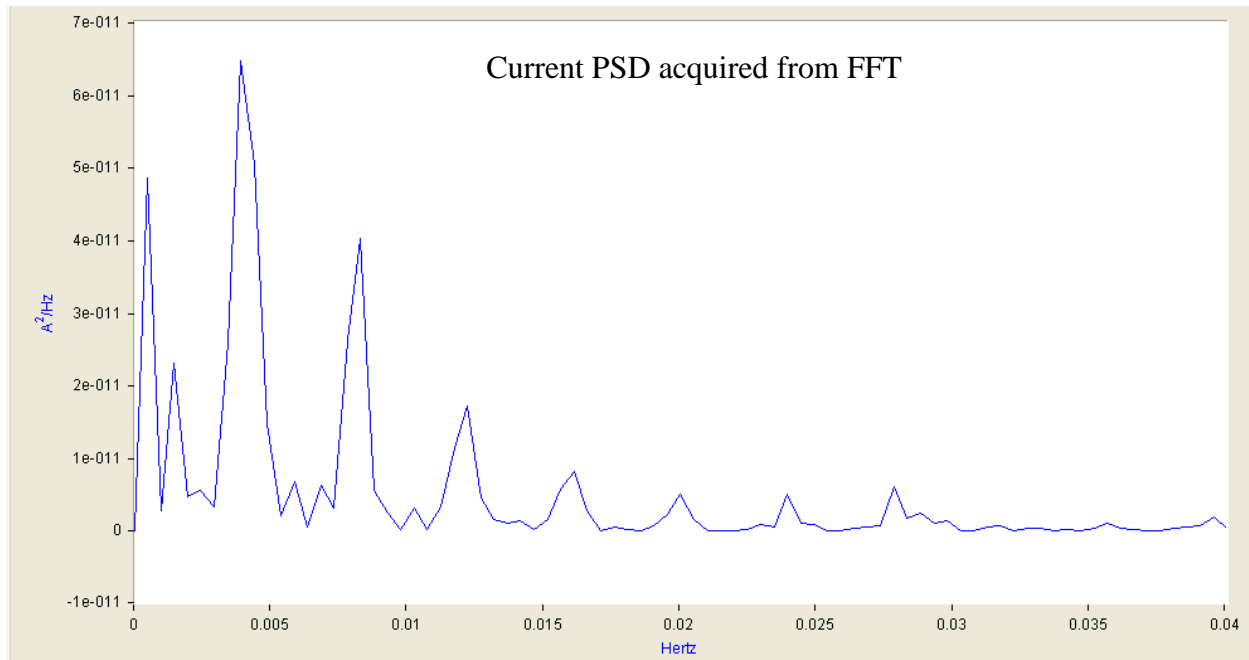


Figure 68.- Current PSD acquired from FFT method for Odessa (sample 2). Acquired with Dadisp.

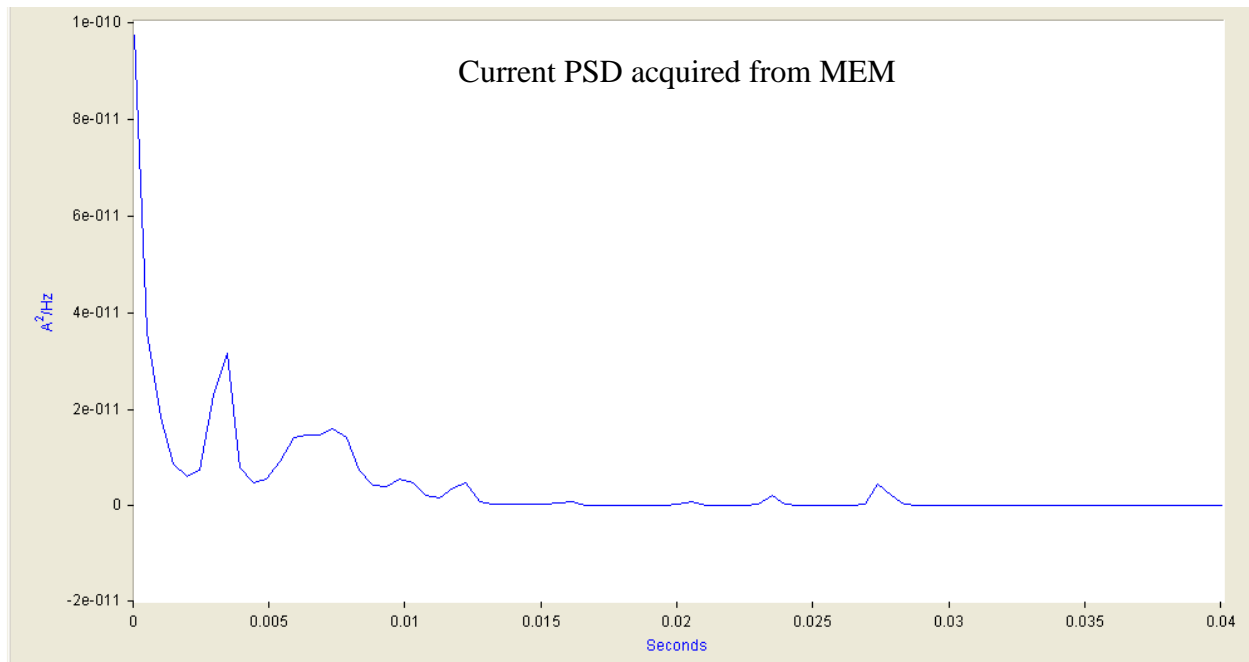


Figure 69.- Current PSD acquired from MEM method for Odessa (sample 2). Acquired with Dadisp.

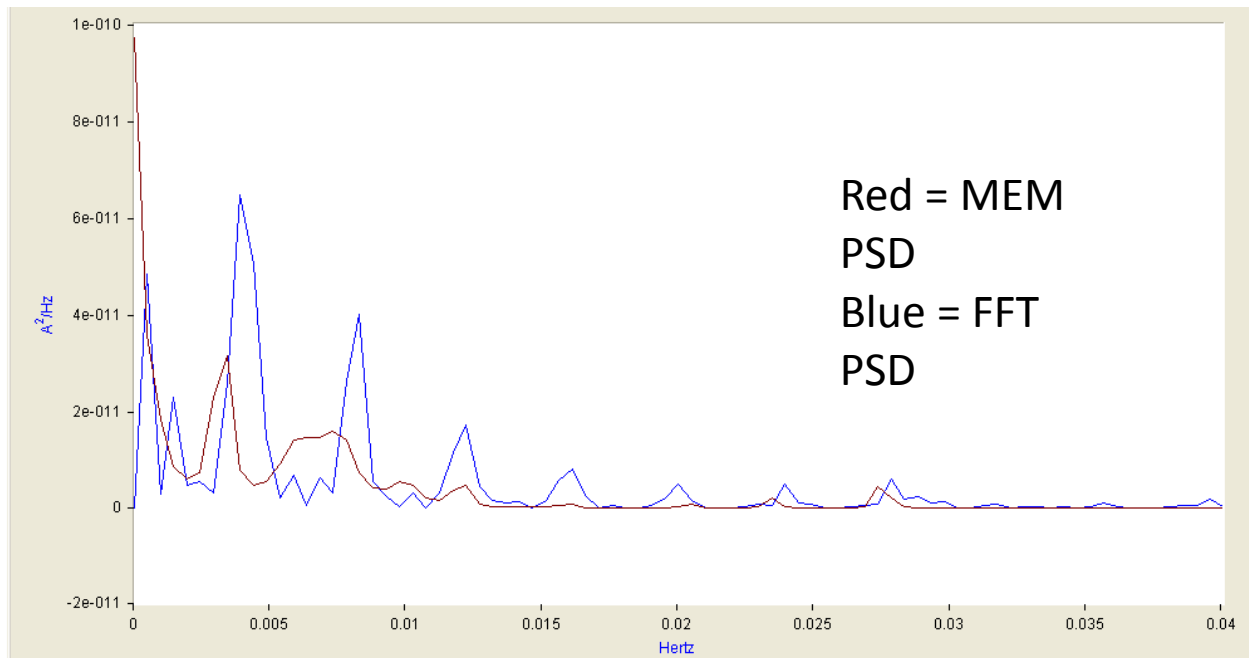
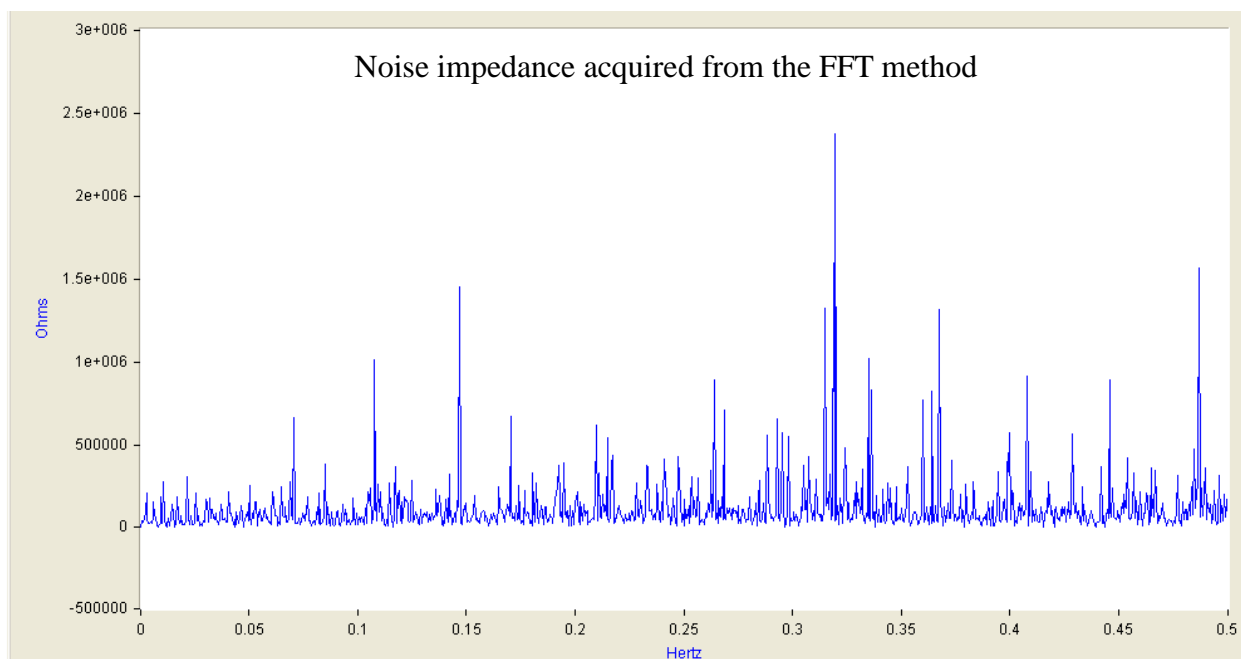


Figure 70.- Current PSD acquired from FFT and MEM methods for Odessa (sample 2). Acquired with Dadisp.



*Figure 71.- Noise impedance calculated with the PSD from the FFT of the potential and current.
Acquired with Dadisp*

Curriculum Vitae

Carlos E. Castillo was born on July 19, 1985 in Ciudad Juarez, Chihuahua, Mex. He is the first son of Raul E. Castillo and Elia R. Tello de Castillo. He obtained his Bachelor of Science in Mechanical Engineering degree at the University of Texas at El Paso (UTEP) in 2008. Shortly after, he pursued his graduate studies at UTEP for his Master of Science in Mechanical Engineering and graduated in the 2011.

Permanent Address: 7142 Orizaba Ave.
 El Paso, TX, 79912

This thesis was typed by Carlos Castillo.